

Ion-acoustic solitons: Analytical, experimental and numerical studies

Von der Fakultät Mathematik und Physik der Universität Stuttgart
zur Erlangung der Würde eines Doktors der
Naturwissenschaftlichen (Dr. rer. nat) genehmigte Abhandlung

Vorgelegt von

Farah Aziz

aus Pakistan

Hauptberichter:

Prof. Dr. U. Stroth

Mitberichter:

Prof. Dr. G. Wunner

Tag der mündlichen Prüfung:

11.07.2011

Institut für Plasmaforschung der Universität Stuttgart

2011

And whoso bringeth the truth and believeth therein – Such are the dutiful.

(Quran, 39:33)

Zusammenfassung

Ein Plasma ist ein nichtlineares und dispersives Medium, das die Ausbreitung vielfältiger Typen von elektrostatischen und elektromagnetischen Wellen ermöglicht. Ion-akustische Wellen sind relativ simple Wellen, die die Form von solitären Wellen annehmen, wenn die Auswirkungen von Nichtlinearität und Dispersion im Plasma einander ausgleichen. Solitäre Wellen werden als Solitonen bezeichnet, wenn sie ihre Form bei der Ausbreitung und nach Kollision mit einem anderen Soliton nicht ändern. Die vorliegende Dissertation beschränkt sich im Wesentlichen auf die theoretische, experimentelle und numerische Untersuchung von Ionen-akustischen Solitonen. Der analytische Teil befasst sich mit der Ausbreitung, der Reflexion und der Transmission von Solitonen in einem inhomogenen Plasma mit eingeschlossenen Elektronen. Der experimentelle Teil und die Simulationen behandeln die Untersuchung von Soliton-Entstehungsmechanismen und ihre Propagation in einem Double-Plasma (DP) Experiment.

Die eindimensionale Ausbreitung von Solitonen wird unter dem Einfluss von Ionen-Temperatur, Dichte-Inhomogenität und Temperatur sowie Konzentration der eingefangenen Elektronen analysiert. Dabei stellte sich heraus, dass die übliche KdV-Gleichung durch variable Koeffizienten und einen zusätzlichen Term, der aufgrund des Dichtegradienten im Plasma erscheint, modifiziert wird. Diese modifizierte KdV-Gleichung (mKdV) wird unter Verwendung einer neuartigen Technik namens Sinus-Cosinus-Methode gelöst. Die lineare und nichtlineare Analysen lassen uns schlussfolgern, dass die Soliton-Ausbreitungseigenschaften in der Gegenwart bereits kleiner Populationen von eingefangenen Elektronen signifikant geändert werden, da diese Elektronen von dem Potenzial der Welle gefangen werden und damit während ihrer Ausbreitung stark mit der Welle wechselwirken. Weiterhin wird beobachtet, dass die Solitonen sich in Form eines Dichtehügels entwickeln, das heißt, es handelt sich um Druck-Solitonen. Diese Solitonen entsprechen dem mKdV-Kriterium. Neben der eindimensionalen Ausbreitung von mKdV-Solitonen, wird auch die schiefe Reflexion der Solitonen an einem Dichtegradienten im Plasma untersucht. Dazu werden für einfallende und reflektierte Welle zwei verschiedene mKdV-Gleichungen hergeleitet, und dann am Ort der Reflexion gekoppelt. Die Lösung der gekoppelten Gleichungen zeigt, dass Solitonen mit eingefangenen Elektronen in einem inhomogenen Plasma mit verringerten Amplituden reflektiert werden. Im Zusammenhang mit der Transmission und Reflexion der Solitonen an einem semitransparenten Gitter, werden die Bedingungen für die Schiefe der

Ausbreitung und die maximale Ionendriftgeschwindigkeit hergeleitet. Es wird auch eine Transmission-Reflexions-Erhaltungsgleichung hergeleitet, auf deren Grundlage der Mechanismus der Soliton-Reflexion und Transmission im Detail untersucht werden. Der Einfluss der eingefangenen Elektronen auf die Ausbreitung, Reflexion und Transmission der Solitonen wird durch Bestimmung der Energie, Amplitude und Breite der Solitonen untersucht, zusätzlich zu den Auswirkungen von Temperatur und Drift der Ionen.

Wie bereits erwähnt, werden die experimentellen und Simulationsstudien in einem DP-Gerät durchgeführt. Dieses Gerät besteht aus zwei Plasma-Regionen, der Source-Kammer und der Target-Kammer, die sich beide in einem gemeinsamen Vakuumgefäß befinden. Hier wird die Anregung von linearen und nichtlinearen Ionen-Schallwellen durch das Anlegen von sinusförmigen Burst-Signalen auf dem Gitter, das die Source und die Target-Kammern trennt, durchgeführt. Der Soliton-Erzeugungsmechanismus in der Target-Kammer wird durch Messungen mit Hilfe einer Langmuir-Sonde untersucht. Es wird beobachtet, dass die Profile der Solitonen von einem Ausbruch von schnellen Ionen und einer Abnahme der Ionen begleitet werden, wenn die Elektronentemperatur T_e größer als die Ionentemperatur T_i ist, d.h. $T_e \gg T_i$. Soliton-Profile werden für unterschiedliche Peak-to-Peak-Amplituden, Laufzeiten und Frequenzen der angelegten Gitter-Signale untersucht. Die Soliton-Amplituden werden für unterschiedliche Parameter berechnet, wobei beobachtet wird, dass sie zunächst ansteigen bis sie einen bestimmten Sättigungswert erreichen. Es wird außerdem beobachtet, dass die Soliton-Amplitude ab einer gewissen Grenze unabhängig von der Signalamplitude, Dauer und Frequenz wird. Diese Beobachtung wird in den Experimenten tiefergehend untersucht.

Particle-In-Cell (PIC) Simulationen werden durchgeführt, um den Entstehungs- und Ausbreitungsmechanismus der Solitonen zu untersuchen. Verwendet wird der Code XPDP1, der von PTSG, University of California, Berkeley, USA, entwickelt wurde. Dieser Code wurde modifiziert, um unseren Ansprüchen zu genügen und nur die Target-Kammer des DP-Gerätes zu simulieren. Die Simulationsergebnisse zeigen ähnliche Eigenschaften wie in den beobachteten Experimente für $T_e/T_i > 10$. Detaillierte Einblicke liefern die Simulationen auch in die Soliton-Entstehungsmechanismen basierend auf der Ionen-Phasenraum-Verteilung. Weiterhin wird die Auswirkung der Amplitude, der Dauer und der Frequenz des Anregungssignals auf die Soliton-Entwicklung simuliert. Die simulierten Solitonen verhalten sich in einer konsistenten Weise unter der Auswirkung der Parameter und erreichen eine Sättigung in ihrer Amplitude nach Durchlaufen einer ersten Steigerung. Zusätzlich zeigen die Simulationen bei $T_e/T_i < 10$ mit höheren Konzentrationen von resonanten Ionen eine starke Wechselwirkung der Wellen mit den Ionen, wodurch ein weiteres Soliton durch einen Energie-Austausch-Mechanismus entsteht. Abschließend wird der Entstehungsmechanismus dieses zweiten Solitons basierend auf den Simulationsstudien diskutiert.

Abstract

Plasma is a nonlinear and dispersive medium that supports the propagation of several types of electrostatic and electromagnetic waves. Ion-acoustic waves are very simple kind of waves that take the form of solitary waves, if the effects of nonlinearity and dispersion are balanced with each other in the plasma. A solitary wave is called a soliton if it retains its shape during propagation and after collision with another solitary wave. In the present thesis, the research work is mainly focused on the theoretical, experimental and numerical analyses of ion-acoustic solitons. The analytical part deals with the soliton propagation, reflection and transmission in an inhomogeneous plasma having electrons being trapped in the soliton potential. The experimental and simulation parts emphasize on the soliton evolution mechanisms and their propagation in a Double-Plasma (DP) device.

One-dimensional propagation of the solitons is analyzed under the effects of ion temperature, density inhomogeneity and temperature and concentration of trapped electrons. Here, the usual KdV equation is found to be modified by variable coefficients and an additional term appearing due to the density gradient present in the plasma. This modified KdV (mKdV) equation is solved by using a novel technique, called sine-cosine method. The linear and nonlinear analyses lead us to infer that the soliton propagation characteristics are significantly modified in the presence of even a small population of trapped electrons, as these electrons are trapped by the wave potential and hence interact strongly with the wave during its propagation. Further, it is observed that the solitons evolve in the form of a density hill, which means they are compressive solitons in nature. These solitons fulfill the mKdV criterion. Apart from the one dimensional propagation of mKdV solitons, oblique reflection of the solitons from a density gradient is investigated in the plasma. For this, two different mKdV equations are derived for the incident and reflected waves, and then coupled at the place of reflection. The solution of the coupled equations reveals that the solitons reflect with smaller amplitudes in an inhomogeneous plasma, in the presence of trapped electrons. In relation to the transmission and reflection of the solitons from a semi-transparent grid, conditions are obtained for the obliqueness of the propagation and maximum drift velocity of ions. Also, a transmission-reflection conservation law is derived, based on which the mechanism of soliton reflection and transmission is explored in detail. The contribution of trapped electrons to the solitons' propagation, reflection and transmission is examined through energy, amplitude and width of

the solitons, in addition to the effects of temperature and drift of the ions.

As mentioned, the experimental and simulation studies are conducted in a DP device. This device consists of two plasma regions, the source chamber and a target chamber, both housed in a common vacuum chamber. Here, the excitation of linear and nonlinear ion-acoustic waves is carried out by applying bursts of sinusoidal signals on the grid that separates the source and the target chambers. The soliton generation mechanism in the target chamber is explored by carrying out diagnostic measurements using a Langmuir probe. It is observed that the soliton profiles are accompanied by a burst of fast ions and a depression of ions, when electron temperature T_e remains much larger than the ion temperature T_i , i.e. $T_e \gg T_i$. Soliton profiles are investigated for different peak-to-peak amplitudes, durations and frequencies of the applied grid signal. The soliton amplitudes are calculated for the varying parameters, and are seen to increase initially before reaching a saturation. It is observed that the soliton amplitude becomes independent of the signal amplitude, duration and frequency after a certain limit. This observation is further explored in the experiments.

Particle-In-Cell (PIC) simulations are carried out in order to study in detail the evolution and propagation mechanism of the solitons. The code XPDP1 is used, which is developed by PTSG, University of California, Berkeley, US. This code is modified in order to cater to our requirement of simulating the target chamber of the DP device. The simulation results show similar features as observed in the experiment for $T_e/T_i > 10$. A detailed insight into the soliton evolution mechanism is obtained based on the ion phase-space distributions obtained from the simulations. Also, the effect of the amplitude, duration and frequency of the excitation signal on the soliton evolution is simulated. The simulated soliton is found to behave in a consistent manner under the effect of the parameters and it acquires a saturation in its amplitude after undergoing an initial enhancement. However, the simulations with $T_e/T_i < 10$ having higher concentrations of resonant ions show strong interaction of the waves with the ions, producing another soliton through energy exchange mechanism. Finally, the generation mechanism of this second soliton is discussed based on the simulation studies.

Contents

1	Introduction/Motivation	11
2	Theoretical background of solitons	14
2.1	What are solitons?	14
2.1.1	Historical background of solitons	14
2.1.2	Occurrence of solitons in nature	15
2.1.3	Formation of solitons	15
2.2	Korteweg-deVries (KdV) equation	15
2.2.1	Reductive perturbation technique	17
2.2.2	Properties of KdV solitons	19
2.3	Modified Korteweg-deVries (mKdV) equation	19
2.4	Solitons in the presence of non-isothermal electrons	20
2.5	Solitons in the presence of two-temperature electrons	21
2.6	Solitons in Double-Plasma devices	22
2.7	Solitons in inhomogeneous plasmas	23
2.8	Soliton reflection and/or transmission mechanism	23
3	Propagation of solitons	25
3.1	Geometry of the problem	25
3.2	Linear analysis: Linear dispersion relation	26
3.3	Nonlinear analysis: mKdV equation	30
4	Reflection of solitons	36
4.1	Geometry of the problem	36
4.2	mKdV equation for incident soliton	38
4.3	mKdV equation for reflected solitons	41
4.4	Results and discussion	43
5	Transmission of solitons	51
5.1	Geometry of the problem	51
5.2	Mathematical formulation	52
5.2.1	Relevant mKdV equations	52
5.2.2	Solution of mKdV equations	55
5.3	Soliton reflection-transmission conservation law	57
5.4	Results and discussion	59

6	Solitons in a DP device	67
6.1	FLIPS as a Double-Plasma device	67
6.2	Experimental setup	69
6.3	Excitation of linear ion-acoustic waves in FLIPS	70
6.4	Excitation of solitons in FLIPS	72
6.5	Experimental results	76
6.5.1	Effect of signal amplitude	76
6.5.2	Effect of signal duration	76
6.5.3	Effect of signal frequency	78
7	Particle-In-Cell simulations	83
7.1	Particle simulation models	83
7.2	The Particle-In-Cell simulation technique	85
7.2.1	The computational cycle	85
7.2.2	Scaling	85
7.2.3	Noise	86
7.3	The modified XPDP1 code	86
7.4	Simulation parameters	88
7.5	Creating a steady-state plasma	88
7.6	Excitation of solitons	91
7.7	Simulation results	97
7.7.1	Effect of signal amplitude	97
7.7.2	Effect of signal duration	97
7.7.3	Effect of signal frequency	99
7.8	Role of fast ions	99
8	Conclusions	108

Chapter 1

Introduction/Motivation

Plasma, often referred to as the “fourth state of matter”, is an ionized gas which some estimate to be the primary constituent of 99% of our visible universe. For instance, stars, nebulae, intergalactic medium and interstellar medium are all made up of plasma. Some examples closer to our Earth are polar auroras, lightning and ionosphere. A plasma being a mixture of neutral particles, positive and negative ions is a quasi-neutral fluid which is also electrically conductive. Due to this property, plasma can easily couple with electric and magnetic fields, which in turn gives rise to numerous types of waves and oscillations, in the acoustic, radio and optical range.

In nonlinear and dispersive plasmas, sometimes the dispersion effects on the waves can be compensated by nonlinearity and they can propagate over a large distance keeping the original wave forms. These stable waves are called solitons [1]. Typical examples are waves in shallow water and plasma waves, specifically the ion-acoustic waves. Both waves are governed by a common nonlinear wave equation called Korteweg deVries (KdV) equation. As the term “soliton” suggests, these solitary waves behave like particles, when they interact with each other. Solitons continue to be a subject of interest even today because of their particle-like nature and the property of preserving their identity for long distances. For example, in optical fibers, solitons can travel for thousands of kilometers, and can be used to carry information. The historical background of solitons as well as the basic concepts about the solitons are explained in detail in section 2.1.

The theory behind soliton propagation in homogeneous plasmas is quite widely understood, where the electrons are considered to be isothermal and are represented by Boltzmann distributions. In most of the real situations, one encounters inhomogeneous plasma, in space as well as in the laboratory. When a density inhomogeneity is present in the plasma, the properties of the soliton are altered. Apart from that, if the electrons are non-isothermal, or if two-temperature electrons are present, the existing theory fails to explain the the soliton behavior. It is for this reason we have developed a theoretical model for the propagation, as well as reflection and transmission of the solitons in an inhomogeneous plasma in the presence of non-isothermal two-temperature

trapped electrons. Plasmas with trapped electrons can be present in the auroral magnetosphere [2], where heating and injection can give rise to the presence of hot and cold electrons. In space, two-temperature electrons can be found in Saturn's E rings, for instance [3]. Apart from that, they are also encountered in the laboratory, where fast and slow components of electrons often exist due to the preferential heating of a certain number of electrons due to an external source. The results obtained from our theoretical analyses can have relevance to the understanding of particle and field data that are received from different spacecraft missions in the Earth's auroral ionosphere and the magnetosphere. In a homogeneous plasma the soliton propagation is governed by KdV equation, which is derived by using a reductive perturbation technique. The basics of the KdV equation and the reductive perturbation technique are explained in section 2.2. In our case we are dealing with the soliton propagation in an inhomogeneous plasma, which leads to a modified Korteweg de Vries (mKdV) equation (see section 2.3). Apart from that, two-temperature non-isothermal electrons are also present along with finite temperature ions. The non-isothermal electrons are trapped by the wave potential and interact strongly with the wave during its propagation. In chapter 3 the soliton propagation in an inhomogeneous plasma with two-temperature electrons is discussed. Solitons and other waves can get reflected from the inhomogeneities present in the plasma. Apart from inhomogeneities in plasma, solitons are reported to be reflected from the boundaries and walls of the plasma. So, in chapters 4 and 5 we have developed theoretical models that enable us to examine the soliton reflection and transmission under the effect of two-temperature electrons (including trapped electrons), density inhomogeneity, drift of ions, obliqueness of wave propagation, etc.

A Double-Plasma (DP) device provides a very suitable experimental setup to study the propagation of solitons. This device consists of a source and target chamber, divided by a negatively biased separation grid. In case of our research work, we have used FLIPS (*Flexibles Plasmaexperiment Stuttgart*) as a DP device, in order to experimentally study the propagation of solitons in the target chamber of the device. Additionally, the effects of excitation signal parameters are analyzed by varying the peak-to-peak amplitude, frequency and duration of the signal. In chapter 6, the excitation of solitons in FLIPS, and their dependence on the parameters are discussed.

Simulations are a very useful tool to understand and/or predict plasma behavior. In order to have a detailed insight into the mechanisms going on during the evolution and excitation of solitons in the target chamber of FLIPS, we simulate our experimental results by taking $T_e/T_i > 10$, where T_e is the electron, and T_i is the ion temperature. For this reason, Particle-In-Cell (PIC) simulation technique is used, in which one follows the motion of a large number of charged particles in their self-consistent electric and magnetic fields. Resonant particles are those which have their velocity close to that of the wave. The exchange of energy and momentum between the wave and the resonant ions during the soliton evolution is a very important phenomenon, and using

PIC simulations we are able to analyze it. In chapter 7, the simulation results are presented. PIC simulations make it possible to actually observe the phase-space distributions and the interaction of the resonant and non-resonant ions with the solitons. The phenomena of interactions between particles and waves has become of quite importance due to the involvement of these processes in the heating mechanisms of fusion devices [4] and in accelerating the charged particles [5]. This gives us a good motivation to simulate the interaction of fast ions with the solitons. This can be done by increasing the concentration of resonant ions in the simulation box by raising the ion temperature so that $T_e/T_i < 10$.

Chapter 2

Theoretical background of solitons

2.1 What are solitons?

Solitary waves are localized waves which retain their shapes despite dispersion and nonlinearity of the medium. If two solitary waves emerge with the same shape after having collision with each other, they are termed as solitons.

2.1.1 Historical background of solitons

In 1834 John Scott Russel observed solitary wave for the first time on the Edinburgh Glasgow canal, but it was not understood to be an example of a soliton even after more than a century. Russel was trying to find out the relationship between the speed of the boat and its propelling force, and suddenly due to a minor problem in the apparatus, the boat stopped and he observed a solitary structure in water, and described it like this:

“...it accumulated round the prow of the vessel in a state of violent agitation, then suddenly leaving it behind, rolled forward with great velocity, assuming the form of a large solitary elevation, a rounded, smooth and well-defined heap of water, which continued its course along the channel apparently without change of form or diminution of speed.”

Russel continued to study these waves in the following years, and as a result of his experiments carried out in a water tank, he reported his observations to the British Association in 1844 [6]. According to Russel, a wave of height h , traveling in a channel of depth d has a velocity given by the expression $v = \sqrt{g(d+h)}$, together with g as the acceleration of gravity. This implies that a large amplitude solitary wave travels faster than that of small amplitude. He also reported that a sufficiently large initial mass of water produces two or more independent solitary waves, which cross each other without change of any kind.

Zabusky and Kruskal [1], in order to work on the Fermi-Pasta-Ulam model of phonons in an an-harmonic lattice, approximated the nonlinear spring and

mass system by a nonlinear equation. In 1965, they reported that the solitary waves pass through each other without undergoing any change in speed or shape. This means that when two or more solitary waves collide, they do not break up or disperse, rather they are stable against mutual collisions and retain their identities. It is due to this particle-like behavior that Zabusky and Kruskal named this wave as “**soliton**”, “**on**” being the Greek word for particle (like electron, photon, etc).

2.1.2 Occurrence of solitons in nature

Many examples of solitons can be found in nature; on our planet as well as in space. In oceans, large amplitude internal waves are commonly produced at continental shelf breaks and may evolve into solitons, for instance the internal waves caused by the Strait of Gibraltar. Tsunamis approaching near the shore are said to be explained by nonlinear theory, and due to this reason they have been referred to as solitons by some researchers. Roll clouds can also be described as examples of solitary waves. The most famous are the Morning Glory clouds observed in Australia’s Gulf of Carpentaria.

2.1.3 Formation of solitons

Solitons are formed as a result of a delicate balance between the nonlinearity and dispersion of a medium. Generally, in dispersive media linear waves while propagating at large distances become dispersive and tend to spread because the phase velocity becomes k dependent. In most nonlinear media, when the amplitude of a wave is not small, nonlinear effects start to occur. The most important role of nonlinear effects is to cause steepening of the leading edge of the wave, which then leads to wave breaking. Figures 2.1a shows the spreading of the original waveform, by dispersion, and 2.1b shows the steepening of the waveform caused by the nonlinearity. Figure 2.1c shows how the combination of these two effects gives rise to a stable structure called soliton.

Although plasma behaves generally like a nonlinear medium and almost all plasma waves exhibit dispersion, they do not necessarily show soliton solutions. Nonlinear ion-acoustic waves or ion-acoustic solitons do show soliton behavior and can be described as a typical example of solitons in plasma. Ion-acoustic solitons can be described by a common nonlinear wave equation called **Korteweg-deVries (KdV) equation** originally derived by D. J. Korteweg and G. deVries [7] in 1895.

2.2 Korteweg-deVries (KdV) equation

KdV equation is a nonlinear equation governing weak nonlinear dispersive phenomena. It describes the propagation of a soliton as seen from a reference frame moving with the wave, as a function of time, in case of weak dispersion and a particular weak nonlinearity.

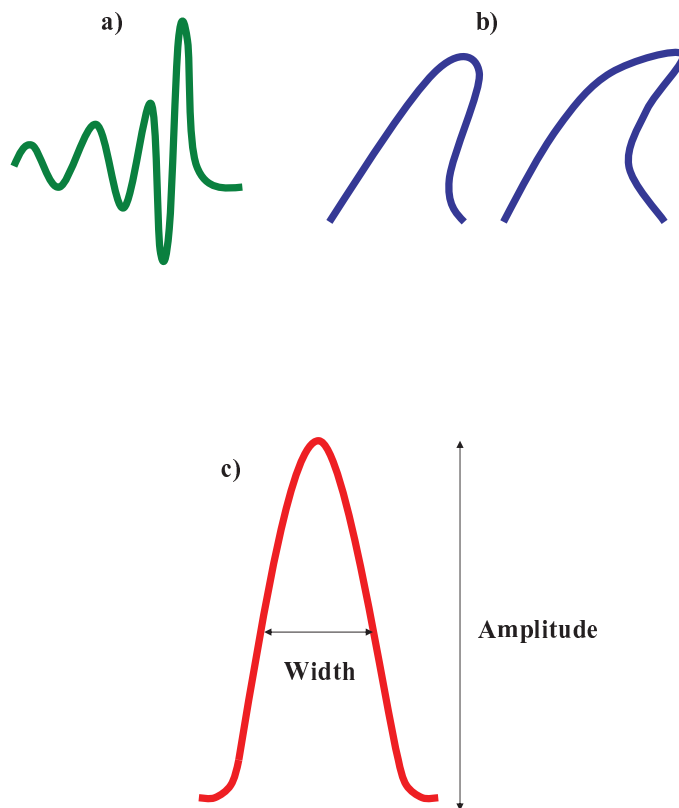


FIGURE 2.1: Formation of a soliton. a) Linear dispersive wave: when the phase velocity becomes k dependent, the wave disperses. b) Nonlinear wave: with the increase in amplitude the wave steepens and has a tendency to break. c) Soliton.

Korteweg and deVries [7] presented a complete account of solutions to the nonlinear hydrodynamical equations. They presented a theory of shallow water waves which resulted in a partial differential equation:

$$\frac{\partial u}{\partial t} + v_0 \frac{\partial u}{\partial x} + \alpha u \frac{\partial u}{\partial x} + \beta \frac{\partial^3 u}{\partial x^3} = 0$$

In the above equation, v_0 is the speed of the small amplitude wave, α is the nonlinearity and β is the dispersion parameter. It becomes quite obvious that the third and fourth terms represent the nonlinear and dispersion effects, respectively. However, if the nonlinearity and dispersion are zero in the above equation then the KdV equation becomes a linear wave equation with a traveling wave solution for any pulse shape at the fixed speed $v_0 = c$.

$$\frac{\partial u}{\partial t} + c \frac{\partial u}{\partial x} = 0$$

In general, the KdV equation is nonlinear with exact traveling wave solutions

$$u(x, t) = A \operatorname{sech}^2 \left[\frac{(x - v_0 t)}{W} \right],$$

where $W = \sqrt{12\beta/\alpha A}$; implying that higher amplitude waves are narrower. With this shape, the effects of dispersion balance those of nonlinearity at an adjustable value of the pulse speed. Thus the solitary wave is recognized as an independent dynamic entity, maintaining a dynamic balance between these two influences. Interestingly, in accordance with Russel's empirical results, solitary wave velocities are related to amplitudes by the relation

$$v = c + \frac{1}{3}\alpha A.$$

2.2.1 Reductive perturbation technique

The reductive perturbation technique requires the expansion of dependent quantities (like densities, velocities, potential etc.) about their equilibrium position in the form of a small parameter ϵ , the smallness of which determines the order/strength of the perturbation. This expansion has to be done in view of the powers of ϵ in the stretched coordinates in order to balance the effects of nonlinearity and dispersion. It means, the stretching i.e. the transformation of coordinates to the wave frame of reference, and expansion of dependent quantities i.e. type of oscillations/perturbation, leads to this balance. The higher powers of ϵ means that a physical quantity varies more slowly in comparison with the one which carries lower powers of ϵ .

Most of the physical systems are governed by equations of motion, which are not very simple, i.e. they contain several dependent variables. In order to reduce the system to a simpler form, a procedure was proposed by Washimi and Taniuti [8], which in a systematic manner reduces the general nonlinear

evolution equations into simpler and more tractable nonlinear equations. Under the assumption that the amplitudes of the waves are small, one is able to reduce the starting hyperbolic system to a few simple nonlinear equations, i.e. KdV equation, Burgers equation, the nonlinear Schrödinger equation.

It is hard to define the rules of the reduction method, because it is based mainly on how to choose the relevant scales using one's experience. It does not have a concrete mathematical foundation, like a lot of other asymptotic theories. The assumption according to Leibovich and Seebass [9] is, "if it works, its right".

In order to carry out the reductive perturbation method, it is worthwhile to normalize all the variables in the problem, in order to make them dimensionless which spares us the task of working with so many constants. For instance, all the perturbed densities can be rescaled by the background density n_0 , and the space coordinate r by the Debye length λ_D , which is the measure of the shielding distance of the sheath, given by $\lambda_D = \sqrt{\epsilon_0 T_e / n_0 e^2}$, where, ϵ_0 , T_e , and e are the permittivity of free space, electron temperature and electronic charge, respectively.

$$n_i \rightarrow \frac{n_i}{n_0}, \quad r \rightarrow \frac{r}{\lambda_D}$$

The next step would be to expand all the dependent variables in terms of the small expansion parameter ϵ .

$$f = f_0 + \epsilon f_1 + \epsilon^2 f_2 + \epsilon^3 f_3 \dots$$

where f could represent the dependent variables, like density, potential, velocities etc. The physical properties of the system decide if the first term exists or not. If it does exist then it is the equilibrium value, for instance, the density is perturbed around its equilibrium value n_0 , so that for the density we can write

$$n = \epsilon^0 n_0 + \epsilon^1 n_1 + \epsilon^2 n_2 + \epsilon^3 n_3 \dots$$

In the absence of an electric field there is no equilibrium potential, so the first term vanishes, in this case

$$\varphi = \epsilon^1 \varphi_1 + \epsilon^2 \varphi_2 + \epsilon^3 \varphi_3 \dots$$

In the first approximation, as per the theory of solitons of weakly dispersive waves, the wave moves with the phase velocity that does not depend on the wave number. In the frame moving with this velocity the evolution of the wave is defined by the weak dispersion of the wave and the weak nonlinearity. This evolution takes place on the longer time scale and in the case of solitons the dispersion and the nonlinearity balance each other. This physical sense is reflected by the transformation to the coordinates

$$\xi = \epsilon^p (x - \lambda_0 t), \quad \tau = \epsilon^{3p} t$$

where λ_0 is the phase velocity of the wave neglecting the wave dispersion. This scaling is usually determined by the linear dispersion relation and then the value of p is decided according to the order of nonlinearity we wish to deal with. Washimi and Taniuti [8] proposed the transformation

$$\xi = \epsilon^{1/2}(x - t), \quad \tau = \epsilon^{3/2}x$$

and derived the KdV equation in plasma for the first time. This type of transformation to coordinates ξ and τ is appropriate for a homogeneous medium.

Asano and Taniuti [10] made the first attempt in the inhomogeneous media and proposed such stretched coordinates where the phase velocity λ_0 appears in a time like coordinate. It means

$$\xi = \epsilon^p \left(\frac{x}{\lambda_0} - t \right), \quad \tau = \epsilon^{2p}x,$$

are suitable. Then they had extended the reductive perturbation technique to study sound waves in an inhomogeneous duct, sound wave propagation through a stratified layer and hydromagnetic waves across a non uniform magnetic field [11].

2.2.2 Properties of KdV solitons

A KdV soliton must fulfill the following criteria:

1. The velocity of the soliton V_S remains constant throughout its course of propagation.
2. The velocity is proportional to the soliton amplitude. This means that the velocity V_S and amplitude A_S of a KdV soliton are related as [1]

$$V_S = C_i + \frac{1}{3}A_S \quad (2.1)$$

along with C_i as the ion-acoustic speed.

3. The product of the amplitude A_S of the soliton and width W_S squared is a constant [1]

$$A_S \times W_S^2 = \text{Constant} \quad (2.2)$$

2.3 Modified Korteweg-deVries (mKdV) equation

Sometimes, departure from the Boltzmann distribution function for the electrons could arise, for instance, due to trapped particles, and can lead to a modified KdV (mKdV) equation. An mKdV equation is similar to the simple KdV equation in the sense that both of these equations are completely

integrable. The only difference from the KdV equation is the power of the nonlinear term, so that the mKdV equation is written as

$$\frac{\partial u}{\partial t} + v_0 \frac{\partial u}{\partial x} + \alpha u^2 \frac{\partial u}{\partial x} + \beta \frac{\partial^3 u}{\partial x^3} = 0$$

In the above equation the third and the fourth terms are the nonlinear and dispersive terms, respectively. The criterion for the mKdV soliton is slightly different from that of the KdV soliton, i.e. the product of the amplitude of the soliton and width is a constant [12].

$$A_S \times W_S = \text{Constant} \quad (2.3)$$

2.4 Solitons in the presence of non-isothermal electrons

Normally when we derive KdV equation for ion-acoustic waves, electrons are considered to be isothermal. This isothermality is justified by the fact that the speed of a thermal electron is much higher than that of the ion-acoustic wave, and so it remains more or less unaffected by the wave. Hence, the density of the isothermal electrons can be represented by a Boltzmann distribution,

$$f_e \propto \exp \left[- \left(\frac{v^2}{2} - \varphi \right) \right]$$

This leads us to a normalized electron density given by

$$n_e = \exp(\varphi) \quad (2.4)$$

which shows that the electrons are isothermal, provided that electron inertia is neglected. Here, the velocity of the electron v , and the potential φ are normalized by $\sqrt{kT_e/m_i}$ and kT_e/e , respectively.

Sometimes we encounter cases where electrons cannot maintain their isothermality, for instance due to lack of collisions. In such cases we observe a flat topped distribution, which is an obvious deviation from the Boltzmannian behavior. It was first shown by Schamel [13, 14] that for the non-isothermal electrons, we have a vortex-like distribution which solves the electron Vlasov equation. Thus, the distribution in 1-D for the free electrons is as follows:

$$f_{ef}(v) = \tilde{K} \sqrt{\frac{\delta}{2}} \exp \left[- \left(\frac{\delta}{2} v^2 - \varphi \right) \right] \quad \text{for } v > +\sqrt{\frac{2\varphi}{\delta}}, v < -\sqrt{\frac{2\varphi}{\delta}}.$$

For trapped electrons, the distribution looks like this:

$$f_{et}(v) = \tilde{K} \sqrt{\frac{\delta}{2\pi}} \exp \left[-\beta \left(\frac{\delta}{2} v^2 - \varphi \right) \right] \quad \text{for } |v| \leq \sqrt{\frac{2\varphi}{\delta}}.$$

Here $\delta = m_i/m_e$, $\beta = T_{ef}/T_{et}$ and $\tilde{K} = 1$ for the case of solitary waves.

The number densities can be derived from the above distributions and are given as:

$$n_e(\varphi) = \int_{-\infty}^{-\sqrt{2\varphi/\delta}} f_{ef}(v)dv + \int_{-\sqrt{2\varphi/\delta}}^{\sqrt{2\varphi/\delta}} f_{et}(v)dv + \int_{\sqrt{2\varphi/\delta}}^{\infty} f_{ef}(v)dv$$

$$n_e(\varphi) = \tilde{K} \left[\exp(\varphi)\operatorname{erfc}(\varphi)^{1/2} + |\beta|^{-1/2} \begin{cases} \exp(\beta\varphi)\operatorname{erfc}(\beta\varphi)^{1/2} & \text{for } \beta \geq 0, \\ (2/\sqrt{\pi})W(\sqrt{-\beta\varphi}) & \text{for } \beta < 0 \end{cases} \right] \quad (2.5)$$

Here, $\beta = 1$ means the isothermal case which reduces the above relation to a Maxwellian (Eq. 2.4). $\beta = 0$ represents the flat topped distribution for the non-isothermal case. Now, for small amplitudes ($\varphi \ll 1$) the electron number density is given as

$$n_e(\varphi) = \tilde{K} \left[1 + \varphi - \frac{4}{3} \left(\frac{1-\beta}{\sqrt{\pi}} \right) \varphi^{3/2} + \frac{1}{2} \varphi^2 \dots \right] \quad (2.6)$$

In the above equation, the third terms is the contribution of the resonant electrons, both trapped and free.

2.5 Solitons in the presence of two-temperature electrons

In various situations, there is a possibility of the presence of two-temperature electron components in plasmas. For example, hot turbulent plasmas of thermonuclear interest often have high-energy tails. Strong electron beam plasma interactions can result in two-electron-temperature plasmas and hot cathode discharge plasmas have double electron temperature distributions. Apart from that, in a Double-Plasma (DP) device, plasma is created by a biased filament that also introduces a fast electron component. In addition, the two-temperature non-isothermal electrons can be obtained in the target chamber of a DP device by the rf-heating of the plasma, as suggested by Nishida and Nagasawa [15]. Other examples of the existence of two-temperature electrons can be found in space; in Saturn's E rings for instance [3].

When two groups of electrons are present, the Langmuir probe current characteristics show a distinct break in the electron-retardation region. For plasmas having relatively colder ions, the restoring force provided to the ion-acoustic waves is due to the pressure of the electrons. This is the reason why ion-acoustic waves are sensitive to the presence of electrons having a different temperature. As compared to ion time scales, the time scales of the physical processes giving rise to such electron distributions are relatively shorter, which justifies the description of the two electron components as two

fluids. Considering this fact, Jones *et al.* [16] showed that the ion component being relatively colder, the restoring force is then provided by the electron pressure, represented by an effective temperature T_{eff} , given as

$$T_{eff} = \frac{(n_{el0} + n_{eh0})T_{el}T_{eh}}{n_{el0}T_{eh} + n_{eh0}T_{el}}.$$

Here T_{el} and T_{eh} are the temperatures, and n_{el0} and n_{eh0} are the densities of the low- and high-temperature electrons. The effective temperature depends on both the temperatures and the number densities of both the components.

There has been an increasing interest in studying the propagation of solitons in a plasma containing two-temperature electrons. In such plasmas, two groups of the electrons at different temperatures are present and the electron velocity distribution may be represented by the superposition of two Maxwellians for the isothermal electrons [17], or by the superposition of two vortex-like distributions for the non-isothermal electrons [13]. The non-isothermal electrons are trapped by the wave potential and interact strongly with the wave during its evolution [18]. Jones *et al.* [16] discussed experimentally and theoretically the propagation of ion-acoustic waves in a two-electron temperature plasma. They observed the effect of presence of even a small fraction of the lower electron temperature component on the behavior of the waves. Shortly after that, Goswami and Buti [17] studied theoretically the effects of a relatively cold electron component in the plasma on the amplitude of the ion-acoustic solitary wave. Nishida and Nagasawa [15] reported the first experimental existence of rarefactive ion-acoustic solitons in a two electron temperature plasma in a DP device. More recently, Singh and Malik [19] studied theoretically the propagation of fast and slow solitons in an inhomogeneous magnetized negative-ion containing plasma with two-temperature non-isothermal electrons.

2.6 Solitons in Double-Plasma devices

A typical Double-Plasma device consists of two plasma regions, the source chamber and a target chamber, both housed in a common vacuum chamber. The source and target plasmas are separated from each other by a negatively biased separation grid. DP devices have proven to be quite useful for studying solitons, since the first experimental observations of solitons carried out by Ikezi *et al.* [20]. Later, several novel techniques [21] were employed by experimentalists to excite ion-acoustic solitons in these devices [22, 23]. Among a few techniques of producing solitons, grid excitation of solitons has largely been used [21, 24, 25]. In this technique, the grid separating the target and source chambers is modulated at a frequency higher than the ion plasma frequency, so that the ions coming from the source chamber are modulated while entering into the target chamber. This results in the excitation of ion-acoustic solitons along with ion bursts in the target chamber of the DP device. Nega-

tive ions have also been produced in these devices for investigating the soliton propagation [22, 23, 26, 27].

2.7 Solitons in inhomogeneous plasmas

In most of the real situations, we encounter inhomogeneous plasmas rather than homogeneous ones. Although in a homogeneous plasma the soliton solution of the KdV equation travels with constant speed or shape, however, the weak inhomogeneities of the plasma contribute to slowly varying coefficients in the usual KdV equation [28, 29, 30, 31]. In some cases, the inhomogeneities also lead to an extra term in the KdV equation. Accordingly, the soliton behavior is modified in inhomogeneous plasmas. Kuehl [32] derived the KdV equation in a weakly inhomogeneous plasma, significantly modified by the effects of both ion drift and ionization. The density gradients, apart from being the origin of an extra term in the KdV equation, are also responsible for the reflection of solitons [28]. The mechanism of reflection of soliton by plasma inhomogeneities is discussed in detail in the following section.

2.8 Soliton reflection and/or transmission mechanism

Solitons have been reported to reflect from inhomogeneities in the plasma, as well as from the solid surfaces, inserted in the plasma. Kuehl [28] analytically studied the reflection of ion-acoustic solitons by plasma inhomogeneities in a weakly inhomogeneous plasma. The coupled KdV equations for the oppositely traveling ion-acoustic waves were derived, and it was shown that the reflected wave is small compared with both the trailing shelf and the incident soliton, and the soliton amplitude decreases due to energy transfer to the shelf.

DP devices have primarily been used for studying the reflection of solitons, either from the grids or reflectors inserted in the device. Dahiya *et al.* [33] have shown that sharp density gradients produced by a negatively biased grid immersed in the plasma can lead to the reflection of solitons, where the scale size of the density gradient is the same or smaller than the width of the initial soliton. Nishida [34] studied the partial reflection of a planar ion-acoustic soliton from a planar metallic plate, glass plate or metallic grid. Imen and Kuehl [35] analyzed the reflection of a planar ion-acoustic soliton on a planar metallic or dielectric surface and found the results to be in agreement with Nishida's experiment [34]. Investigations have also been carried out in order to study the reflection of solitons from unbiased structures inserted into the plasma [36], and space charge sheath [37], etc.

Transmission of solitons through mesh grids or density inhomogeneities has been a slightly less explored field. Nagasawa and Nishida [38] experimentally observed nonlinear reflection and refraction of the solitons from a metallic mesh

electrode in a DP device and found a new phenomenon called the nonlinear Snell's law. Cooney *et al.* [12] had experimentally investigated the soliton propagation, collision, and reflection at a sheath in a multicomponent plasma and discussed a soliton reflection-transmission conservation law that described the KdV soliton propagation, in agreement with the experimental results of Nishida [34].

The mechanism behind the reflection of the solitons can be based on several theories proposed by researchers. Ishihara [39] proposed a theory for the reflection of solitons based on the existence of a sheath in front of the reflector, which results in a steep density gradient as well as a supersonic flow of ions. This sheath acts as a high-pass filter and hence allows all the high-frequency waves and rejects the low-frequency-wave components. Hence, the solitons being long-wavelength waves are reflected back into the subsonic flow region before they reach the sharp density gradient region having supersonic flow. The short wavelength waves are then absorbed by the supersonic sheath region due to shock formation and other nonlinear processes. Thus, the density inhomogeneity as well as ion flow are important factors for the soliton reflection.

Nakamura [40] suggested that the efficient reflection of solitons from grids could be attributed to the counter streaming ions through the grid. It was also proposed [34, 38] that when an incident wave enters the sheath area, it pushes up the sheath potential which then causes the emitted ions to form a reflected or transmitted wave.

According to yet another model [41, 42], the reflection of ions play an important role in soliton reflection from a bipolar structure consisting of a negatively biased grid and positively biased metal plate. The reflected ion perturbation causes the re-excitation of the soliton from the bipolar structure device.

The transmission of solitons through a grid could also be explained on the basis of the concept that ion-acoustic solitons tunnel through the sheath area. These solitons are resonantly absorbed when the spatial width of the soliton is comparable to the characteristic gradient scale length of the sheath in front of the reflector. This was experimentally shown by Nishida, Yoshida, and Nagasawa [43].

Chapter 3

Contribution of trapped electrons to soliton evolution in an inhomogeneous plasma

In this chapter, the one dimensional propagation of solitons is analyzed in the presence of trapped electrons and a density gradient in a plasma. We use the well-known reductive perturbation technique in order to study the possible modes in the plasma and their evolution as solitons. In such an unmagnetized plasma, which has a density gradient, finite temperature ions and trapped electrons, a modified Korteweg-deVries (mKdV) equation is realized along with an additional term due to the density gradient. This equation is solved to get the solitary wave solution. The phase velocity, soliton amplitude, and width are examined under the effect of electron and ion temperatures and their concentrations. The main focus will be on the contribution of thermal effects of ions and the group of two-temperature electrons to the soliton propagation characteristics.

3.1 Geometry of the problem

We consider an inhomogeneous plasma, where the density decays in $+x$ direction so that there exists a background flow of the ions with velocity v_0 in $+x$ direction. Apart from having a density gradient, this plasma has ions with finite temperature T_i and two groups of non-isothermal electrons with temperatures T_{el} and T_{eh} , respectively. The effective temperature of the electrons is thus given by

$$T_{eff} = \frac{n_0 T_{el} T_{eh}}{n_{el0} T_{eh} + n_{eh0} T_{el}}$$

where, n_{el0} , n_{eh0} and n_0 are the unperturbed densities of low- and high-temperature electrons and ions, respectively.

In order to investigate the propagation of solitons in inhomogeneous plasma we start with a set of 1D fluid equations by considering the plasma to be inter-

penetrating fluid. We normalize the fluid equations in order to make them dimensionless for the sake of simplicity. The electron and ion densities n_{el} , n_{eh} and n_i are normalized by the unperturbed plasma density n_0 . Furthermore, the ion flow velocity v is normalized by the effective ion-acoustic speed $(T_{eff}/m_i)^{1/2}$, where m_i is the ion mass. The space coordinate x and time coordinate t are normalized by the Debye length $(\epsilon_0 T_{eff}/n_0 e^2)^{1/2}$ and inverse ion plasma frequency $(n_0 e^2/\epsilon_0 m_i)^{-1/2}$. The electric potential φ is normalized by T_{eff}/e , where e is the electronic charge. We consider unperturbed field to be zero [44] which makes unperturbed electric potential $\varphi_0 = 0$. After normalization, the equation of continuity, equation of motion of ions and Poisson's equation are given as

$$\frac{\partial n_i}{\partial t} + \frac{\partial}{\partial x}(n_i v) = 0 \quad (3.1)$$

$$\frac{\partial v}{\partial t} + v \frac{\partial v}{\partial x} + \frac{\partial \varphi}{\partial x} + \frac{3\sigma}{n_i} \frac{\partial n_i}{\partial x} = 0 \quad (3.2)$$

$$\frac{\partial^2 \varphi}{\partial x^2} + n_i - n_{el} - n_{eh} = 0 \quad (3.3)$$

Here, n_i , n_{el} and n_{eh} are the ion and electron densities, v is the ion flow velocity and $\sigma = T_i/T_{eff}$. The densities of low- and high-temperature electrons are calculated using the distributions for non-isothermal electrons given by Schamel [13], as explained in section 2.4.

$$n_{el} = n_{el0} \left[1 + \frac{T_{eff}}{T_{el}} \varphi - \frac{4}{3} b_l \left(\frac{T_{eff}}{T_{el}} \varphi \right)^{3/2} + \frac{1}{2} \left(\frac{T_{eff}}{T_{el}} \varphi \right)^2 + \dots \right] \quad (3.4)$$

$$n_{eh} = n_{eh0} \left[1 + \frac{T_{eff}}{T_{eh}} \varphi - \frac{4}{3} b_h \left(\frac{T_{eff}}{T_{eh}} \varphi \right)^{3/2} + \frac{1}{2} \left(\frac{T_{eff}}{T_{eh}} \varphi \right)^2 + \dots \right] \quad (3.5)$$

In the above equations b_l and b_h are the non-isothermality parameters [18, 19, 45, 46], given as

$$b_l = \frac{(1 - T_{el}/T_{eff})}{\sqrt{\pi}} \quad \text{and} \quad b_h = \frac{(1 - T_{eh}/T_{eff})}{\sqrt{\pi}}.$$

3.2 Linear analysis: Linear dispersion relation

Using the reductive perturbation technique as explained in the previous chapter, the densities, fluid velocity, and the potential are expanded in terms of ϵ as following in order to derive the phase velocity relation and a relevant mKdV equation:

$$n_i = n_0(x) + \epsilon n_{i1}(x, t) + \epsilon^{3/2} n_{i2}(x, t) + \epsilon^2 n_{i3}(x, t) + \dots \quad (3.6a)$$

$$n_{el} = n_{el0}(x) + \epsilon n_{el1}(x, t) + \epsilon^{3/2} n_{el2}(x, t) + \epsilon^2 n_{el3}(x, t) + \dots \quad (3.6b)$$

$$n_{eh} = n_{eh0}(x) + \epsilon n_{eh1}(x, t) + \epsilon^{3/2} n_{eh2}(x, t) + \epsilon^2 n_{eh3}(x, t) + \dots \quad (3.6c)$$

$$v = v_0(x) + \epsilon v_1(x, t) + \epsilon^{3/2} v_2(x, t) + \epsilon^2 v_3(x, t) + \dots \quad (3.6d)$$

$$\varphi = \epsilon \varphi_1(x, t) + \epsilon^{3/2} \varphi_2(x, t) + \epsilon^2 \varphi_3(x, t) + \dots \quad (3.6e)$$

Here v_0 is the unperturbed ion flow velocity. From the above equations it can be seen that the unperturbed quantities are functions of space coordinate x , and the perturbed quantities are functions of both space and time coordinates, i.e. x and t .

The following stretched coordinates are used [19, 46, 47]:

$$\xi = \epsilon^{1/4} \left(\frac{x}{\lambda_0} - t \right) \quad \text{and} \quad \tau = \epsilon^{3/4} x,$$

where λ_0 is the phase velocity of the linear wave.

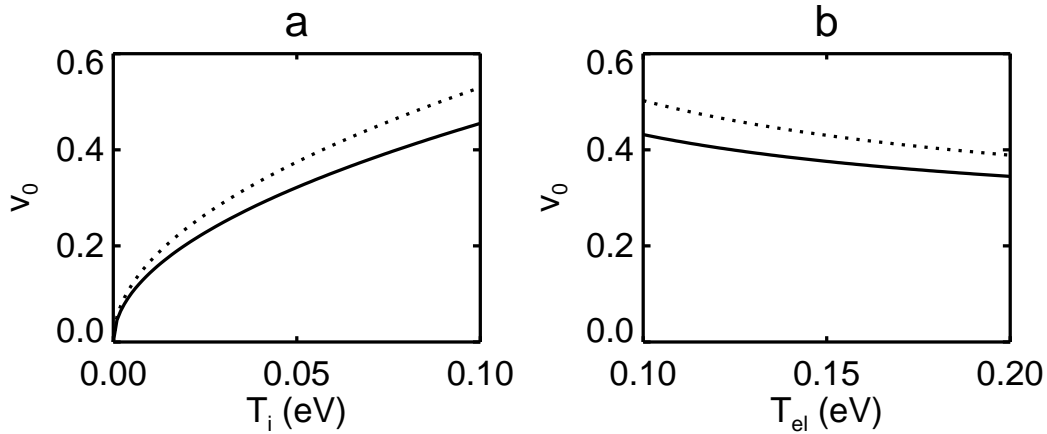


FIGURE 3.1: Dependence of background ion flow velocity v_0 on a) ion temperature T_i , provided $T_{el} = 0.1$ eV and b) on the temperature of trapped electrons T_{el} , provided $T_i = 0.09$ eV. The graphs are plotted for $n_{el0} = 0.04$ (solid line), and $n_{el0} = 0.06$ (dotted line), where $n_0 = 0.8$.

Since the plasma is inhomogeneous in space only, the unperturbed quantities are taken to be the functions of the space coordinate τ only, which means

$$\frac{\partial n_0}{\partial \xi} = \frac{\partial n_{el0}}{\partial \xi} = \frac{\partial n_{eh0}}{\partial \xi} = \frac{\partial v_0}{\partial \xi} = 0$$

As per the reductive perturbation approach, the set of stretched coordinates and the expansion of physical quantities are used in the basic fluid equations. Through this we get various expressions with different powers of ϵ , which are separately put to zero in order to obtain various equations in zeroth, first and second ordered quantities. This way the zeroth order equations are obtained as follows:

$$n_0 v_0 \frac{\partial}{\partial \tau} v_0 + 3\sigma \frac{\partial}{\partial \tau} n_0 = 0 \quad (3.7a)$$

$$n_0 \frac{\partial}{\partial \tau} v_0 + v_0 \frac{\partial}{\partial \tau} n_0 = 0 \quad (3.7b)$$

$$n_0 = n_{0l} + n_{0h} \quad (3.7c)$$

Comparing Eqs. 3.7a and 3.7b we get a relation for the background ion flow velocity v_0 as

$$v_0 = \sqrt{3\sigma} = \sqrt{3T_i \frac{n_{el0}T_{eh} + n_{eh0}T_{el}}{(n_{el0} + n_{eh0})T_{el}T_{eh}}} \quad (3.8)$$

It can be seen that v_0 is proportional to $\sqrt{\sigma}$, which is the ratio of the ion temperature T_i to the effective temperature of the electrons T_{eff} . As v_0 is proportional to the square root of the ion temperature we see in Fig. 3.1a that with an increase in T_i the background flow velocity v_0 of the ions also increases. The effect of temperature of trapped electrons T_{el} on v_0 is plotted in Fig. 3.1b, which shows a decrease in v_0 , as T_{el} increases. The result is shown for two different concentrations of low-temperature electrons, indicating that the background ion-flow velocity is higher for higher concentrations of low-temperature electrons.

The first order equations are given below:

$$n_0 \frac{\partial}{\partial \xi} \varphi_1 + 3\sigma \frac{\partial}{\partial \xi} n_{i1} - n_0(\lambda_0 - v_0) \frac{\partial}{\partial \xi} v_1 = 0 \quad (3.9a)$$

$$n_0 \frac{\partial}{\partial \xi} v_1 - (\lambda_0 - v_0) \frac{\partial}{\partial \xi} n_{i1} = 0 \quad (3.9b)$$

$$n_{i1} = n_{el1} + n_{eh1} \quad (3.9c)$$

$$n_{el1} = n_{el0} \frac{T_{eff}}{T_{el}} \varphi_1 \quad (3.9d)$$

$$n_{eh1} = n_{eh0} \frac{T_{eff}}{T_{eh}} \varphi_1 \quad (3.9e)$$

Now in order to get the phase velocity relation we manipulate the linear equations (Eqs. 3.9a-3.9e) and arrive at the following relation:

$$\lambda_0 = v_0 + \sqrt{1 + 3\sigma} = v_0 + \sqrt{1 + 3T_i \frac{n_{el0}T_{eh} + n_{eh0}T_{el}}{n_0 T_{el} T_{eh}}} \quad (3.10)$$

The above equation (3.10) shows the *linear dispersion relation* of the wave, which is a result of linear analysis of the basic fluid equations that describes the present inhomogeneous plasma having trapped electrons.

It can be seen that the phase velocity λ_0 of the wave depends on ion and electron temperatures and their concentrations. The effect of ion and electron temperatures on the phase velocity of the wave can be seen in Figs. 3.2a and 3.2b. Figure 3.2a shows the increase in phase velocity of the wave as the ion temperature T_i is raised. The result is shown for two different concentrations of low-temperature electrons n_{el0} . Also, it is seen that higher concentration of low-temperature electrons gives rise to higher phase velocities, which was quite expected [19]. The increased phase velocity with the ion temperature and density of non-isothermal electrons can be explained based on a restoring force. Actually a larger restoring force acts on the ions during their oscillations

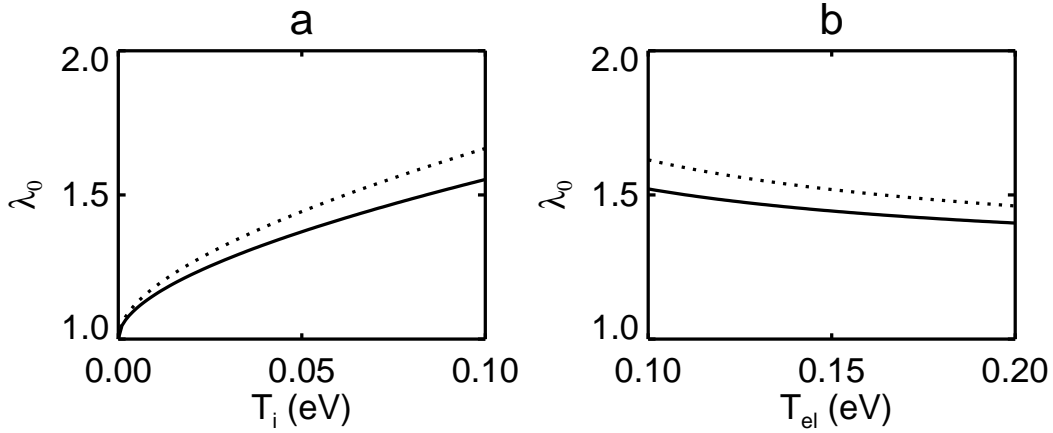


FIGURE 3.2: Dependence of phase velocity λ_0 of the wave on a) ion temperature T_i , provided $T_{el} = 0.1$ eV and b) on the temperature of trapped electrons T_{el} , provided $T_i = 0.09$ eV. The graphs are plotted for $n_{el0} = 0.04$ (solid line), and $n_{el0} = 0.06$ (dotted line), where $n_0 = 0.8$.

in the presence of higher ion temperature and a larger number of electrons. This results in the oscillations of higher frequency and the wave propagates with higher phase velocity. Figure 3.2b shows the decrease of phase velocity λ_0 under the effect of the temperature of trapped electrons T_{el} . It is seen that this decrease is evident in the case of plasma having a slightly higher concentration of low-temperature electrons. When we compare the solid and dotted line graphs in Figs. 3.2a and 3.2b, we observe that the effect of ion temperature is more pronounced on the phase velocity in the presence of a large number of non-isothermal electrons in the plasma. When we compare our results of unmagnetized plasma with that of magnetized plasma having negative ions [19], we note that the effect of electron temperature T_{el} remains the same on the phase velocity λ_0 in both types of the plasmas.

3.3 Nonlinear analysis: mKdV equation

In order to carry out the nonlinear analysis of the problem, we make use of the higher order equations, which are written as:

$$n_0 \frac{\partial}{\partial \xi} \varphi_2 + 3\sigma \frac{\partial}{\partial \xi} n_{i2} - n_0(\lambda_0 - v_0) \frac{\partial}{\partial \xi} v_2 + n_0 \lambda_0 \frac{\partial}{\partial \tau} \varphi_1 + n_0 v_0 \lambda_0 \frac{\partial}{\partial \tau} v_1 + \lambda_0(n_0 v_1 - n_{i1} v_0) \frac{\partial}{\partial \tau} v_0 + 3\sigma \lambda_0 \frac{\partial}{\partial \tau} n_{i1} = 0 \quad (3.11a)$$

$$n_0 \frac{\partial}{\partial \xi} v_2 - (\lambda_0 - v_0) \frac{\partial}{\partial \xi} n_{i2} \lambda_0 \frac{\partial}{\partial \tau} (n_0 v_1 - n_{i1} v_0) = 0 \quad (3.11b)$$

$$\frac{\partial^2}{\partial \xi^2} \varphi_1 + n_{i2} - n_{el2} - n_{eh2} = 0 \quad (3.11c)$$

$$n_{2l} = n_{0l} \left[\frac{T_{eff}}{T_{el}} \varphi_2 - \frac{4}{3} n_{0l} b_l \left(\frac{T_{eff}}{T_{el}} \right)^{3/2} \varphi_1^{3/2} \right] \quad (3.11d)$$

$$n_{2h} = n_{0h} \left[\frac{T_{eff}}{T_{eh}} \varphi_2 - \frac{4}{3} n_{0h} b_h \left(\frac{T_{eff}}{T_{eh}} \right)^{3/2} \varphi_1^{3/2} \right] \quad (3.11e)$$

The above Eqs. 3.11 together with linear Eqs. 3.9 lead to the following mKdV equation in terms of n_{i1} :

$$\frac{\partial}{\partial \tau} n_{i1} + \alpha n_{i1}^{1/2} \frac{\partial}{\partial \xi} n_{i1} + \beta \frac{\partial^3}{\partial \xi^3} n_{i1} + \gamma n_{i1} \frac{\partial}{\partial \tau} n_0 = 0 \quad (3.12)$$

Here the coefficients are given by

$$\alpha = \frac{2N}{n_0^{3/2} \lambda_0 (\lambda_0^2 + 1)}, \quad \beta = \frac{1}{n_0 \lambda_0^3 (\lambda_0^2 + 1)} \quad \text{and} \quad \gamma = \frac{2v_0^2 - \lambda_0^2}{n_0 \lambda_0^3 (\lambda_0^2 + 1)}.$$

$$\text{Where, } N = n_{el0} b_l \left(\frac{T_{eff}}{T_{el}} \right)^{3/2} + n_{eh0} b_h \left(\frac{T_{eff}}{T_{eh}} \right)^{3/2}.$$

It can be seen from Eq. 3.12 that inhomogeneity in the plasma has resulted into an extra term in the usual KdV equation. In order to find the solution of this mKdV equation, we use some transformation such that the density gradient term is encompassed into the nonlinear term. For this reason we use a transformation $n_1 = b(\tau) \tilde{n}(\xi, \tau)$ along with a new variable $b(\tau)$. Here

$$b(\tau) = \exp \left[- \int^\tau \gamma \left(\frac{\partial n_0}{\partial \tau'} \right) d\tau' \right]$$

which contains the density gradient term. Putting this transformation in Eq. 3.12, we get

$$\frac{\partial}{\partial \tau} \tilde{n} + \alpha b^{1/2} \tilde{n}^{1/2} \frac{\partial}{\partial \xi} \tilde{n} + \beta \frac{\partial^3}{\partial \xi^3} \tilde{n} = 0. \quad (3.13)$$

We get rid of the square root term by using another transformation $\tilde{n}^{1/2} = n$ in the previous equation so that it becomes

$$n \frac{\partial}{\partial \tau} n + \alpha b^{1/2} n^2 \frac{\partial}{\partial \xi} n + \beta \left(3 \frac{\partial}{\partial \xi} n \frac{\partial^2}{\partial \xi^2} n + n \frac{\partial^3}{\partial \xi^3} n \right) = 0. \quad (3.14)$$

Due to the variable coefficients, this equation is not solvable by the ordinary method of integration. Hence, we use an alternative method suggested by Yan [48]. This new transformation method can be obtained by the sine-Gordon equation and establishes a relation between linear and nonlinear theories. According to Yan, this method is simpler than the hyperbolic tangent method for solving differential equations. Since this method involves only *sine* and *cosine* functions, it is known as *sine-cosine method*, which gives traveling wave solutions to nonlinear wave equations. According to this method, the solution can be written as

$$n(\omega) = A_0 + \sum_{j=1}^p (B_j \sin \omega + A_j \cos \omega) \cos^{j-1} \omega, \quad \text{where} \quad \frac{d\omega}{d\zeta} = \sin \omega$$

or, in the form of hyperbolic functions

$$n(\zeta) = A_0 + \sum_{j=1}^p \tanh^{j-1} \zeta (B_j \operatorname{sech} \zeta + A_j \tanh \zeta)$$

In order to get a stationary solution following the sine-cosine method, we now transform the coordinates to the frame of reference of the soliton through $\zeta = g(\tau - U\xi)$, where g^{-1} is the width and U is the shift in the velocity when the wave evolves as a soliton. Here, p is determined by the balance of the leading order of nonlinear to linear terms. We find $p = 2$ in our case. With this, the solution in the form of the intermediate variable ω is written as

$$n(\omega) = A_0 + A_1 \cos \omega + B_1 \sin \omega + A_2 \cos^2 \omega + B_2 \cos \omega \sin \omega \quad (3.15)$$

Now, the aforementioned solution is substituted in Eq. 3.14, and then the coefficients of the various trigonometric identities are put equal to zero. Based on the values of the coefficients A_0 , A_1 , A_2 , B_1 and B_2 , we will have soliton solutions corresponding to Eq. 5.14. Through calculations, we noticed that some of these coefficients have more than one value (which is a drawback of the sine-cosine method), which means that an N-soliton solution is possible in the present plasma model. However, in order to obtain a single soliton solution and for the sake of simplicity, we set the values of A_1 , B_1 and B_2 as $A_1 = B_1 = B_2 = 0$. With this the coefficients of $\cos \omega$, $\cos^3 \omega$, $\cos^5 \omega$ and $\cos^7 \omega$ can be written as:

coefficient of $\cos \omega$:

$$-A_0 + \alpha\sqrt{g}UA_0^2 + 6\beta h^2U^3A_2 - 8\beta h^2U^3A_0 = 0$$

coefficient of $\cos^3 \omega$:

$$A_0 - A_2 - \alpha\sqrt{g}UA_0^2 + 2\alpha\sqrt{g}UA_0A_2 - 38\beta h^2U^3A_2 + 20\beta h^2U^3A_0 = 0$$

coefficient of $\cos^5 \omega$:

$$A_2 - 2\alpha\sqrt{g}UA_0A_2 + \alpha\sqrt{g}UA_2^2 + 62\beta h^2U^3A_2 - 12\beta h^2U^3A_0 = 0$$

coefficient of $\cos^7 \omega$:

$$\alpha\sqrt{g}UA_2 + 30\beta h^2U^3 = 0$$

Solving the above equations simultaneously, we find the values of the unknown variables as

$$A_0 = -A_2 = \frac{15}{8\alpha b^{1/2}U}, \quad \text{and} \quad g = \sqrt{\frac{1}{16\beta U^3}}$$

With these values, the solution in the form of hyperbolic functions can be written as

$$n = \frac{15}{8\alpha b^{1/2}U} \text{sech}^2 \left[\sqrt{\frac{1}{16\beta U^3}}(\tau - U\xi) \right]$$

Here, the peak amplitude of the soliton A_S , and the width of the soliton W_S are given as

$$A_S = \frac{15}{8\alpha b^{1/2}U} \quad \text{and} \quad W_S = g^{-1} = \sqrt{16\beta U^3}, \quad \text{respectively.}$$

Shown in Fig. 3.3 is the amplitude and width relation for the solitons discussed in the present case. This proportionality indicates that they are mKdV solitons, since they fulfill the mKdV criterion (Eq. 2.3) i.e. $A_S \times W_S = \text{Constant}$.

Our numerical calculations reveal that the solitons evolve as density hill (compressive soliton), as shown in Fig. 3.4. The soliton profile is plotted for two values of background density, showing the effect of the density gradient on the soliton profile, as the ion flow velocity is a measure of the density gradient. From this figure it is observed that the soliton evolves with higher amplitude and lower width in the presence of sharper density gradients. Hence, it is inferred that the effect of density gradient is to enhance the soliton peak amplitude. This is consistent with the result obtained by Malik and Nishida [49], in a magnetized plasma. We also notice that the density dip type profile (rarefactive soliton) does not occur in this plasma. The nonoccurrence of rarefactive solitons in the present plasma is similar to the result obtained by Gill *et al.* [50] in a homogeneous plasma with non-isothermal electrons using pseudo-potential approach.

Furthermore, the effects of the ion and electron temperatures and trapped electron concentrations on soliton width and peak amplitudes are shown in

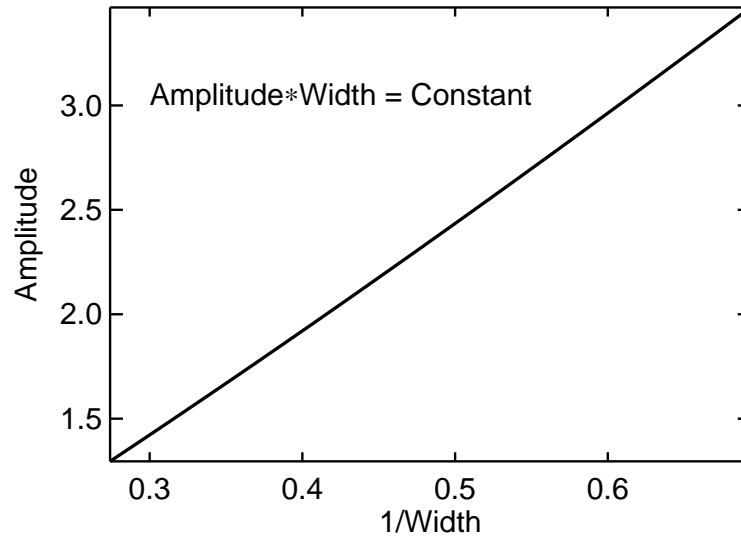


FIGURE 3.3: Relation between amplitude and width of the mKdV soliton, for T_i ranging from 0 to 0.1 eV, and $n_0 = 0.8$. All the other parameters are the same as in Fig. 3.4.

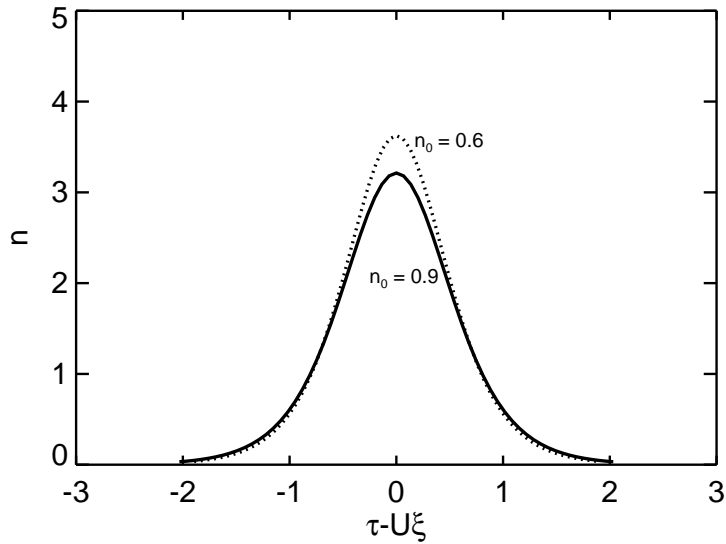


FIGURE 3.4: Soliton density profiles for two values of n_0 . Also, $T_i = 0.09$ eV, $T_{el} = 0.1$ eV, $T_{ch} = 5$ eV, $n_{el0} = 0.04$, $n_{eh0} = n_0 - n_{el0}$ and $U = 1.1$.

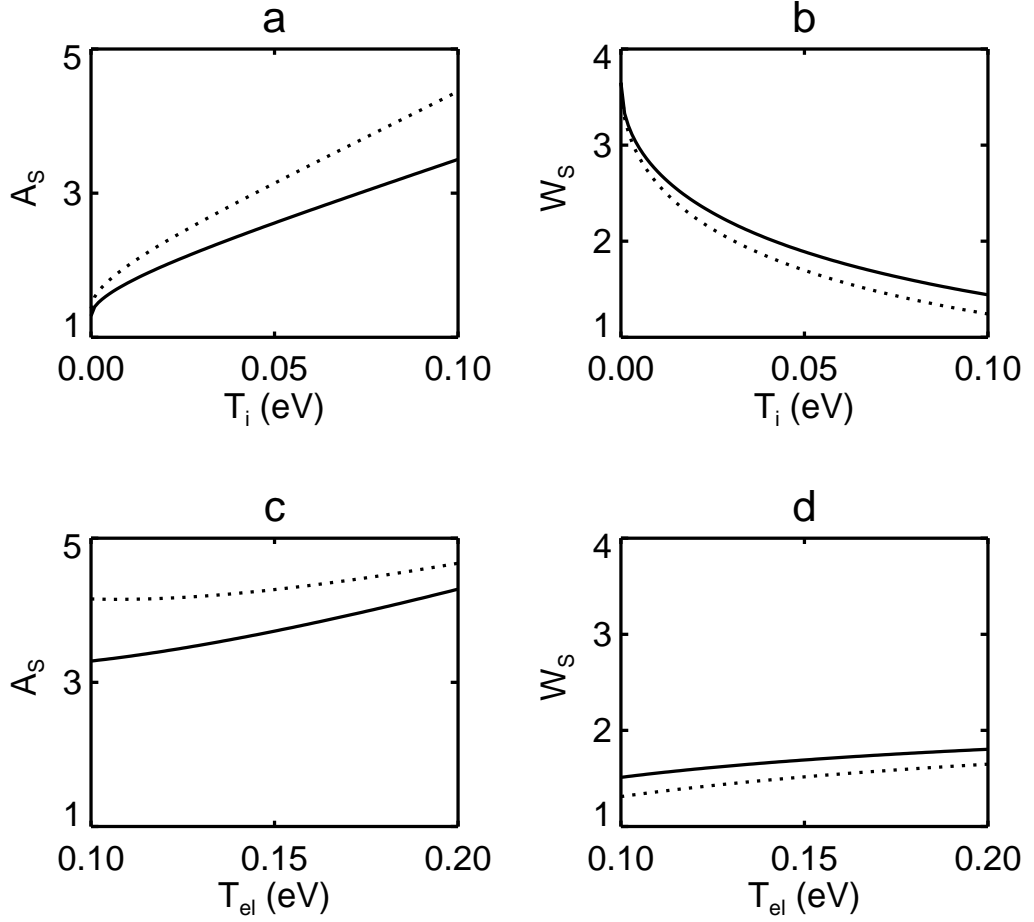


FIGURE 3.5: Dependence of a) soliton amplitude A_S and b) width W_S , on ion temperature T_i , provided $T_{el} = 0.1$ eV. Also, dependence of c) soliton amplitude A_S and d) width W_S , on the temperature of trapped electrons T_{el} , provided $T_i = 0.09$ eV. The graphs are plotted for $n_{el0} = 0.04$ (solid line), and $n_{el0} = 0.06$ (dotted line), where $n_0 = 0.8$ and $U = 1.1$.

Fig. 3.5. Figures 3.5a and 3.5b show an increase in the peak amplitude, and decrease in the width of the soliton, as T_i is increased. Apart from that, higher concentration of low-temperature electrons n_{el0} gives rise to narrower solitons with bigger peak amplitudes. The increasing soliton amplitude with the density n_{el0} is a similar result as obtained earlier in an inhomogeneous magnetized plasma [46]. Since the effective temperature T_{eff} goes down for the higher density n_{el0} , it can be said that the soliton amplitude increases with the decreasing T_{eff} . This is in agreement with the result of Goswami and Buti [17] obtained in an ordinary homogeneous unmagnetized plasma having positive ions and two-temperature electrons. Goswami and Buti proposed that decrease in T_{eff} results in the decrease of dispersion strength, thus for a fixed width, larger amplitudes are required to produce sharper gradients. So that for a given width, the dispersion effects are sufficient to produce solitons. This results in bigger solitons in the presence of lower values of T_{eff} . Also it is seen from the figures that the peak amplitude of the solitons shows a stronger dependence on ion temperature T_i when the concentration of low-temperature electrons is slightly higher. This is in accord with the behavior of phase velocity with T_i and n_{el0} . As discussed earlier, as a result of higher ion temperature the wave propagates with higher phase velocity. Then for the constant velocity shift U , the soliton would propagate with higher speed [51]. Since the soliton speed is directly linked to the soliton amplitude, the soliton evolves with higher amplitude for the case of higher ion temperature.

Figures 3.5c and 3.5d show an increase in both the peak amplitude A_S and width W_S of the soliton, as T_{el} is increased. With regard to the increase in soliton amplitude with the temperature of non-isothermal electrons, we recall that these electrons are trapped by the wave potential and interact strongly with the wave during its evolution [18]. Therefore, the nature of amplitude can be explained based on the wave particle interaction and the exchange of energy between them. The soliton energy being proportional to both amplitude and width, is significantly enhanced by the fact that increase in T_{el} results in the enhancement of both amplitude and the width of the soliton. Since the thermal speed of the electrons is enhanced with the rise in their temperature and it becomes larger than the velocity of the wave, there is a possibility that the energy is picked up by the wave during interaction. Due to this reason, the soliton would evolve with comparatively higher amplitudes and bigger widths in the presence of trapped electrons with higher temperature. However, we need to use the kinetic approach in order to better explain this wave-particle interaction. On the other hand, the increased soliton amplitude with n_{el0} can be explained on the basis of phase velocity λ_0 . Since this velocity gets larger in the case of higher n_{el0} , the soliton would evolve with higher amplitude and relatively smaller widths, when a larger number of low-temperature electrons are present in the plasma. It is thus deduced from the above discussion that low-temperature electrons, even if in a small quantity, affect the behavior of the solitons in a significant way.

Chapter 4

Oblique reflection of solitons in an inhomogeneous plasma: Effect of trapped electrons

In the previous chapter, the evolution of solitons in an inhomogeneous plasma was considered by taking one-dimensional motion of the ions. The main focus was to examine the contribution of trapped electrons to the soliton propagation characteristics. It was observed that a small amount of trapped electrons drastically modifies the soliton propagation. However, in the present chapter, we will deal with the problem of soliton reflection in the same plasma having trapped electrons. In order to generalize the problem, we consider the oblique propagation and reflection of the solitons. The detailed description of the geometry of the said problem is given in the next section.

4.1 Geometry of the problem

We consider an inhomogeneous plasma, which has finite temperature ions and two-temperature non-isothermal electrons. Due to the density gradient in the (x, z) plane, there is a background ion flow with velocity v_0 in the direction of decreasing density. In this plasma model, the propagation and reflection of the waves is considered to be oblique, i.e. at an angle θ with the z -axis. This density gradient is also responsible for the oblique reflection of the solitons. The physical mechanism behind this reflection process is explained in section 2.8. The oscillations are assumed in the (x, z) plane and the incident wave makes an angle θ_I with the z -axis. After striking with the reflector, it reflects, making angle θ_R with the z -axis. The unit wave vector along the wave propagation is taken as \hat{k} in the (x, z) plane. Hence $\hat{k} \cdot \vec{r} = x \sin \theta + z \cos \theta$, where \hat{k} could either be \hat{k}_I or \hat{k}_R . Similarly, θ could either be θ_I or θ_R . This is required to keep the obliqueness of the wave in our plasma model.

In order to investigate the propagation and reflection of solitons in such inhomogeneous plasma, we start with a set of 2-D fluid equations by considering

the plasma to be inter-penetrating fluid. We have normalized these equations in order to make them dimensionless for the sake of simplicity. This is done by employing the same normalization parameters as used in section 3.1. As earlier, we consider the unperturbed electric field and hence the unperturbed electric potential φ_0 to be zero.

These are the equation of continuity, equation of motion, Poisson's equation and the density distribution of the low- and high-temperature electrons:

$$\frac{\partial n_i}{\partial t} + \vec{\nabla} \cdot (n_i \vec{v}) = 0 \quad (4.1)$$

$$\frac{\partial \vec{v}}{\partial t} + (\vec{v} \cdot \vec{\nabla}) \vec{v} + \vec{\nabla} \varphi + \frac{2\sigma}{n_i} \vec{\nabla} n_i = 0 \quad (4.2)$$

$$\nabla^2 \varphi + n_i - n_{el} - n_{eh} = 0 \quad (4.3)$$

$$n_{el} = n_{el0} \left[1 + \frac{T_{eff}}{T_{el}} \varphi - \frac{4}{3} b_l \left(\frac{T_{eff}}{T_{el}} \varphi \right)^{3/2} + \frac{1}{2} \left(\frac{T_{eff}}{T_{el}} \varphi \right)^2 + \dots \right] \quad (4.4)$$

$$n_{eh} = n_{eh0} \left[1 + \frac{T_{eff}}{T_{eh}} \varphi - \frac{4}{3} b_h \left(\frac{T_{eff}}{T_{eh}} \varphi \right)^{3/2} + \frac{1}{2} \left(\frac{T_{eff}}{T_{eh}} \varphi \right)^2 + \dots \right] \quad (4.5)$$

In the above equations b_l and b_h are the non-isothermality parameters [45, 46, 19, 18], given as

$$b_l = \frac{(1 - T_{el}/T_{eff})}{\sqrt{\pi}} \quad \text{and} \quad b_h = \frac{(1 - T_{eh}/T_{eff})}{\sqrt{\pi}}.$$

We take the angle of incidence as θ_I in view of the oblique incidence of the wave. By taking λ_{0I} as the phase velocity of the wave, we introduce the following stretched coordinates. [19, 46, 47, 52]

$$\xi_I = \epsilon^{1/4} \left(\frac{x \sin \theta_I + z \cos \theta_I}{\lambda_{0I}} - t \right), \quad \tau_I = \epsilon^{3/4} (x \sin \theta_I + z \cos \theta_I)$$

The reductive perturbation technique, as explained in the previous chapters, requires the expansion of dependent quantities (like densities, velocities, potential etc.) about their equilibrium position in the form of a small parameter ϵ , the smallness of which determines the order/strength of the perturbation. We expand the densities, fluid velocities and electric potential in terms of ϵ by taking into account the oblique incidence of the wave, as follows [31, 52]:

$$f = f_0(x, z) + \epsilon f_1(x, z, t) + \epsilon^{3/2} f_2(x, z, t) + \epsilon^2 f_3(x, z, t) + \dots \quad (4.6)$$

$$\text{where, } f \equiv n_i, n_{el}, n_{eh}, \varphi, v_x, v_z.$$

From the above equations it can be seen that the unperturbed quantities are functions of space coordinates x and z , and the perturbed quantities are the functions of both space and time coordinates. v_{0x} and v_{0z} are the x and z components of the background ion flow velocity, respectively.

4.2 mKdV equation for incident soliton

Now we derive the relevant mKdV equation for the obliquely incident soliton. Since the plasma is inhomogeneous in space only, the unperturbed quantities are taken to be functions of the space coordinate τ_I only, which means

$$\frac{\partial n_0}{\partial \xi_I} = \frac{\partial n_{el0}}{\partial \xi_I} = \frac{\partial n_{eh0}}{\partial \xi_I} = \frac{\partial v_{x0}}{\partial \xi_I} = \frac{\partial v_{z0}}{\partial \xi_I} = 0$$

As per the reductive perturbation approach, the set of stretched coordinates and the expansion of physical quantities are used in the basic fluid equations. Through this we get various expressions with different powers of ϵ . The expansion parameter cannot be neglected, as it represents the perturbation in the medium, that is responsible for the excitation of the wave and its evolution as a soliton. Hence, the coefficients of ϵ^0 , $\epsilon^{1/2}$, ϵ , $\epsilon^{3/2}$, ϵ^2 , $\epsilon^{5/2}$ etc. are separately put to zero, which gives rise to various equations in zeroth, first and second ordered quantities. This way the zeroth ordered equations are obtained as follows:

$$(v_{0x} \sin \theta_I + v_{0z} \cos \theta_I) \frac{\partial}{\partial \tau_I} n_0 + n_0 (\sin \theta_I \frac{\partial}{\partial \tau_I} v_{0x} + \cos \theta_I \frac{\partial}{\partial \tau_I} v_{0z}) = 0 \quad (4.7)$$

$$n_0 (v_{0x} \sin \theta_I + v_{0z} \cos \theta_I) \frac{\partial}{\partial \tau_I} v_{0x} + 2\sigma \sin \theta_I \frac{\partial}{\partial \tau_I} n_0 = 0 \quad (4.8)$$

$$n_0 (v_{0x} \sin \theta_I + v_{0z} \cos \theta_I) \frac{\partial}{\partial \tau_I} v_{0z} + 2\sigma \cos \theta_I \frac{\partial}{\partial \tau_I} n_0 = 0 \quad (4.9)$$

$$n_0 = n_{el0} + n_{eh0} \quad (4.10)$$

The first order equations are given as:

$$(v_{0x} \sin \theta_I + v_{0z} \cos \theta_I - \lambda_{0I}) \frac{\partial}{\partial \xi_I} n_1 + n_0 (\sin \theta_I \frac{\partial}{\partial \xi_I} v_{1x} + \cos \theta_I \frac{\partial}{\partial \xi_I} v_{1z}) = 0 \quad (4.11)$$

$$n_0 (v_{0x} \sin \theta_I + v_{0z} \cos \theta_I - \lambda_{0I}) \frac{\partial}{\partial \xi_I} v_{1x} + n_0 \sin \theta_I \frac{\partial}{\partial \xi_I} \varphi_1 + 2\sigma \sin \theta_I \frac{\partial}{\partial \xi_I} n_1 = 0 \quad (4.12)$$

$$n_0 (v_{0x} \sin \theta_I + v_{0z} \cos \theta_I - \lambda_{0I}) \frac{\partial}{\partial \xi_I} v_{1z} + n_0 \cos \theta_I \frac{\partial}{\partial \xi_I} \varphi_1 + 2\sigma \cos \theta_I \frac{\partial}{\partial \xi_I} n_1 = 0 \quad (4.13)$$

$$n_1 = n_{el1} + n_{eh1} \quad (4.14)$$

$$n_{el1} = n_{el0} \frac{T_{eff}}{T_{el}} \varphi_1 \quad (4.15)$$

$$n_{eh1} = n_{eh0} \frac{T_{eff}}{T_{eh}} \varphi_1 \quad (4.16)$$

We use the linear equations to reach the phase velocity relation for the incident wave:

$$\lambda_{0I} = v_{0x} \sin \theta_I + v_{0z} \cos \theta_I + \sqrt{(1 + 2\sigma)} \quad (4.17)$$

The second order equations in terms of the smallness parameter ϵ are then collected in order to obtain:

$$\begin{aligned}
& (v_{0x} \sin \theta_I + v_{0z} \cos \theta_I - \lambda_{0I}) \frac{\partial}{\partial \xi_I} n_2 + n_0 (\sin \theta_I \frac{\partial}{\partial \xi_I} v_{2x} + \cos \theta_I \frac{\partial}{\partial \xi_I} v_{2z}) \\
& + \lambda_{0I} (v_{0x} \sin \theta_I + v_{0z} \cos \theta_I) \frac{\partial}{\partial \tau_I} n_1 + \lambda_{0I} (v_{1x} \sin \theta_I + v_{1z} \cos \theta_I) \frac{\partial}{\partial \tau_I} n_2 \\
& + n_0 \lambda_{0I} (\sin \theta_I \frac{\partial}{\partial \tau_I} v_{1x} + \cos \theta_I \frac{\partial}{\partial \tau_I} v_{1z}) + n_1 \lambda_{0I} (\sin \theta_I \frac{\partial}{\partial \tau_I} v_{0x} + \cos \theta_I \frac{\partial}{\partial \tau_I} v_{0z}) = 0
\end{aligned} \tag{4.18}$$

$$\begin{aligned}
& n_0 (v_{0x} \sin \theta_I + v_{0z} \cos \theta_I - \lambda_{0I}) \frac{\partial}{\partial \xi_I} v_{2x} + n_0 \sin \theta_I \frac{\partial}{\partial \xi_I} \varphi_2 + 2\sigma \sin \theta_I \frac{\partial}{\partial \xi_I} n_2 \\
& + n_0 \lambda_{0I} (v_{0x} \sin \theta_I + v_{0z} \cos \theta_I) \frac{\partial}{\partial \tau_I} v_{1x} + n_0 \lambda_{0I} (v_{1x} \sin \theta_I + v_{1z} \cos \theta_I) \frac{\partial}{\partial \tau_I} v_{0x} \\
& + n_0 \lambda_{0I} \sin \theta_I \frac{\partial}{\partial \tau_I} \varphi_1 + n_1 \lambda_{0I} (v_{0x} \sin \theta_I + v_{0z} \cos \theta_I) \frac{\partial}{\partial \tau_I} v_{0x} + 2\sigma \lambda_{0I} \sin \theta_I \frac{\partial}{\partial \tau_I} n_1 = 0
\end{aligned} \tag{4.19}$$

$$\begin{aligned}
& n_0 (v_{0x} \sin \theta_I + v_{0z} \cos \theta_I - \lambda_{0I}) \frac{\partial}{\partial \xi_I} v_{2z} + n_0 \cos \theta_I \frac{\partial}{\partial \xi_I} \varphi_2 + 2\sigma \cos \theta_I \frac{\partial}{\partial \xi_I} n_2 \\
& + n_0 \lambda_{0I} (v_{0x} \sin \theta_I + v_{0z} \cos \theta_I) \frac{\partial}{\partial \tau_I} v_{1z} + n_0 \lambda_{0I} (v_{1x} \sin \theta_I + v_{1z} \cos \theta_I) \frac{\partial}{\partial \tau_I} v_{0z} \\
& + n_0 \lambda_{0I} \cos \theta_I \frac{\partial}{\partial \tau_I} \varphi_1 + n_1 \lambda_{0I} (v_{0x} \sin \theta_I + v_{0z} \cos \theta_I) \frac{\partial}{\partial \tau_I} v_{0z} + 2\sigma \lambda_{0I} \cos \theta_I \frac{\partial}{\partial \tau_I} n_1 = 0
\end{aligned} \tag{4.20}$$

$$\frac{1}{\lambda_{0I}^2} \frac{\partial^2}{\partial \xi_I^2} \varphi_1 + n_2 - n_{el2} - n_{eh2} = 0 \tag{4.21}$$

$$n_{el2} = n_{el0} \left[\frac{T_{eff}}{T_{el}} \varphi_2 - \frac{4}{3} n_{el0} b_l \left(\frac{T_{eff}}{T_{el}} \right)^{3/2} \varphi_1^{3/2} \right] \tag{4.22}$$

$$n_{eh2} = n_{eh0} \left[\frac{T_{eff}}{T_{eh}} \varphi_2 - \frac{4}{3} n_{eh0} b_h \left(\frac{T_{eff}}{T_{eh}} \right)^{3/2} \varphi_1^{3/2} \right] \tag{4.23}$$

The aforementioned equations are used to derive the mKdV equation for the incident solitons in terms of the perturbed velocity v_{1z} . We write it in the form of v_{1I} in order to distinguish it from the reflecting case and obtain the following mKdV equation

$$\frac{\partial}{\partial \tau_I} v_{1I} + \alpha_I v_{1I}^{1/2} \frac{\partial}{\partial \xi_I} v_{1I} + \beta_I \frac{\partial^3}{\partial \xi_I^3} v_{1I} + \gamma_I v_{1I} \frac{\partial}{\partial \tau_I} n_0 = 0 \tag{4.24}$$

Here, the various coefficients are given by

$$\alpha_I = \frac{2N}{n_0 \lambda_{0I} \sqrt{(\cos \theta_I (\lambda_{0I} - v_{0I})) (\lambda_{0I}^2 + 1 + 2\sigma - v_{0I}^2)}}$$

$$\beta_I = \frac{1}{n_0 \lambda_{0I}^3 (\lambda_{0I}^2 + 1 + 2\sigma - v_{0I}^2)}$$

$$\gamma_I = \frac{1}{n_0} \left[\frac{v_{0I} (4\lambda_{0I}^2 + 4\sigma + 1) - \lambda_{0I} (3v_{0I}^2 + \lambda_{0I}^2 + 2\sigma)}{(\lambda_{0I}^2 + 1 + 2\sigma - v_{0I}^2) (v_{0I} - \lambda_{0I})} \right]$$

Where, $v_{0I} = v_{0x} \sin \theta_I + v_{0z} \cos \theta_I$,

$$\text{and } N = n_{el0} b_l \left(\frac{T_{eff}}{T_{el}} \right)^{3/2} + n_{eh0} b_h \left(\frac{T_{eff}}{T_{eh}} \right)^{3/2}.$$

It can be noticed from Eq. 4.24 that the usual KdV equation is modified by the different nonlinear term (second term) along with an additional last term that shows the effect of the density inhomogeneity in the plasma. In order to find the solution of the mKdV equation, we use a transformation $v_{1I} = b_I(\tau_I) \tilde{v}_I(\xi_I, \tau_I)$ where

$$b_I(\tau_I) = \exp \left[- \int^{\tau_I} \gamma_I \left(\frac{\partial n_0}{\partial \tau'_I} \right) d\tau'_I \right]$$

for accommodating the density gradient term in the nonlinear term through a new variable b_I . Putting this transformation in Eq. 4.24, we get

$$\frac{\partial}{\partial \tau_I} \tilde{v}_{1I} + \alpha_I b_I^{1/2} \tilde{v}_{1I}^{1/2} \frac{\partial}{\partial \xi_I} \tilde{v}_{1I} + \beta_I \frac{\partial^3}{\partial \xi_I^3} \tilde{v}_{1I} = 0 \quad (4.25)$$

Now, we further put $\tilde{v}_{1I}^{1/2} = v_I$ in the previous equation so that it becomes

$$v_I \frac{\partial}{\partial \tau_I} v_I + \alpha_I b_I^{1/2} v_I^2 \frac{\partial}{\partial \xi_I} v_I + \beta_I \left(3 \frac{\partial}{\partial \xi_I} v_I \frac{\partial^2}{\partial \xi_I^2} v_I + v_I \frac{\partial^3}{\partial \xi_I^3} v_I \right) = 0 \quad (4.26)$$

Due to the variable coefficients, this equation is not solvable by the ordinary method of integration. Hence, we use an alternative method called sine-cosine method, explained in section 3.3. According to this method, the solution can be written as

$$v_I(\omega_I) = A_{0I} + \sum_{j=1}^p (B_{jI} \sin \omega_I + A_{jI} \cos \omega_I) \cos^{j-1} \omega_I, \quad \text{where } \frac{d\omega}{d\zeta_I} = \sin \omega_I$$

or, in the form of hyperbolic functions

$$v_I(\zeta_I) = A_{0I} + \sum_{j=1}^p \tanh^{j-1} \zeta_I (B_{jI} \operatorname{sech} \zeta_I + A_{jI} \tanh \zeta_I).$$

In order to get a stationary solution, we now transform the coordinates to the frame of reference of soliton through $\zeta_I = g_I(\tau_I - U_I \xi_I)$, where g_I^{-1} is the

width and U_I is the shift in the velocity when the wave evolves as a soliton. Here, $p = 2$ in our case. With this, the solution in the form of intermediate variable ω_I is written as

$$v_I(\omega_I) = A_{0I} + A_{1I} \cos \omega_I + B_{1I} \sin \omega_I + A_{2I} \cos^2 \omega_I + B_{2I} \cos \omega_I \sin \omega_I$$

Now, the solution is found out using exactly the same procedure as explained in the previous chapter. Hence, we reach the solution

$$v_I = \frac{15}{8\alpha b_I^{1/2} U_I} \operatorname{sech}^2 \left[\sqrt{\frac{1}{16\beta_I U_I^3}} (\tau_I - U_I \xi_I) \right]$$

Here, the peak amplitude of the soliton A_I , and the width of the soliton W_I are given as

$$A_I = \frac{15}{8\alpha b_I^{1/2} U_I} \quad \text{and} \quad W_I = g_I^{-1} = \sqrt{16\beta_I U_I^3}, \quad \text{respectively.}$$

4.3 mKdV equation for reflected solitons

As discussed in section 2.8, the density inhomogeneity is an important factor for the soliton reflection. In the earlier investigations [28, 29, 31], it was assumed that the incident soliton propagating in the \hat{k} direction gets reflected in the $-\hat{k}$ direction. However, due to the density gradients existing in the x - as well as in the z -directions in the present plasma, in general, the soliton may reflect in another direction also. In order to generalize this situation and, hence, in the interest of oblique reflection, we take the angle of reflection as $\theta_R \neq \theta_I$.

In view of such a reflection, the appropriate stretched coordinates are taken as

$$\xi_R = \epsilon^{1/4} \left(-\frac{x \sin \theta_R + z \cos \theta_R}{\lambda_{0R}} - t \right), \quad \text{and} \quad \tau_R = -\epsilon^{3/4} (x \sin \theta_R + z \cos \theta_R)$$

Then, just like the incident case, the reductive perturbation technique is used to get the phase velocity relation for the reflected wave. Therefore, the zeroth order and linear equations give rise to the following phase velocity relation:

$$\lambda_{0R} = -(v_{0x} \sin \theta_R + v_{0z} \cos \theta_R) + \sqrt{(1 + 2\sigma)} \quad (4.27)$$

The higher order equations then give rise to the following mKdV equation for the reflected wave:

$$\frac{\partial}{\partial \tau_R} v_{1R} + \alpha_R v_{1R}^{1/2} \frac{\partial}{\partial \xi_R} v_{1R} + \beta_R \frac{\partial^3}{\partial \xi_R^3} v_{1R} + \gamma_R v_{1R} \frac{\partial}{\partial \tau_R} n_0 = 0 \quad (4.28)$$

Here the various coefficients are given by

$$\alpha_R = \frac{2N}{n_0 \lambda_{0R} \sqrt{(\cos \theta_R (\lambda_{0R} - v_{0R})) (\lambda_{0R}^2 + 1 + 2\sigma - v_{0R}^2)}}$$

$$\beta_R = \frac{1}{n_0 \lambda_{0R}^3 (\lambda_{0R}^2 + 1 + 2\sigma - v_{0R}^2)}$$

$$\gamma_R = \frac{1}{n_0} \left[\frac{v_{0R}(4\lambda_{0I}^2 + 4\sigma + 1) - \lambda_{0R}(3v_{0R}^2 + \lambda_{0R}^2 + 2\sigma)}{(\lambda_{0R}^2 + 1 + 2\sigma - v_{0R}^2)(v_{0R} - \lambda_{0R})} \right]$$

together with $v_{0R} = -(v_{0x} \sin \theta_R + v_{0z} \cos \theta_R)$.

N is the same as defined for the incident soliton case. Now, we will couple the mKdV equations, i.e., Eq. 4.26 and 4.28, by replacing v_{1R} in Eq. 4.28 by $v_{1R} + v_I$, which is the total ion fluid velocity [28]. It is to be kept in mind that v_I is independent of τ_R and ξ_R . This way, the coupled equation is obtained as

$$\frac{\partial}{\partial \tau_R} v_{1R} + \alpha_R (v_I + v_{1R})^{1/2} \frac{\partial}{\partial \xi_R} v_{1R} + \beta_R \frac{\partial^3}{\partial \xi_R^3} v_{1R} + \gamma_R (v_I + v_{1R}) \frac{\partial}{\partial \tau_R} n_0 = 0 \quad (4.29)$$

In view of earlier results, we use the approximation $v_{1R} \ll v_I$ and substitute $v_{1R} = b_R(\tau_R) \tilde{v}_R(\xi_R, \tau_R)$, where

$$b_R(\tau_R) = \exp \left[- \int^{\tau_R} \gamma_R \left(\frac{\partial n_0}{\partial \tau'_R} \right) d\tau'_R \right]$$

With this the aforementioned equation takes the form

$$\frac{\partial}{\partial \tau_R} \tilde{v}_R + \alpha_R \left(\sqrt{v_I} + \frac{b_R \tilde{v}_R}{2\sqrt{v_I}} \right) \frac{\partial}{\partial \xi_R} \tilde{v}_R + \beta_R \frac{\partial^3}{\partial \xi_R^3} \tilde{v}_R + \gamma_R \frac{v_I}{b_R} \frac{\partial}{\partial \tau_R} n_0 = 0 \quad (4.30)$$

Now, we make another transformation, $\tilde{v}_R(\xi_R, \tau_R) = h_R(\tau_R) + v_R(\xi_R, \tau_R)$, where

$$h_R(\tau_R) = - \int^{\tau_R} \left(\frac{\gamma_R}{b_R} \right) v_I \left(\frac{\partial n_0}{\partial \tau'_R} \right) d\tau'_R$$

for coupling the density gradient term with the nonlinear term through the variable h_R . With this transformation, the previous equation becomes

$$\frac{\partial}{\partial \tau_R} v_R + \alpha_R \left(\sqrt{v_{1I}} + \frac{b_R h_R}{2\sqrt{v_{1I}}} \right) \frac{\partial}{\partial \xi_R} v_R + \alpha_R \frac{b_R}{2\sqrt{v_{1I}}} v_R \frac{\partial}{\partial \xi_R} v_R + \beta_R \frac{\partial^3}{\partial \xi_R^3} v_R = 0 \quad (4.31)$$

Following the same method as used for the incident case, we write the solution of this equation in the following form:

$$v_R(\omega_R) = A_{0R} + A_{1R} \cos \omega_R + B_{1R} \sin \omega_R + A_{2R} \cos^2 \omega_R + B_{2R} \cos \omega_R \sin \omega_R$$

$$\text{Here, } \frac{d\omega}{d\xi_R} = \sin \omega_R \quad \text{and} \quad \zeta_R = g_R(\tau_R - U_R \xi_R).$$

Now, we follow exactly the same procedure as in the incident case and reach the final solution of the mKdV equation (4.31) as

$$v_R = S_R + A_R \text{sech}^2 [W_R^{-1}(\tau_R - U_R \xi_R)] \quad (4.32)$$

$$\text{Here } S_R = \frac{2\sqrt{v_I}}{\alpha_R b_R U_R} (1 - 4\beta_R g_R^2 U_R^3) - \frac{2v_I}{b_R} - h_R$$

is the down-shift that the solitons undergo after reflection [46, 53]. The amplitude A_R comes out to be

$$A_R = 24\sqrt{v_I} \frac{\beta_R U_R^2}{\alpha_R b_R} g_R^2.$$

The value of g_R is calculated from the mKdV criterion (Eq. 2.3), according to which, the product of amplitude and width remains constant i.e. $A_I \times W_I = A_R \times W_R$. Using this criterion, we arrive at the relation for the reflected soliton width W_R

$$W_R = g_R^{-1} = \frac{64}{5} \sqrt{v_I} \frac{\beta_R U_R^2}{\alpha_R b_R} g_I \alpha_I U_I \sqrt{b_I}.$$

4.4 Results and discussion

So far we have obtained the expressions for the amplitudes and widths of both the incident and reflected solitons. It is obvious from the analysis that when the ion-acoustic wave of phase velocity λ_{0I} is evolved as incident soliton, a velocity shift amounting to U_I takes place. Also, for the propagation of the wave, and hence of the soliton, this phase velocity should be positive. Since the direction of \hat{k} has already been taken into account while writing the stretched coordinates for obtaining the phase velocity relation for the reflected wave, the phase velocity λ_{0R} should be positive for the propagation of the wave. In this regard, it can be seen from Eq. 4.27 that the phase velocity λ_{0R} will attain positive values if the following inequality is satisfied in the plasma:

$$\sqrt{(1 + 2\sigma)} \geq (v_{0x} \sin \theta_R + v_{0z} \cos \theta_R)$$

The aforementioned inequality reveals that there is a limit on the angle of reflection θ_R beyond which the soliton reflection is not possible. If we assume $v_{0x} = v_{0z} = v_0$, then the maximum possible value of angle θ_R is obtained as

$$\theta_{Rmax} = \frac{1}{2} \sin^{-1} \left[\left(1 + \frac{2T_i(n_{el0}T_{eh} + n_{eh0}T_{el})}{(n_{el0} + n_{eh0})T_{el}T_{eh}} - v_0^2 \right) / v_0^2 \right] \quad (4.33)$$

Clearly, the obliqueness of reflection is decided by plasma parameters including the ion temperature, ion drift velocity, and the densities and temperatures of low- and high-temperature electrons. This limit on the obliqueness θ_R is a new element of the present investigation of soliton reflection, in addition to the effect of the temperature and density of the trapped electrons. Keeping in view this limit of the angle θ_R , now, the reflection of the solitons is analyzed by observing the dependence of the reflected soliton amplitude and reflection coefficient (the ratio of reflected soliton amplitude and incident soliton amplitude) on the temperature and densities of the electrons and ions.

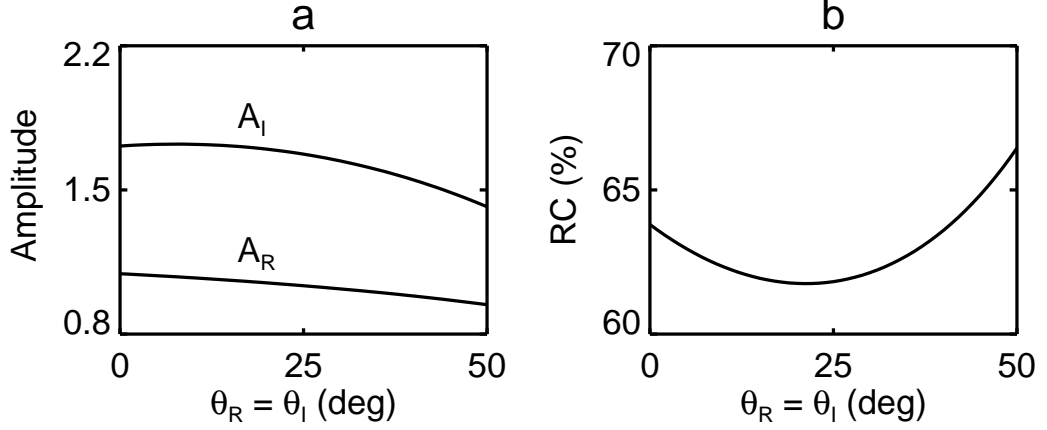


FIGURE 4.1: Dependence of a) incident and reflected soliton amplitudes A_I and A_R , and b) Reflection coefficient RC , on obliqueness $\theta_I (= \theta_R)$. Here $T_i = 0.09$ eV, $T_{el} = 0.1$ eV, $T_{eh} = 5$ eV, $n_0 = 0.8$, $n_{el0} = 0.04$, $n_{eh0} = n_0 - n_{el0}$, $U_I = 1.1$, $U_R = 1.3$ and $v_{0x} = v_{0z} = 0.04$.

The angle of incidence θ_I generally depends on the mode of excitation of solitons and can be changed by tilting the reflector [38], but the angle of reflection θ_R is determined by the plasma properties like temperature and density. For the sake of analyzing the behavior of solitons with respect to obliqueness, the angle of incidence θ_I is taken to be equal to the angle of reflection i.e. $\theta_I = \theta_R$, although this is not the case in general. The effect of obliqueness on the amplitude of the incident and reflected soliton A_R can be seen from Fig. 4.1a. For smaller angles of incidence we observe a very slight dependence of the incident soliton amplitude A_I on the obliqueness. As obliqueness increases, we observe a decrease in A_I , and a similar behavior is shown by the reflected amplitude A_R . This figure shows that the soliton gets reflected with lower amplitude if the reflection takes place at larger obliqueness. It means the reflected soliton shall carry relatively lower energy in the present case of oblique reflection. Hence, a bigger reflected soliton is possible when the normal reflection takes place.

The strength of reflection is presented in the form of the reflection coefficient $RC = (A_R/A_I) \times 100$. Figure 4.1b shows the effect of obliqueness on the reflection coefficient RC . Here, it is observed that the reflection coefficient first decreases and then increases with angle. The initial decrease in RC is attributed to the stronger dependence of A_R on the obliqueness as compared to A_I . For bigger angles we observe an increase in RC , due to the fact that A_I decreases with angle strongly as compared to A_R .

In Fig. 4.2, the effect of ion temperature T_i is shown on the peak amplitudes and widths of the incident and the reflected solitons. In Figs. 4.2a and 4.2b, it is observed that higher ion temperature gives rise to taller and narrower incident

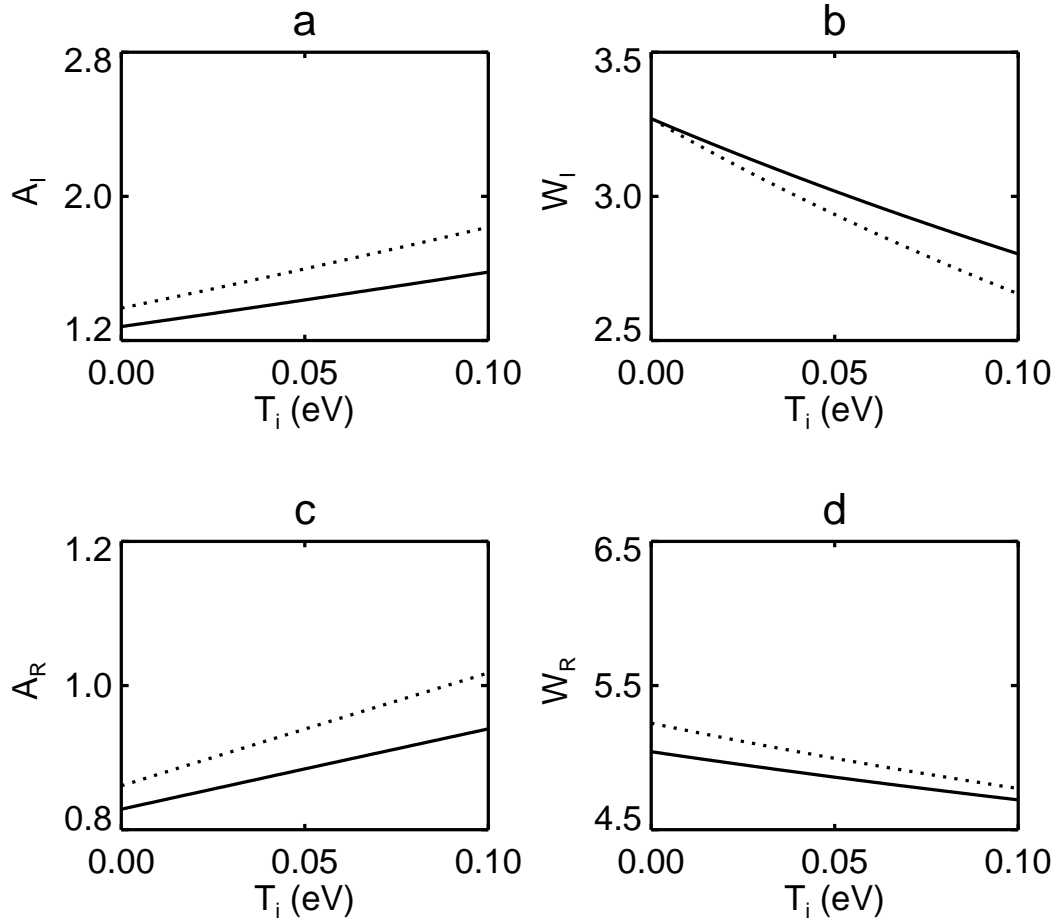


FIGURE 4.2: Dependence of incident soliton a) amplitude A_I , b) width W_I , and reflected soliton c) amplitude A_R , d) width W_R , on ion temperature T_i . Here, $\theta_I = 40^\circ$ and $\theta_R = 30^\circ$. The graphs are plotted for $n_{el0} = 0.04$ (solid line), and $n_{el0} = 0.06$ (dotted line). All the other parameters are the same as used in Fig. 4.1.

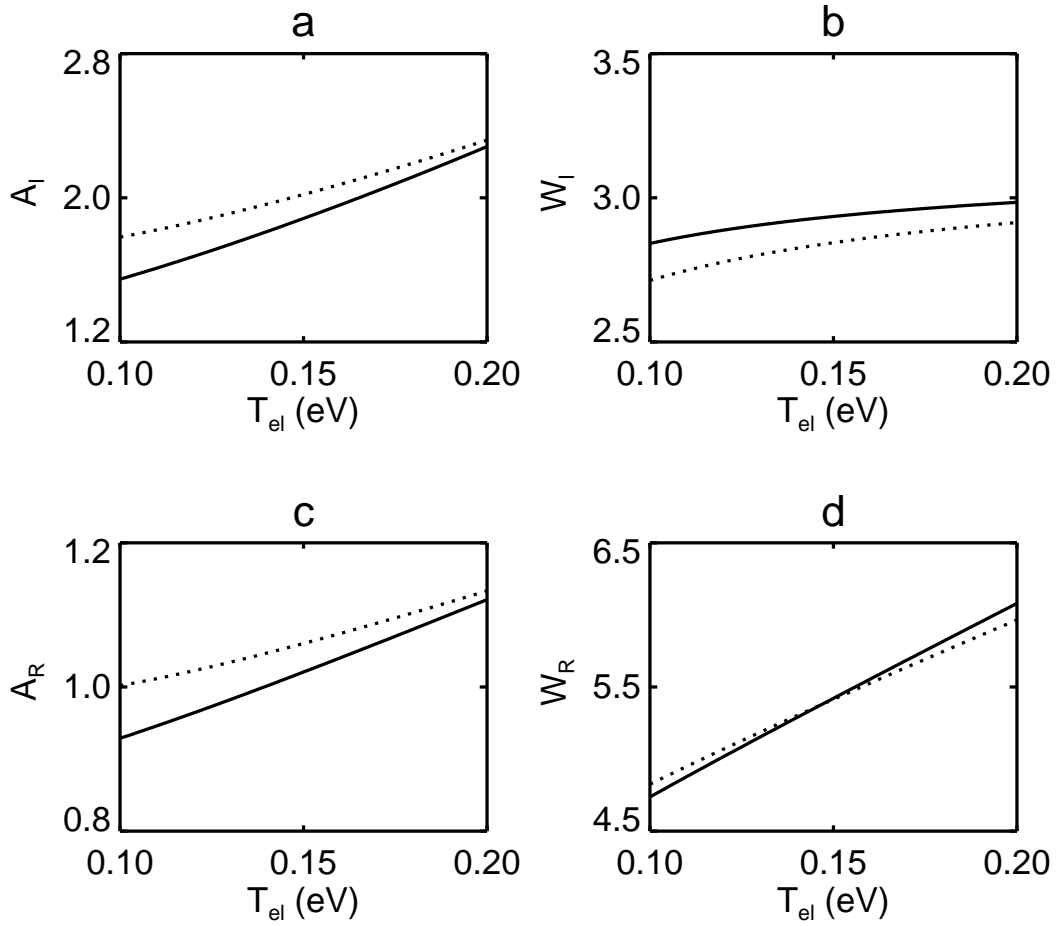


FIGURE 4.3: Dependence of incident soliton a) amplitude A_I , b) width W_I , and reflected soliton c) amplitude A_R , d) width W_R , on trapped electron temperature T_{el} . The graphs are plotted for $n_{el0} = 0.04$ (solid line), and $n_{el0} = 0.06$ (dotted line). Here, $T_i = 0.09$ eV, and all the other parameters are the same as used in Fig. 4.2.

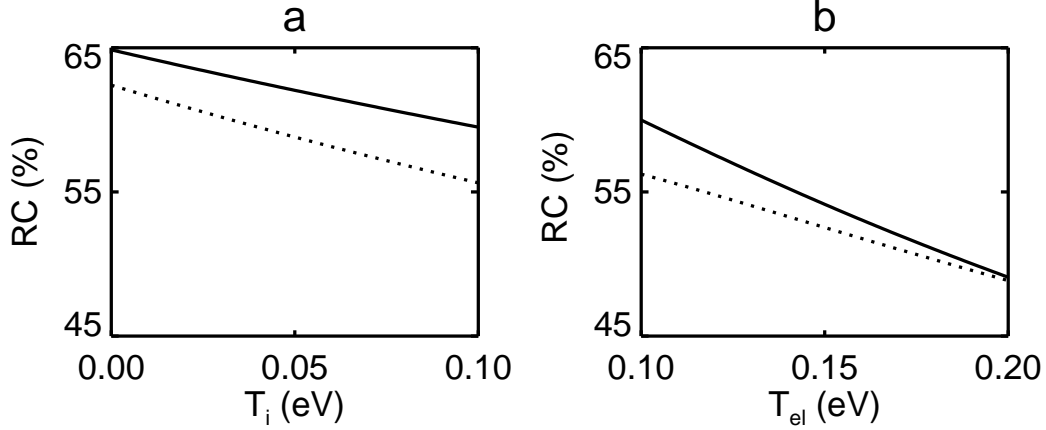


FIGURE 4.4: a) Dependence of reflection coefficient $RC\%$ on ion temperature T_i , provided $T_{el} = 0.1$ eV. b) Dependence of reflection coefficient $RC\%$ on trapped electron temperature T_{el} , provided $T_i = 0.09$ eV. The graphs are plotted for $n_{el0} = 0.04$ (solid line), and $n_{el0} = 0.06$ (dotted line). All the other parameters are the same as used in Fig. 4.2.

solitons. The same effect was observed for the incident soliton illustrated in the previous chapter. The increase in amplitude is due to the fact that the ion temperatures tend to increase the phase velocity. It has already been established that, for a constant velocity shift U_I , the higher phase velocity gives rise to faster solitons. The speed being directly related to the amplitude of the soliton then explains the evolution of taller solitons in the presence of higher ion temperature. The reflected solitons show a similar behavior, as seen in Figs. 4.2c and 4.2d. When the slopes of this figure are closely examined it becomes clear that the incident soliton has a stronger dependence on T_i than the reflected soliton. The graphs are plotted for two values of low-temperature (trapped) electron density n_{el0} . A comparison of solid and dotted graphs represents that a higher concentration of trapped electrons gives rise to solitons which have bigger peak amplitudes. Here, it seems that during wave particle interaction, the energy picked up by the wave and, hence, by the soliton is more when low-temperature (trapped) electrons are present in higher concentration. If we focus on the slopes of the graphs, we realize that the effect of obliqueness is more prominent in the presence of a large number of low-temperature electrons. The dotted plots in the Fig. 4.2 also show that the effect of ion temperature is more significant when more trapped electrons are present in the plasma.

The effect of temperature of trapped electrons T_{el} on the soliton characteristics is shown in Fig. 4.3. Figures 4.3a and 4.3b show that the amplitude and width of the incident soliton increase with the increase in trapped electron temperature. From this we can deduce that the energy of the soliton

varies strongly with T_{el} . This is attributed to the change in soliton energy, being directly proportional to the square of its amplitude. Thus, when both amplitude and width of the soliton increase, we expect a significant increase in the soliton energy, too. Figures 4.3c and 4.3d show the similar effects of T_{el} on the reflected soliton amplitude and width. The slopes of the plots demonstrate that the effect of T_{el} on reflected soliton is weaker in comparison with the incident case. The graphs are plotted for two different concentrations of low-temperature electrons. It is, however, interesting to note that the presence of less trapped electrons results in a stronger dependence of soliton amplitude and width on the trapped electron temperature. This statement is derived by comparing dotted and solid graphs in Fig. 4.3.

Figure 4.4a illustrates the effect of T_i on the reflection coefficient RC . RC being the ratio of A_R to A_I decreases with the increase in T_i due to the fact that A_I has a stronger dependence on T_i as compared to A_R . Two different graphs are plotted for two values of the trapped electron density n_{el0} . The dotted plot shows a stronger dependence of reflection coefficient on the ion temperature in the presence of a large number of trapped electrons. Figure 4.4b shows that the effect of T_{el} on reflection coefficient is similar to that of T_i , but the effect of n_{el0} is opposite.

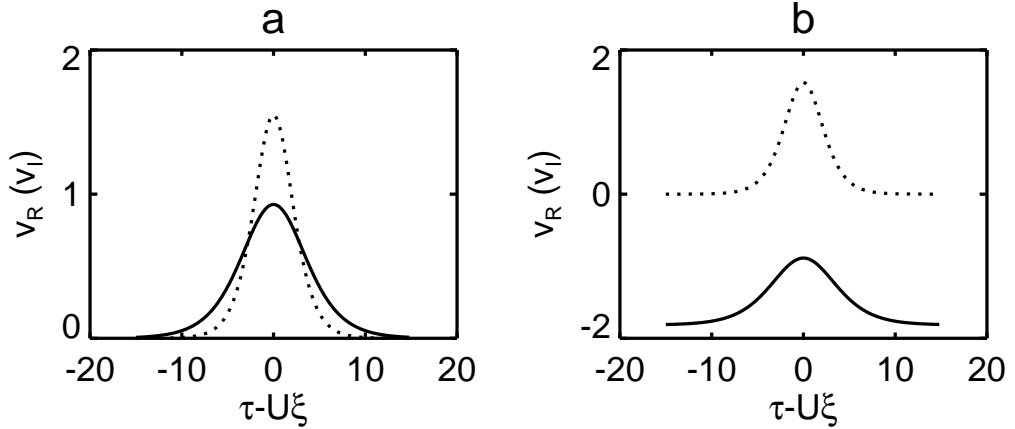


FIGURE 4.5: a) Perturbed velocity profiles for incident soliton (dotted) and reflected soliton (solid), without down-shift. b) Perturbed velocity for incident soliton (dotted) and reflected soliton (solid), with down-shift. Here, $T_i = 0.09$ eV, $n_{el0} = 0.04$ and all the other parameters are the same as used in Fig. 4.2.

The profiles of the incident and reflected solitons are shown in Fig. 4.5a. The incident soliton is the dotted one and is taller than the reflected soliton. The down-shift in the reflected soliton is not considered in Fig. 4.5a. The smaller amplitude of the reflected soliton in comparison with the amplitude of the incident soliton is a similar result to that obtained in earlier investigations [29, 31].

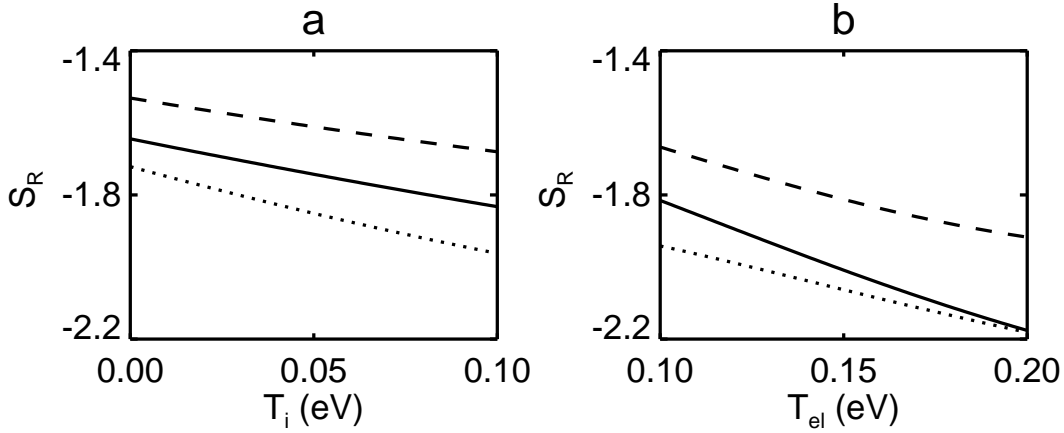


FIGURE 4.6: a) Dependence of soliton down-shift S_R , on ion temperature T_i , provided $T_{el} = 0.1$ eV. b) Dependence of soliton down-shift S_R , on trapped electron temperature T_{el} , provided $T_i = 0.09$ eV. The graphs are plotted for $n_{el0} = 0.04$, $\theta_R = 30^\circ$ (solid line), $n_{el0} = 0.06$, $\theta_R = 30^\circ$ (dotted line), and $n_{el0} = 0.04$, $\theta_R = 5^\circ$ (dashed line). All the other parameters are the same as used in Fig. 4.2

When the solitons get reflected in an inhomogeneous plasma with two-temperature electrons, we observe that the reflected solitons undergo a down-shift in their original line of propagation. Such down-shift could not be explored in earlier investigations on soliton reflection. Figure 4.5b shows the same soliton profiles as in Fig. 4.5a, but this time, the soliton down-shift is also taken into account. It is obvious from this figure that the solitons suffer a loss in amplitude as well as a shifting after the reflection. The physical reason for this down-shift could be the loss of energy of the soliton during reflection. Since the amplitude of the reflected soliton is smaller than the amplitude of the incident soliton and the energy is directly proportional to square of the amplitude, the reflected soliton carries less energy, i.e. $E_R < E_I$. Hence, a part of the energy is being utilized in shifting the soliton after its reflection. Moreover, these compressive solitons are the result of the compression of ions. The density-hill-type shape of the compressive solitons yields that the pressure at the upper side is more than the pressure at the lower side of the soliton. This will develop a pressure gradient force from the upper to the lower side. Hence, it is plausible that, during the reflection, this downward force brings the soliton down, i.e., the solitons are shifted after the reflection.

This down-shift could also be explained on the basis of the geometry of the problem under consideration. As mentioned earlier, the geometry of the present problem is such that there exists a density gradient and the incident solitons moving in $+xz$ direction witness a spatial decrease in density. This situation is reversed in the case of reflected solitons. When the reflected solitons propagate, they travel in the opposite direction, i.e., in the $-xz$ direction. This

means that the reflected solitons have to move uphill in order to propagate, resulting in the loss of energy which then causes the down-shift.

A background ion flow velocity could be another factor which plays a major role in giving rise to the down-shift in v_{1R} . It is clear from the geometry of the system that the ions have a background flow velocity (velocity components v_{0x} and v_{0z}) in the $+xz$ direction, i.e., along the direction of propagation of the incident solitons. When the soliton is reflected, it is slowed down due to the fact that it has to move upstream, i.e., against the flow of ions. As the reflected mKdV equation is a coupled equation, we can say that the down-shift S_R is actually a measure of the loss in the reflected soliton velocity as compared to the incident soliton velocity. This S_R then appears as an offset value in the solution of the reflected mKdV as seen in Eq. 4.32. A detailed scrutiny of the relation for S_R reveals that it originates from the combined effect of the background ion flow (v_{0x}, v_{0z}), the obliqueness, and the velocity shift U_R .

The down-shift that the soliton undergoes is also analyzed under the effect of ion and electron temperatures. The variation of soliton down-shift with the ion and electron temperatures is shown in Fig. 4.6a and 4.6b, respectively. Figure 4.6a shows that the soliton shift tends to increase with increasing ion temperature. Also, the increase of the soliton down-shift with a rise in the trapped electron temperature can be seen in Fig. 4.6b. The large down-shift of the soliton in the presence of higher temperature ions and electrons can be explained based on the speed of the incident soliton. Since the higher amplitude soliton propagates with larger speed, it is observed that the incident soliton propagates at a faster speed when the plasma has higher temperature ions and electrons. Under this situation, it is obvious that such fast-traveling soliton would reflect with a greater down-shift. Similar explanation may be given for the larger down-shift in the presence of a larger number of trapped electrons. Moreover, a comparison of dotted and solid graphs in Fig. 4.6 reveals that the down-shift is less when the soliton reflects at a smaller angle θ_R . It is also observed from these plots that, for a higher concentration of low-temperature electrons, the down-shift has a higher value.

Chapter 5

Effect of trapped electrons on soliton transmission during its oblique propagation in an inhomogeneous plasma

The soliton propagation and its oblique reflection in an inhomogeneous plasma has been studied in the previous chapters. It was observed that the reflected soliton carries lower energy in comparison with the incident soliton, revealing that there is a loss of energy in this mechanism. The difference of the energies, however, was responsible for the shift that is undergone by the soliton after its reflection.

Now in the present chapter, we investigate the complete problem of soliton propagation, its reflection and transmission in an inhomogeneous plasma under the effect of trapped electrons. Here additionally we derive a transmission-conservation law based on the energies of the incident soliton, reflected soliton and transmitted soliton. The effect of trapped electrons on the soliton's propagation, reflection and transmission is examined through the energy, amplitude and width of the solitons. Also, the effect of temperature and drift velocity of the ions is analyzed in this chapter.

For the sake of generality, we consider oblique propagation of the solitons and solve the problem by using well-known reductive perturbation technique for obtaining the relevant mKdV equations. These mKdV equations are coupled and then solved by exploring some new transformations.

5.1 Geometry of the problem

An inhomogeneous plasma is considered which has finite temperature ions and two-temperature non-isothermal electrons including trapped electrons. Due to the density gradient in the xz -direction, there is a background ion flow with velocity v_0 in the direction of decreasing density. In this plasma model,

the propagation, reflection and transmission of the waves is considered to be oblique, i.e. at an angle θ with the z -axis. The oscillations are assumed in the (x, z) plane and the incident wave makes an angle θ_I with the z -axis. After striking with the reflecting grid, it reflects and transmits, making angles θ_R and θ_T with the z -axis, respectively. The unit wave vector is taken as \hat{k} in the (x, z) plane. Hence $\hat{k} \cdot \vec{r} = x \sin \theta + z \cos \theta$, where θ could be θ_I , θ_R or θ_T . This is required to keep the obliqueness of the wave in our plasma model. For better understanding of the model, we have shown the directions of incident, reflected and transmitted solitons by I, R and T, respectively, in Fig. 5.1.

In view of the reflection and transmission of the solitons in the presence of a density gradient and trapped electrons, a semi-transparent reflector (metal grid) is considered in the plasma, which is partially transparent and the solitons not only get reflected but also get transmitted to the other side [43]. The physical mechanism behind this process is explained in section 2.8. The left hand side of the reflector is where the incident soliton propagates towards the right and after reflection from the mesh the soliton propagates towards the left (region A in Fig. 5.1). In this situation, a strong density gradient is produced surrounding the grid and the gradient in both the sides of the grid would be mirror image. However, the direction of density gradient in the bulk of the plasma depends on the plasma production methods. In the present case, this density gradient is assumed to be weak and is taken in the same direction in both the regions A and B. However, the region B is a bit different in the sense that it is slightly less inhomogeneous as compared to the region A. This means that the background ion flow velocity is lesser in the region B, i.e. $v_{0A} > v_{0B}$. In practice, we encounter this type of geometry in a double-plasma (DP) device, [22, 23] where unequally spaced filaments in the discharge chamber separated by a negatively biased grid may lead to the production of two separate inhomogeneous plasmas.

5.2 Mathematical formulation

5.2.1 Relevant mKdV equations

We start by writing the stretched coordinates for the incident, transmitted and reflected waves. In order to differentiate between the incident, reflected and transmitted waves, we use the subscripts I , R and T , respectively. Thus, the stretched coordinates for the incident case are:

$$\xi_I = \epsilon^{1/4} \left(\frac{x \sin \theta_I + z \cos \theta_I}{\lambda_{0I}} - t \right)$$

$$\tau_I = \epsilon^{3/4} (x \sin \theta_I + z \cos \theta_I).$$

Accordingly, the the stretched coordinates for the transmitted case are given as

$$\xi_T = \epsilon^{1/4} \left(\frac{x \sin \theta_T + z \cos \theta_T}{\lambda_{0T}} - t \right)$$

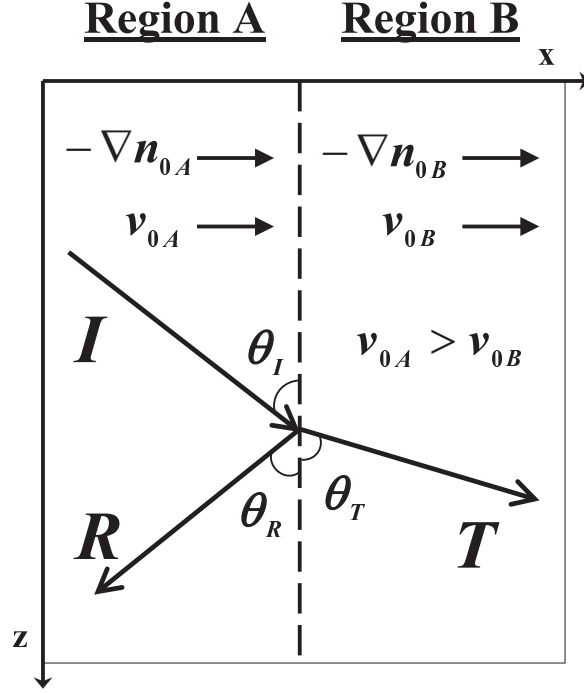


FIGURE 5.1: Diagram showing the geometry of the problem.

$$\tau_T = \epsilon^{3/4} (x \sin \theta_T + z \cos \theta_T),$$

and for the reflected case

$$\xi_R = \epsilon^{1/4} \left(-\frac{x \sin \theta_R + z \cos \theta_R}{\lambda_{0R}} - t \right)$$

$$\tau_R = -\epsilon^{3/4} (x \sin \theta_R + z \cos \theta_R).$$

Since the plasma is inhomogeneous in space, the unperturbed quantities are taken to be the functions of space coordinate $\tau_{I,R,T}$ only, which means

$$\frac{\partial n_0}{\partial \xi_{I,R,T}} = \frac{\partial n_{eI0}}{\partial \xi_{I,R,T}} = \frac{\partial n_{eH0}}{\partial \xi_{I,R,T}} = \frac{\partial v_{0x}}{\partial \xi_{I,R,T}} = \frac{\partial v_{0z}}{\partial \xi_{I,R,T}} = 0$$

This gives rise to various equations in zeroth, first and second order quantities. The zeroth order equations are the equilibrium equations that show the state of plasma before wave excitation. Based on the zeroth order equations, we arrive at the condition for the obliqueness of the incident and transmitted waves.

$$\theta_I = \theta_R = \cos^{-1} \left[\frac{v_{0zA}}{\sqrt{2 \frac{T_i}{T_{eff}} \ln n_0}} \right] \quad (5.1)$$

$$\theta_T = \cos^{-1} \left[\frac{v_{0zB}}{v_{0zA}} \cos \theta_I \right] \quad (5.2)$$

The above equations show that the obliqueness of the wave is decided by the intrinsic properties of the background plasma considered. Equations 5.1 and 5.2 also set an upper limit on the background ion flow velocity. Hence, the maximum possible value of v_{0z} is given as:

$$v_{0zmax} = \sqrt{2T_i \frac{n_{el0}T_{eh} + n_{eh0}T_{el}}{(n_{el0} + n_{eh0})T_{el}T_{eh}} \ln n_0} \quad (5.3)$$

However, the linear dispersion relations for the incident, reflected and transmitted waves are obtained as

$$\lambda_{0I} = v_{0xA} \sin \theta_I + v_{0zA} \cos \theta_I + \sqrt{(1 + 2\sigma)} \quad (5.4)$$

$$\lambda_{0R} = -v_{0xA} \sin \theta_R - v_{0zA} \cos \theta_R + \sqrt{(1 + 2\sigma)} \quad (5.5)$$

$$\lambda_{0T} = v_{0xB} \sin \theta_T + v_{0zB} \cos \theta_T + \sqrt{(1 + 2\sigma)} \quad (5.6)$$

The nonlinear analysis involves the higher order equations, and finally gives rise to the mKdV equations for all the three cases. A relevant mKdV equation for the incident wave is obtained as

$$\frac{\partial}{\partial \tau_I} v_{1I} + \alpha_I v_{1I}^{1/2} \frac{\partial}{\partial \xi_I} v_{1I} + \beta_I \frac{\partial^3}{\partial \xi_I^3} v_{1I} + \gamma_I v_{1I} \frac{\partial}{\partial \tau_I} n_0 = 0 \quad (5.7)$$

Here, v_{1I} is the first order velocity $\equiv v_{z1}$, and various coefficients are given by

$$\alpha_I = \frac{2N}{n_0 \lambda_{0I} \sqrt{[\cos \theta_I (\lambda_{0I} - v_{0I})] (\lambda_{0I}^2 + 1 + 2\sigma - v_{0I}^2)}}$$

$$\beta_I = \frac{1}{n_0 \lambda_{0I}^3 (\lambda_{0I}^2 + 1 + 2\sigma - v_{0I}^2)}$$

$$\gamma_I = \frac{v_{0I} (4\lambda_{0I}^2 + 4\sigma + 1) - \lambda_{0I} (3v_{0I}^2 + \lambda_{0I}^2 + 2\sigma)}{n_0 (\lambda_{0I}^2 + 1 + 2\sigma - v_{0I}^2) (v_{0I} - \lambda_{0I})}$$

where $v_{0I} = v_{0xA} \sin \theta_I + v_{0zA} \cos \theta_I$, and

$$N = n_{el0} b_l \left(\frac{T_{eff}}{T_{el}} \right)^{3/2} + n_{eh0} b_h \left(\frac{T_{eff}}{T_{eh}} \right)^{3/2}.$$

Similarly, the nonlinear analysis of the reflected wave gives rise to the following mKdV equation

$$\frac{\partial}{\partial \tau_R} v_{1R} + \alpha_R v_{1R}^{1/2} \frac{\partial}{\partial \xi_R} v_{1R} + \beta_R \frac{\partial^3}{\partial \xi_R^3} v_{1R} + \gamma_R v_{1R} \frac{\partial}{\partial \tau_R} n_0 = 0 \quad (5.8)$$

Here, various coefficients are given by

$$\alpha_R = \frac{2N}{n_0 \lambda_{0R} \sqrt{[\cos \theta_R (\lambda_{0R} - v_{0R})] (\lambda_{0R}^2 + 1 + 2\sigma - v_{0R}^2)}}$$

$$\beta_R = \frac{1}{n_0 \lambda_{0R}^3 (\lambda_{0R}^2 + 1 + 2\sigma - v_{0R}^2)}$$

$$\gamma_R = -\frac{v_{0R} (4\lambda_{0R}^2 + 4\sigma + 1) - \lambda_{0R} (3v_{0R}^2 + \lambda_{0R}^2 + 2\sigma)}{n_0 (\lambda_{0R}^2 + 1 + 2\sigma - v_{0R}^2) (\lambda_{0R} - v_{0R})}$$

together with $v_{0R} = -v_{0xA} \sin \theta_R - v_{0zA} \cos \theta_R$.

For transmission case the the mKdV equation looks like

$$\frac{\partial}{\partial \tau_T} v_{1T} + \alpha_T v_{1T}^{1/2} \frac{\partial}{\partial \xi_T} v_{1T} + \beta_T \frac{\partial^3}{\partial \xi_T^3} v_{1T} + \gamma_T v_{1T} \frac{\partial}{\partial \tau_T} n_0 = 0 \quad (5.9)$$

where,

$$\alpha_T = \frac{2N}{n_0 \lambda_{0T} \sqrt{[\cos \theta_T (\lambda_{0T} - v_{0T})] (\lambda_{0T}^2 + 1 + 2\sigma - v_{0T}^2)}}$$

$$\beta_T = \frac{1}{n_0 \lambda_{0T}^3 (\lambda_{0T}^2 + 1 + 2\sigma - v_{0T}^2)}$$

$$\gamma_T = \frac{v_{0T} (4\lambda_{0T}^2 + 4\sigma + 1) - \lambda_{0T} (3v_{0T}^2 + \lambda_{0T}^2 + 2\sigma)}{n_0 (\lambda_{0T}^2 + 1 + 2\sigma - v_{0T}^2) (v_{0T} - \lambda_{0T})}$$

with $v_{0T} = v_{0xB} \sin \theta_T + v_{0zB} \cos \theta_T$.

5.2.2 Solution of mKdV equations

The solution of the mKdV equations 5.7, 5.8 and 5.9 cannot be determined by ordinary methods due to the presence of variable coefficients. It is for this reason that we use a sine-cosine method [52, 54], suggested by Yan [48]. The same method has been used in earlier chapters too, so we skip the transformation details to avoid repetition and write down the solution as

$$v_I = A_I \operatorname{sech}^2 [W_I^{-1} (\tau_I - U_I \xi_I)] . \quad (5.10)$$

Here the peak amplitude and the width of the soliton are given by

$$A_I = \frac{15}{8\alpha_I b_I^{1/2} U_I}, \quad W_I = g_I^{-1} = \sqrt{16\beta_I U_I^3}.$$

The solution of the transmitted soliton is obtained by the same method and is given as

$$v_T = A_T \operatorname{sech}^2 [W_T^{-1} (\tau_T - U_T \xi_T)] , \quad (5.11)$$

together with the peak amplitude and width

$$A_T = \frac{15}{8\alpha_T b_T^{1/2} U_T}, \quad W_T = g_T^{-1} = \sqrt{16\beta_T U_T^3}.$$

In order to find the solution of the reflected mKdV equation, we first carry out coupling of the equations 5.7, 5.8 and 5.9. We do this by replacing v_{1R} in 5.8 by $v_{1I} + v_{1T} + v_{1R}$, which is the total ion fluid velocity. [28, 44, 55, 56] It is important to keep in mind that v_{1I} and v_{1T} are independent of τ_R and ξ_R . This way, the coupled equation becomes

$$\begin{aligned} \frac{\partial}{\partial \tau_R} v_{1R} + \alpha_R (v_{1I} + v_{1T} + v_{1R})^{1/2} \frac{\partial}{\partial \xi_R} v_{1R} + \beta_R \frac{\partial^3}{\partial \xi_R^3} v_{1R} \\ + \gamma_R (v_{1I} + v_{1T} + v_{1R}) \frac{\partial}{\partial \tau_R} n_0 = 0 \end{aligned} \quad (5.12)$$

In view of the reflection and transmission of the incident soliton only, we use $v_{1R} \ll v_{1I} + v_{1T}$ and also assume $v_{1T} \ll v_{1I}$. Thus, Eq. 5.12 takes the form

$$\begin{aligned} \frac{\partial}{\partial \tau_R} v_{1R} + \alpha_R P \frac{\partial}{\partial \xi_R} v_{1R} + \alpha_R \frac{P}{Q} v_{1R} \frac{\partial}{\partial \xi_R} v_{1R} + \beta_R \frac{\partial^3}{\partial \xi_R^3} v_{1R} + \gamma_R (v_{1I} + v_{1T}) \frac{\partial}{\partial \tau_R} n_0 \\ + \gamma_R v_{1R} \frac{\partial}{\partial \tau_R} n_0 = 0, \end{aligned}$$

$$\text{where, } P = \frac{2v_{1I} + v_{1T}}{2\sqrt{v_{1I}}} \quad \text{and} \quad Q = 2(v_{1I} + v_{1T}).$$

Now, we use a transformation $v_{1R} = b_R(\tau_R) \tilde{v}_R(\tau_R, \xi_R)$

$$\text{where } b_R(\tau_R) = \exp \left[- \int^{\tau_R} \gamma_R \frac{\partial n_0}{\partial \tau'_R} d\tau'_R \right].$$

With this, the aforementioned equation becomes

$$\begin{aligned} \frac{\partial}{\partial \tau_R} \tilde{v}_R + \alpha_R P \frac{\partial}{\partial \xi_R} \tilde{v}_R + \alpha_R b_R \frac{P}{Q} \tilde{v}_R \frac{\partial}{\partial \xi_R} \tilde{v}_R + \beta_R \frac{\partial^3}{\partial \xi_R^3} \tilde{v}_R \\ + \gamma_R \frac{(v_{1I} + v_{1T})}{b_R} \frac{\partial}{\partial \tau_R} n_0 = 0. \end{aligned}$$

We employ another transformation $\tilde{v}_R(\tau_R, \xi_R) = h_R(\tau_R) + v_R(\tau_R, \xi_R)$ along with

$$h_R(\tau_R) = \int^{\tau_R} -(v_{1I} + v_{1T}) \frac{\gamma_R}{b_R} \frac{\partial n_0}{\partial \tau'_R} d\tau'_R$$

in the above equation in order to get

$$\begin{aligned} \frac{\partial}{\partial \tau_R} v_R + \alpha_R P \frac{\partial}{\partial \xi_R} v_R + \alpha_R b_R \frac{P}{Q} h_R \frac{\partial}{\partial \xi_R} v_R + \alpha_R b_R \frac{P}{Q} v_R \frac{\partial}{\partial \xi_R} v_R \\ + \beta_R \frac{\partial^3}{\partial \xi_R^3} v_R = 0. \end{aligned} \quad (5.13)$$

The solution is then written as follows

$$v_R(\omega_R) = A_{0R} + A_{1R} \cos \omega_R + B_{1R} \sin \omega_R + A_{2R} \cos^2 \omega_R + B_{2R} \cos \omega_R \sin \omega_R \quad (5.14)$$

We set the values of A_{1R} , B_{1R} and B_{2R} as $A_{1R} = B_{1R} = B_{2R} = 0$. With this the coefficients of $\cos \omega_R$, $\cos^3 \omega_R$, $\cos^5 \omega_R$ and $\cos^7 \omega_R$ can be written as:

coefficient of $\cos \omega_R$:

$$-1 + U_R \alpha_R P + U_R \alpha_R b_R \frac{P}{Q} h_R + U_R \alpha_R b_R \frac{P}{Q} A_{0R} - 8\beta_R g_R^2 U_R^3 = 0$$

coefficient of $\cos^3 \omega_R$:

$$1 - U_R \alpha_R P - U_R \alpha_R b_R \frac{P}{Q} h_R - U_R \alpha_R b_R \frac{P}{Q} A_{0R} + U_R \alpha_R b_R \frac{P}{Q} A_{2R} + 20\beta_R g_R^2 U_R^3 = 0$$

coefficient of $\cos^5 \omega_R$:

$$U_R \alpha_R b_R \frac{P}{Q} A_{2R} - 12\beta_R g_R^2 U_R^3 = 0$$

Solving the above equations simultaneously by putting $A_{0R} = -A_{2R}$, we find the values of the unknown variables as

$$A_{0R} = -A_{2R} = \frac{3}{b_R} \left[\frac{1}{U_R \alpha_R} \frac{Q}{P} - Q - h_R b_R \right].$$

With these values, we obtain the following soliton solution

$$v_R = A_R \operatorname{sech}^2 [W_R^{-1}(\tau_R - U_R \xi_R)] \quad (5.15)$$

Here, A_R is the peak amplitude of the reflected soliton and is given as

$$A_R = \frac{3}{b_R} \left[\frac{4}{U_R \alpha_R \tilde{V}} - 2(v_{1I} + v_{1T}) - h_R b_R \right].$$

The width W_R of the reflected soliton is calculated by using the mKdV criterion, and is given by the value

$$W_R = \frac{5b_R}{2\alpha_I} \sqrt{\frac{\beta_I U_I}{b_I}} \left[\frac{4}{U_R \alpha_R \tilde{V}} - 2(v_{1I} + v_{1T}) - h_R b_R \right]^{-1},$$

$$\text{where, } \tilde{V} = \frac{2v_{1I} + v_{1T}}{\sqrt{v_{1I}(v_{1I} + v_{1T})}}.$$

5.3 Soliton reflection-transmission conservation law

In the previous chapter, it was observed that the energies of the incident and reflected solitons are not the same, and the reflected soliton carries lower energy. The reflected soliton was found to undergo a shift and this shift was explained based on the energy difference between the incident and reflected solitons. However, in the present case of complete phenomenon of soliton propagation, its reflection and transmission, such a shift has been compensated

with the transmission of the soliton. Hence, we take the total energy carried by the reflected and transmitted solitons to be equal to the energy of the incident soliton, in order to derive a transmission-reflection conservation law. In the present plasma of weak inhomogeneity, we consider the zeroth order quantities to vary slowly with space, in view of large density gradient scale length. The energy carried by the incident soliton can be obtained by the following integral

$$E_I = \int_{-\infty}^{\infty} v_I^2(\tau_I, \xi_I) d(\xi_I - U_I \tau_I).$$

We put the values of v_I from Eq. 5.10 in the above integral and obtain

$$E_I = A_I^2 \int_{-\infty}^{\infty} \left[\operatorname{sech}^2 \left(\frac{\xi_I - U_I \tau_I}{W_I} \right) \right]^2 d(\xi_I - U_I \tau_I) \quad (5.16)$$

Thus, the value of E_I is evaluated to be

$$E_I = \frac{4}{3} A_I^2 W_I \quad (5.17)$$

In view of the similar profiles of the transmitted and reflected solitons, their energies are written as

$$E_T = \frac{4}{3} A_T^2 W_T \quad \text{and} \quad E_R = \frac{4}{3} A_R^2 W_R.$$

The conservation of energy requires $E_I = E_T + E_R$, which leads to the following relation

$$\frac{4}{3} A_I^2 W_I = \frac{4}{3} A_T^2 W_T + \frac{4}{3} A_R^2 W_R \quad (5.18)$$

According to the mKdV criterion (Eq. 2.3), the product of the amplitude and width of a soliton remains constant.

$$A_I W_I = A_T W_T = A_R W_R \quad (5.19)$$

Based on the work of other investigators [12], we can use this mKdV criterion for the present case and eliminate the widths W_I , W_R and W_T from Eq. 5.18, with the help of Eq. 5.19. This leads to the relation

$$A_I = A_T + A_R \quad (5.20)$$

Finally, we achieve the following transmission-reflection conservation law

$$\left[8\alpha_I b_I^{1/2} U_I \right]^{-1} = \left[8\alpha_T b_T^{1/2} U_T \right]^{-1} + \left[\frac{4}{5U_R \alpha_R \tilde{V} b_R} - \frac{2(v_{1I} + v_{1T})}{5b_R} - \frac{h_R}{5} \right] \quad (5.21)$$

As the reflection coefficient RC and transmission coefficient TC are defined in terms of solitons' amplitudes, so we can also express the above transmission-reflection conservation law in the form of RC and TC . Thus taking $TC = A_T/A_I$ and $RC = A_R/A_I$ we can write Eq. 5.20 as

$$1 = TC + RC \quad (5.22)$$

Unlike other investigators, we calculate the values of U_R and U_T using the concept of energy conservation (Eq. 5.21). With the use of Eq. 5.20 we find the value of U_R , which is given as

$$U_R = \frac{12}{\alpha_R \tilde{V} [6(v_{1I} + v_{1T}) + 3h_R b_R + b_R(A_I - A_T)]},$$

and for obtaining the value of U_T we make use of Eq. 5.19, and find

$$U_T = \frac{\beta_I \alpha_T^2 b_T}{\beta_T \alpha_I^2 b_I} U_I.$$

This way, we make sure that the properties of the reflected and transmitted solitons are connected with the incident soliton and all the solitons satisfy the required soliton transmission-reflection conservation law.

5.4 Results and discussion

At this point, we have the expressions for the various soliton properties including the soliton energy. The effect of different plasma parameters will be studied on the soliton properties in this section. To start with, all three profiles of the incident, reflected and transmitted solitons are shown in Fig. 5.2. Here, and in all the forthcoming plots, the solid line graphs represent the incident solitons, and the dashed and dotted line graphs show the transmitted and reflected solitons, respectively. Figure 5.3 shows the effect of ion temperature T_i on the soliton properties, viz. amplitudes and widths, respectively, for fixed obliqueness. It has been observed in section 3.2 that the ion temperature influences the wave by increasing its phase velocity. This results in taller and narrower solitons, i.e. solitons with bigger amplitude and smaller widths. This is quite clearly observed in Fig. 5.3.

The presence of two-temperature non-isothermal/trapped electrons also has a very significant effect on the soliton characteristics. It has already been established in the previous chapters that the trapped electrons alter the soliton structure prominently, even if they are present in a very small amount. In order to examine the contribution of these electrons to soliton propagation, reflection and transmission, we have plotted Fig. 5.4, which shows the effect of trapped electron temperature on the amplitudes and widths of the solitons. It is clear from this figure that the solitons propagate, reflect and transmit with larger amplitudes and widths in the presence of trapped electrons with higher temperatures.

The main focus of this chapter is on the energy of the solitons; hence, we analyze in detail the energy carried by the incident, reflected and transmitted solitons. Figure 5.5 shows how higher temperatures of ions and trapped electrons give rise to more energetic solitons. As the energy of the soliton depends on the amplitude and width of the soliton, we can expect that more energetic solitons are emerged in the presence of higher values of T_i ; this can be seen in

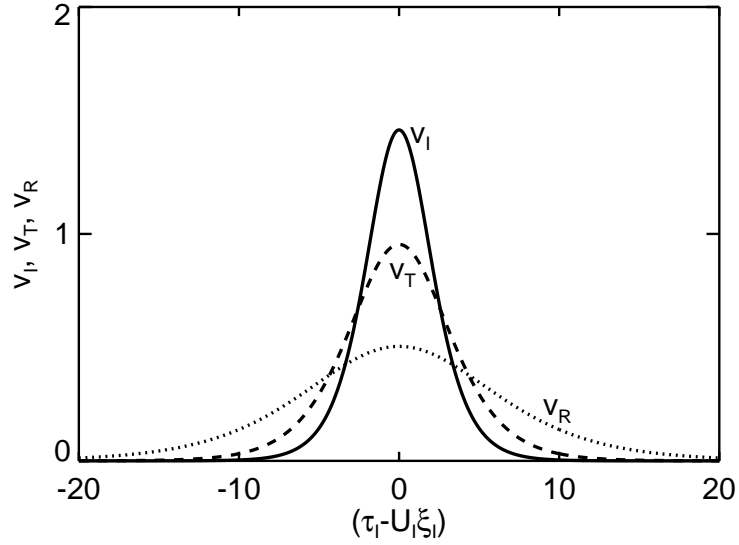


FIGURE 5.2: Incident (solid line), transmitted (dashed line) and reflected (dotted line) soliton profiles. Here, $T_i = 0.09$ eV, $T_{el} = 0.1$ eV, $T_{eh} = 5$ eV, $U_I = 1.1$, $v_{0zA} = 0.025$, $v_{0B} = 0.02$, $n_{el0} = 0.05$, $n_{0A} = 0.9$ and $n_{0B} = 0.85$.

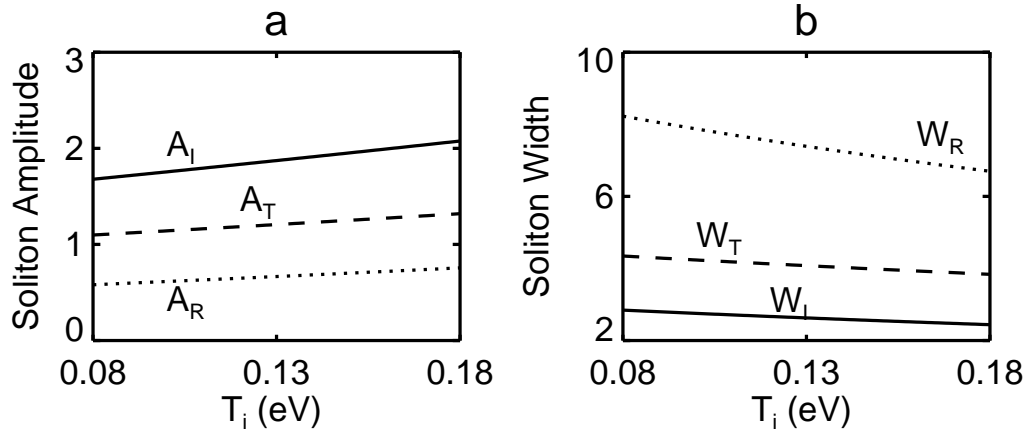


FIGURE 5.3: Effect of ion temperature T_i on peak amplitudes and widths of the incident, reflected and transmitted solitons for $\theta_I = 20^\circ$. All the other parameters are the same as used in Fig. 5.2.

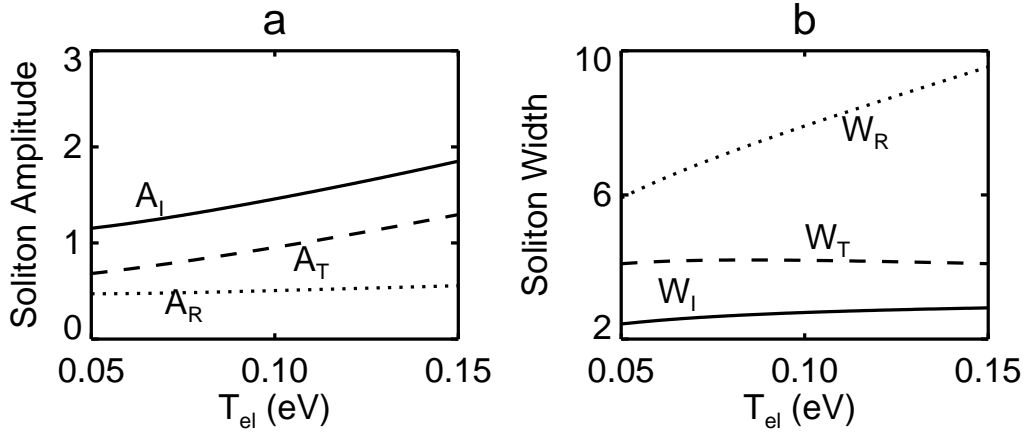


FIGURE 5.4: Effect of trapped electron temperature T_{el} on peak amplitudes and widths of the incident, reflected and transmitted solitons for T_i . All the other parameters are the same as used in Fig. 5.2.

Fig. 5.5a. A comparison between Figs. 5.5a and 5.5b reveals that the effect of ion temperature T_i on the soliton energy is weaker in comparison with that of the temperature T_{el} . The temperature of trapped electrons has a more significant effect on the energy, as compared to that of ions because increase in T_{el} gives rise to taller and at the same time wider solitons, and the energy being a product of both amplitude and width, increases significantly. This can be seen from Fig. 5.5b.

The strength of reflection and transmission of the solitons is expressed in terms of ratios of the amplitudes and are given as the reflection coefficient RC ($= A_R/A_I$) and the transmission coefficient TC ($= A_T/A_I$). These coefficients are calculated as percentages and are plotted with respect to T_i and T_{el} in Fig. 5.6. We observe that T_i has only a slight effect on the reflection and transmission coefficients. The strength of reflection increases and the strength of transmission decreases slightly with the increase in T_i , as shown in Fig. 5.6a. In Fig. 5.6b we see an opposite behavior when T_{el} is increased. According to the energy conservation law given in Eq. 5.22, if RC increases, TC decreases simultaneously. This is quite obvious from Fig. 5.6.

A similar type of behavior of the incident, reflected and transmitted solitons with the concentration n_{el0} of the trapped electrons is noticed in Figs. 5.7 and 5.8. Since the electrons are trapped by the wave potential, it is obvious that the energy exchange occurs between the electrons and the wave. In the present case of ion-acoustic waves and hence the solitons, where the thermal speed of the trapped electrons and the wave velocity of the ion-acoustic wave are of the same order, it is plausible that the wave takes energy from the electrons and hence the solitons evolve with higher amplitudes and greater speeds. The energy of the solitons being proportional to the square of the

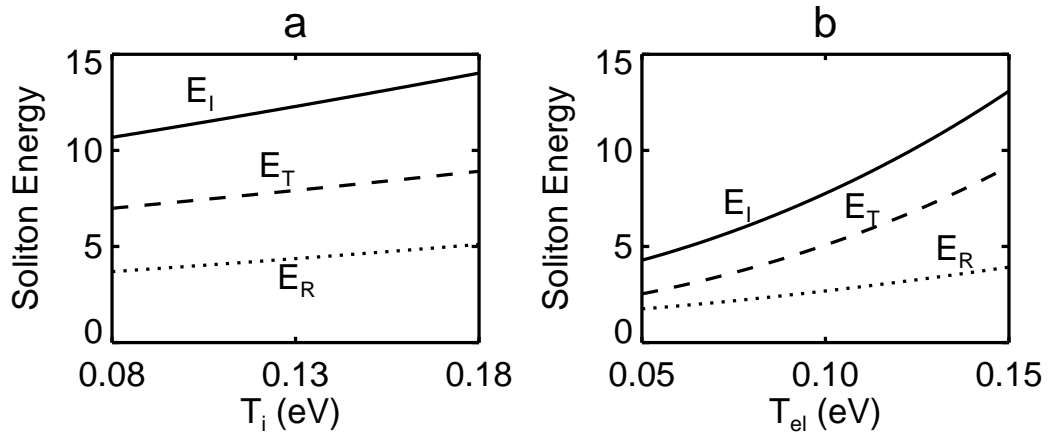


FIGURE 5.5: Effect of a) ion temperature T_i and b) trapped electron temperature T_{el} on the energies of incident, reflected and transmitted solitons corresponding to Fig. 5.3 and 5.4.

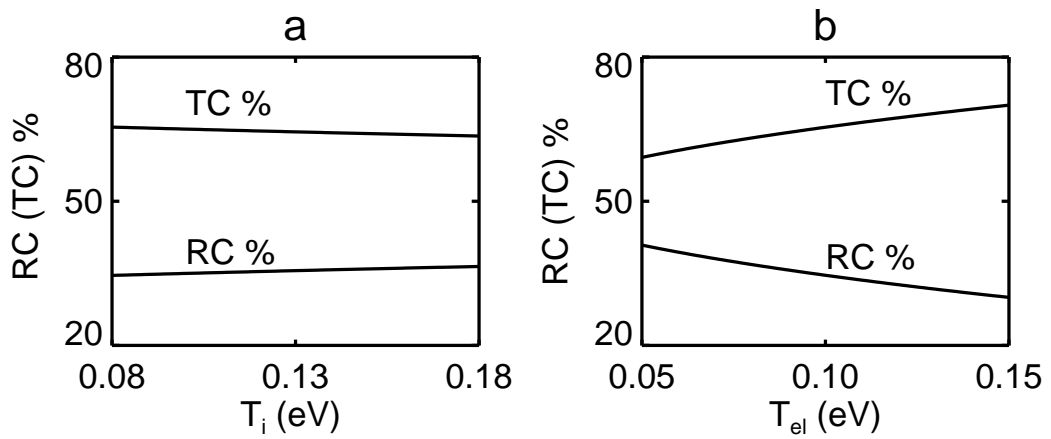


FIGURE 5.6: Effect of a) ion temperature T_i and b) trapped electron temperature T_{el} on the reflection and transmission coefficients RC and TC of the solitons corresponding to Fig. 5.3 and 5.4.

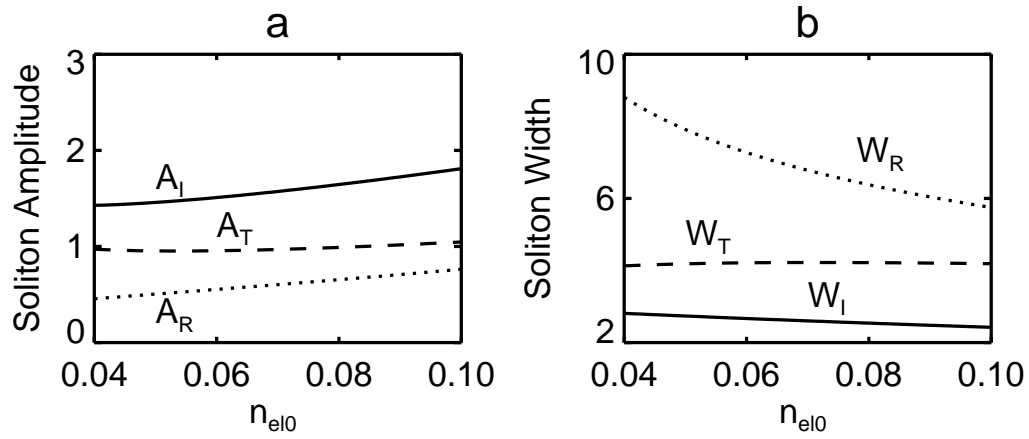


FIGURE 5.7: Effect of trapped electron density n_{el0} on peak amplitudes and widths of the incident, reflected and transmitted solitons, when the other parameters are the same as in Fig. 5.2.

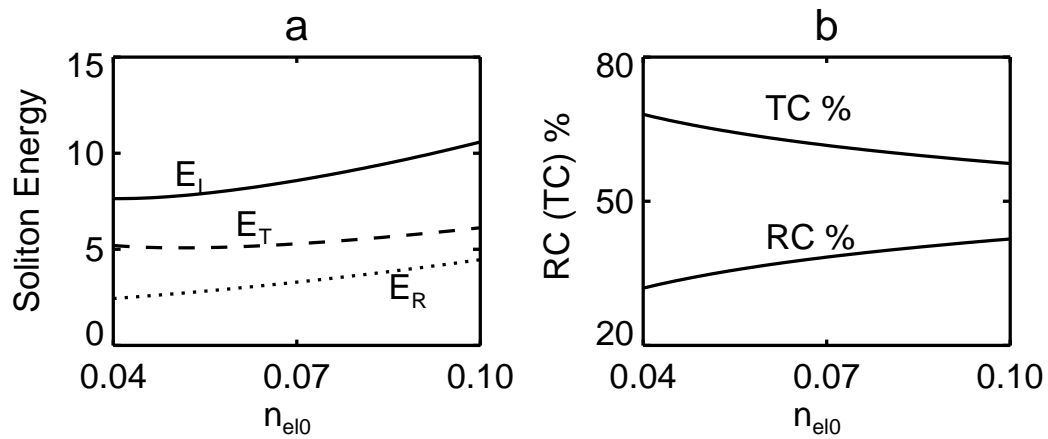


FIGURE 5.8: Effect of trapped electron density n_{el0} on a) energies of incident, reflected and transmitted solitons and b) on reflection and transmission coefficients RC and TC . All the other parameters are the same as in Fig. 5.7.

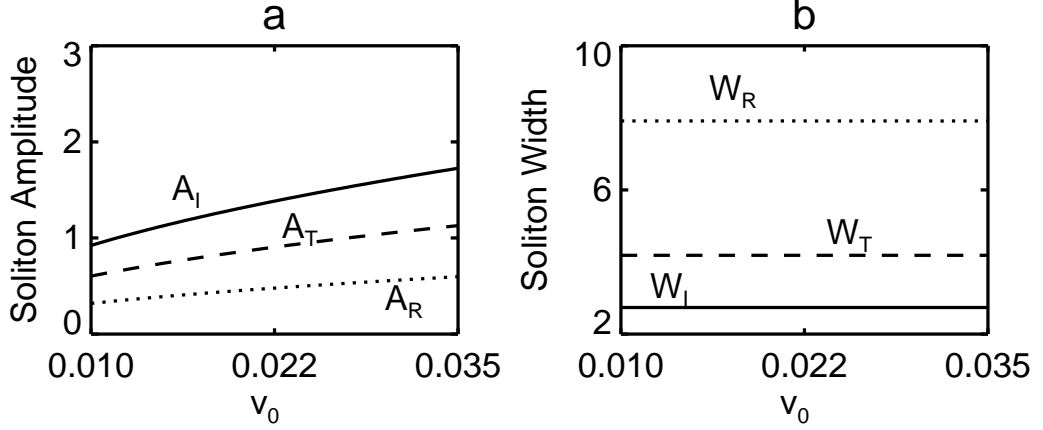


FIGURE 5.9: Effect of background ion-flow velocity v_0 on peak amplitudes and widths of the incident, reflected and transmitted solitons, when the other parameters are the same as in Fig. 5.2.

amplitude (Eq. 5.17) also gets higher in the presence of the trapped electrons, as seen in Fig. 5.8a. As has been understood by other researchers, [44, 46, 53] the incident soliton carrying higher amplitude gets reflected strongly and hence, in the present case also we obtain larger reflection coefficient in the presence of more trapped electrons. This increase in RC and a consequent decrease in TC is portrayed in Fig. 5.8b. Hence, it is further confirmed that the trapped electrons drastically modify the soliton profiles in the plasma; their small fraction yields significant changes in the soliton amplitude, width and energy as is evident from Figs. 5.7 and 5.8.

In the present case of an inhomogeneous plasma, the background ion flow velocity v_0 is actually a measure of the density gradient. It is to be noted here that for the sake of simplicity we have taken $v_{0z} \equiv v_0$. In order to see the effect of inhomogeneity (density gradient) on different properties of the solitons, we try to investigate the effect of the background ion flow velocity v_0 on the soliton propagation. In this context, it is observed from Fig. 5.9 that higher values of ion flow velocity v_0 result in bigger solitons; consequently they are more energetic. The increase in incident, reflected and transmitted soliton energies (E_I , E_R and E_T) with an increase in ion flow velocity v_0 is shown in Fig. 5.10a. Consistent to the earlier Figs. 5.3, 5.4, 5.7 and 5.9, the amplitudes A_I , A_T and A_R here also follow the trend $A_I > A_T > A_R$. However, the opposite behavior of the widths W_I , W_T and W_R , i.e. the trend $W_R > W_T > W_I$, is obvious from the same figures. As is evident from Fig. 5.9, T_i has an implication of enhancing the amplitudes of incident, reflected and transmitted solitons at the same rate. Due to this reason we do not see any change in the reflection and transmission coefficients in Fig. 5.10b.

From the trend of incident, reflected and transmitted solitons' amplitudes,

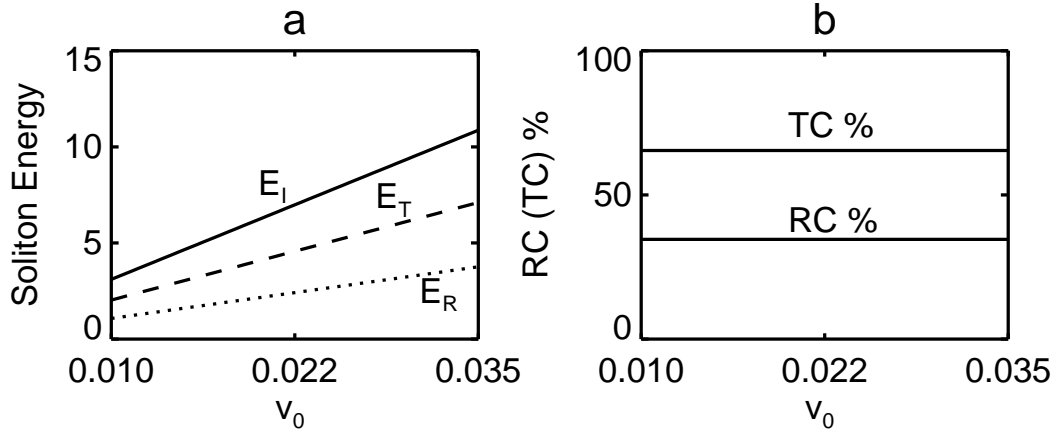


FIGURE 5.10: Effect of background ion-flow v_0 on a) energies of incident, reflected and transmitted solitons and b) on reflection and transmission coefficients RC and TC corresponding to Fig. 5.9.

it is obtained that in the present plasma with trapped electrons, the transmission of the solitons is more significant than their reflection for the plasma conditions under study.

It is very interesting to note that the angle (θ_T) of the transmission of the solitons shows stronger dependence on the density of trapped electrons, and the temperature of ions. This is a new observation and has not so far been explored in other investigations. It is clear from Fig. 5.11a that the angle θ_T gets larger with the increasing density n_{el0} and the temperature T_i . It means the solitons get transmitted at a larger angle when trapped electrons in a greater number are present in the plasma, and the plasma has ions of higher temperature. Since the amplitude A_I of the incident soliton is raised for the higher density n_{el0} and temperature T_i , it can be inferred that the incident solitons with higher amplitudes and hence, with larger energies, get transmitted at larger angles. It can also be said that the obliqueness of the transmitted solitons is in direct proportion to the size of the incident solitons. On the other hand, Fig. 5.11b shows the maximum possible value of the ion drift velocity for realizing the solitons' reflection and transmission. Clearly, the reflection and transmission of the solitons is possible for higher values of ion drift, if the trapped electrons in greater number are present in the plasma and/or the plasma has ions of higher temperature.

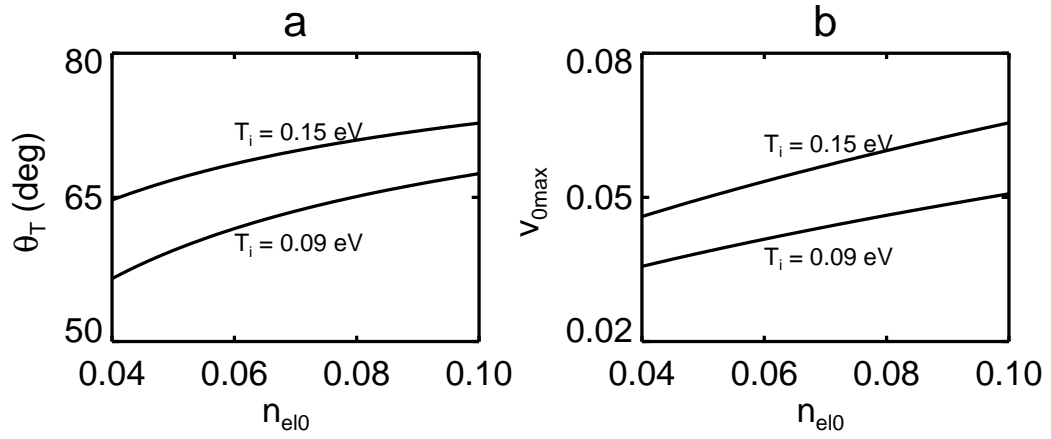


FIGURE 5.11: Dependence of v_{0max} on the density of trapped electrons for two different values of ion temperature, when $T_{el} = 0.1$ eV.

Chapter 6

Excitation of linear and nonlinear ion-acoustic waves in a Double-Plasma (DP) device

In laboratory, solitons are most commonly excited in DP devices. DP devices have proven to be quite useful for studying solitons, since the first experimental observations of solitons, carried out by Ikezi *et al.* [20] in a DP device. A DP device, as evident from its name, consists of two separate plasmas in a single vacuum vessel. It is so constructed that a metallic vacuum chamber is divided into two electrically separate chambers viz., the source chamber and the target chamber. These are physically separated by a metal wire grid kept at floating/negative potential. The plasma can be generated in the two chambers by heating filaments. The separation grid being at floating potential resists the electron communication from the source chamber to the target chamber.

6.1 FLIPS as a Double-Plasma device

For our experimental studies on linear and nonlinear ion-acoustic waves, we carried out our work on a flexible linear device called FLIPS, which is an acronym for *Flexibles Plasmaexperiment Stuttgart*, at the Institut für Plasmaforschung, Stuttgart. FLIPS, as evident from its name is flexible so that we can vary the length of the vacuum chamber according to experimental requirements, and that axial magnetic fields of different structures can be superimposed.

The apparatus consists of a big cylindrical vacuum chamber made of steel, with a maximum length of 2.106 m and an outer diameter of about 0.52 m. The casing is made up of 5 mm thick wall of non-magnetic steel. A schematic diagram of the device is shown in Fig. 6.1a.

Magnetic confinement is an important aspect of laboratory plasma experiments. In FLIPS, a large number of permanent magnets were arranged in “full-line cusp” configuration in order to shield the plasma from the wall. This

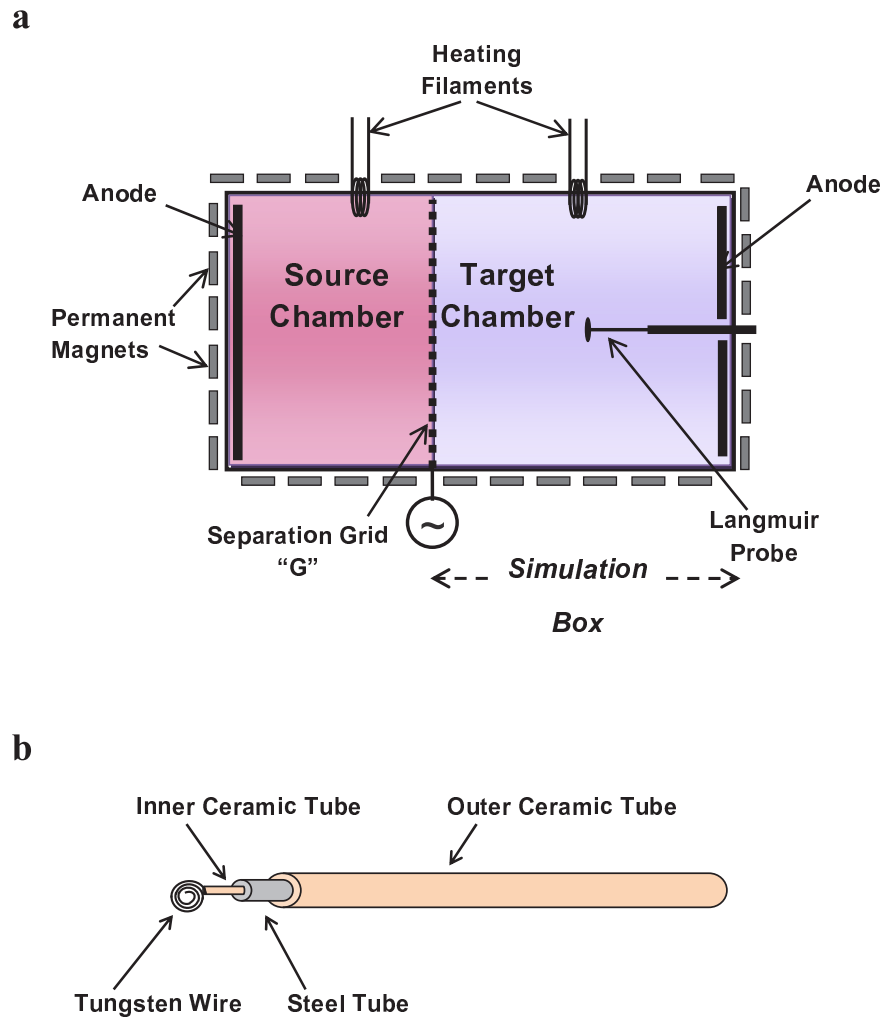


FIGURE 6.1: a) Schematic diagram of the Double-Plasma (DP) device used for soliton generation. The region marked as Simulation Box is the region to be simulated. b) Schematic diagram of the Langmuir probe used for diagnostic measurements.

means that the magnetic field is restricted to the vicinity of the walls of the vacuum chamber and the charged particles moving towards the walls are reflected due to the magnetic mirror effect. The “full-line cusp” configuration provides an efficient plasma confinement and also helps in achieving a higher plasma density in the device by decreasing the losses [57]. Due to this configuration, the magnetic field does not penetrate more than a few centimeters in the vacuum vessel and the bulk plasma remains unmagnetized. This way the magnetic field does not affect the process of excitation of the waves.

6.2 Experimental setup

Argon plasmas were created in both the source and the target chambers by heating tungsten filaments and accelerating the emitted electrons to the respective anodes. The filament in the source chamber was connected to 75 V and 500 mA and in the target chamber the filament was connected to 50 V and 300 mA. A simple schematic diagram of the DP device used in our experiment is given in Fig. 6.1a. Argon gas was fed in the chamber at a pressure of about 20 – 30 mPa. The number density in the target chamber was measured and found around $1 \times 10^{16} \text{ m}^{-3}$, the electron temperature T_e was about 1 – 2 eV and the ion temperature T_i was less than 0.05 eV. This means that the ratio $T_e/T_i > 20$. This is an important feature of a DP device that reduces the damping of waves by lowering the Landau damping.

Langmuir probes is the earliest and still the most widely used diagnostic tool used to measure plasma parameters. Langmuir probes work on the principle that external objects immersed in the plasma tend to form a space charge sheath around them. The I-V characteristics are plotted by biasing the probe, and the electron saturation current is then measured. The electron saturation current being proportional to the electron density can detect the density fluctuations. We take the electron instead of the ion saturation current, because the signal is stronger despite the electrostatic influence of the grid modulations. In order to detect the waves, a Langmuir probe was built and inserted in the target chamber of the device. A simple schematic diagram of the probe used in the experiment is shown in Fig. 6.1b. The probe was constructed using a tungsten wire whose tip was twisted in a spiral to make a plane probe and to have a bigger surface area. The wire was insulated by a ceramic tube which was inside a steel tube for the purpose of shielding from the electric field. This steel tube was again insulated by another ceramic tube. The probe was so mounted that it could move axially, and density fluctuations can be measured at different positions from the grid G .

6.3 Excitation of linear ion-acoustic waves in FLIPS

Just like acoustic waves in a neutral gas, ion-acoustic waves are the longitudinal oscillations of ions in a plasma. Acoustic waves in neutral gas cannot occur in the absence of collisions, however, ions in a plasma can transfer the oscillations through an electric field. Ion-acoustic waves are low frequency electrostatic waves which can occur in unmagnetized plasma or parallel to a background magnetic field. The dispersion relation of an ion-acoustic wave is given as

$$\frac{\omega}{k} = \sqrt{\frac{\gamma_e T_e + \gamma_i T_i}{m_i}} = C_i \quad (6.1)$$

Here C_i is the speed, ω is the frequency, and k is the wave number of the ion-acoustic wave. Also γ_e and γ_i are the adiabatic coefficients for electrons and ions, respectively. The value of γ in the form of degrees of freedom N is given as.

$$\gamma = \frac{2 + N}{N}$$

In case of one dimensional compressions the value of γ_i is taken to be 3. Electrons being very fast, equalize their temperature so that we can consider them as isothermal and take $\gamma_e = 1$. In laboratory plasmas, the ion temperature is usually very low as compared to the electron temperature i.e. $T_e \gg T_i$. Hence, the ion-acoustic speed can simply be written as

$$C_i = \sqrt{\frac{T_e}{m_i}} \quad (6.2)$$

We excite linear ion-acoustic waves in our DP device “FLIPS” by applying a sinusoidal voltage signal on the separation grid G , which was capacitively coupled with a frequency generator. In this way, the separation grid was modulated around the floating potential. The two anodes were kept at ground potential. The peak-to-peak amplitude of the applied sinusoidal signal was 1.2 V. The heating filament of the source chamber was given a voltage of 75 V and a current of 500 mA. The heating filament of the target chamber was given a voltage of 50 V and 300 mA. The argon gas was kept at a pressure of 37 mPa. The modulations applied to the grid, produce initial density perturbations in the target chamber of FLIPS, which then evolve into ion-acoustic waves. These ion-acoustic waves were then detected by the Langmuir probe. The Langmuir probe could move axially and hence we could measure the wavelength of the waves for different applied frequencies.

In Fig. 6.2, we have plotted the graph between frequency and wave number using the data obtained from the Langmuir probe measurements. The dashed line shows the linear dispersion relation given by Eq. 6.1. We observe here that for low frequencies, the experimental result is in good agreement with the theory. For high frequencies i.e, shorter wavelengths we see a deviation from

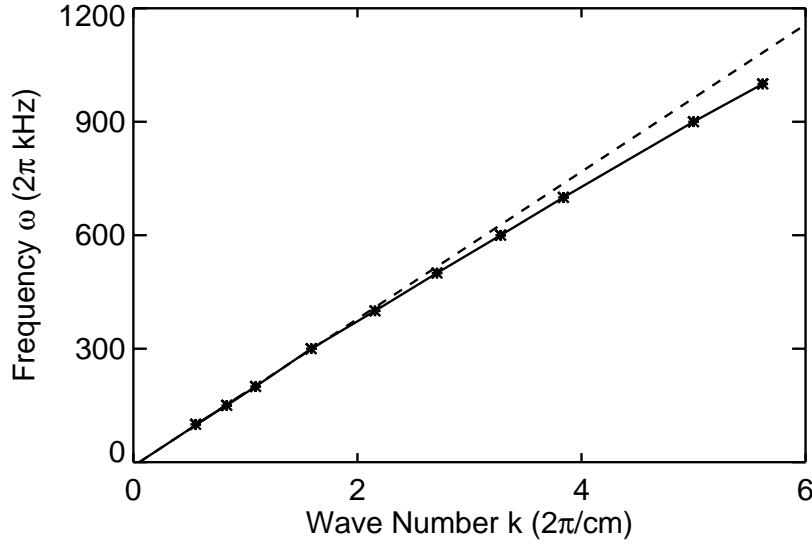


FIGURE 6.2: Graph of the measured dispersion relation for a linear ion-acoustic wave. The dashed line represents the theoretical linear dispersion relation.

the linearity. This reveals the fact that ion-acoustic waves of constant speed are only exhibited at lower frequencies, i.e. at frequencies not higher than the ion plasma frequency ω_{pi} . The ion plasma frequency is given as

$$\omega_{pi} = \sqrt{\frac{e^2 n_i}{\epsilon_0 m_i}} \quad (6.3)$$

Also it is a well established fact that the dispersion relation of the ion-acoustic waves, converges to a constant frequency, for large values of the wave number k . The slope of the linear part of the graph gives the ion-acoustic velocity. The electron temperature can also be obtained from the value of the ion-acoustic velocity using Eq. 6.2.

In Fig. 6.2, the anodes were kept grounded but the effect of increasing anode voltages was also seen by launching ion-acoustic waves at different anode voltages. Figure 6.3 shows the dispersion relations plotted for four different anode voltages. It can be seen that the ion-acoustic velocity increases with the increase in the anode voltage. The reason being that the increase in the anode voltage results in an enhancement in the electron temperature. As the ion-acoustic speed is directly proportional to the electron temperature (Eq. 6.2), higher anode voltages result in higher ion-acoustic speeds.

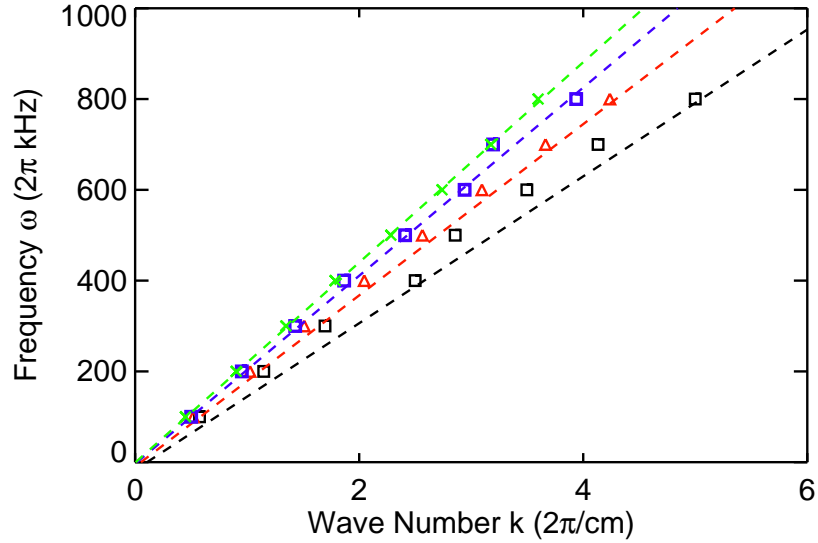


FIGURE 6.3: Dispersion relations for different anode voltages. Black represents 0 V, red 10 V, blue 30 V and green represents 50 V anode voltage, respectively.

6.4 Excitation of solitons in FLIPS

In general, solitons can be excited in a DP device either by applying voltage signals in the form of pulses or continuous waves to the source chamber with respect to the target chamber. One possibility is to apply the voltage signals between the anodes of the two chambers (DP mode) and another one is to apply the signal between the separation grid and the anodes (grid mode) [58]. We use a technique very similar to the latter and modulate the separating grid at a frequency near the ion plasma frequency. This way the ions coming from the source chamber are modulated while entering into the target chamber. The present method is quite similar to the method where a grid is inserted in a single multidipole device, except for the fact that we can now vary the flow of ions from the target chamber to the source chamber by adjusting the plasma potentials of the two chambers.

In FLIPS, the solitons were excited in the target chamber of the DP device by applying bursts of sinusoidal signals of 2 MHz frequency at a repetition rate of 2 kHz on the separation grid. The peak-to-peak amplitude and the duration of the signal were 6 V and 25 μs , respectively. The two anodes were kept grounded. The plasma was at a pressure of 26 mPa and the number density was of the order of 10^{16} m^{-3} . The filament in the source chamber was at 75 V and 500 mA and in the target chamber it was at 50 V and 100 mA, respectively. Diagnostic measurements were again carried out by the Langmuir probe that measures the fluctuations in the electron saturation current, which then gives the fluctuations in the electron density. As the plasma is quasi-

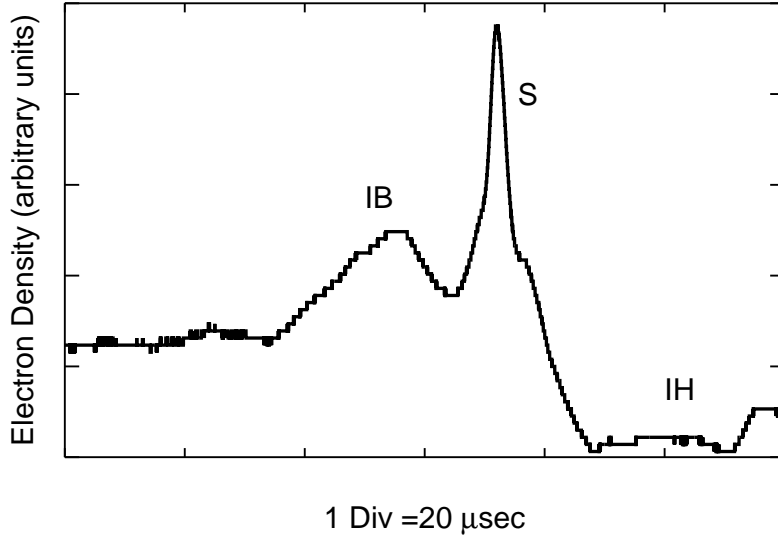


FIGURE 6.4: Electron saturation current measured by the Langmuir probe placed at a distance of 15 cm from the grid. Here, IB, S and IH refer to ion burst, soliton and ion hole, respectively.

neutral, i.e. $n_e \simeq n_i$, the fluctuations in the electron density represent the fluctuations in the ion density. The Langmuir probe was mounted axially in the target chamber so that it moves perpendicular to the grid. This enabled us to measure the signals at various distances from the grid. The signal was amplified twice.

The electron saturation current detected by the Langmuir probe placed at a distance of 15 cm from the grid is shown in Fig. 6.4, where the biggest signal is referred to as the soliton and is marked as S. This structure is followed by a depression of ions, which we name as an ion hole (IH). This ion hole is generated from the trailing edge of the signal. Apart from that, a small hump or burst is also spotted ahead of the soliton. We call this an ion burst (IB), due to the fact that it is made up of a burst of ions.

Figure 6.5 shows the signals detected at 5, 8, 10, 15 and 20 cm from the grid. Here the duration of the applied signal was $250 \mu\text{s}$. For this reason the ion hole IH being emitted from the trailing edge of the signal forms a bit farther away from the soliton and is not seen in the figure. At 5 cm, the soliton S is seen propagating towards the left along with the ion burst IB ahead of it. This ion burst consists of fast ions that result when the modulation is applied on the separation grid. As the fast ions are quite energetic, some of them take part in the soliton formation. The burst then continues to move on, precedes the soliton and is seen ahead of the soliton.

The fact that this ion burst is faster than the soliton and moves ahead of it is further clarified in Fig. 6.6, where the distance-time graphs for S, IB and the

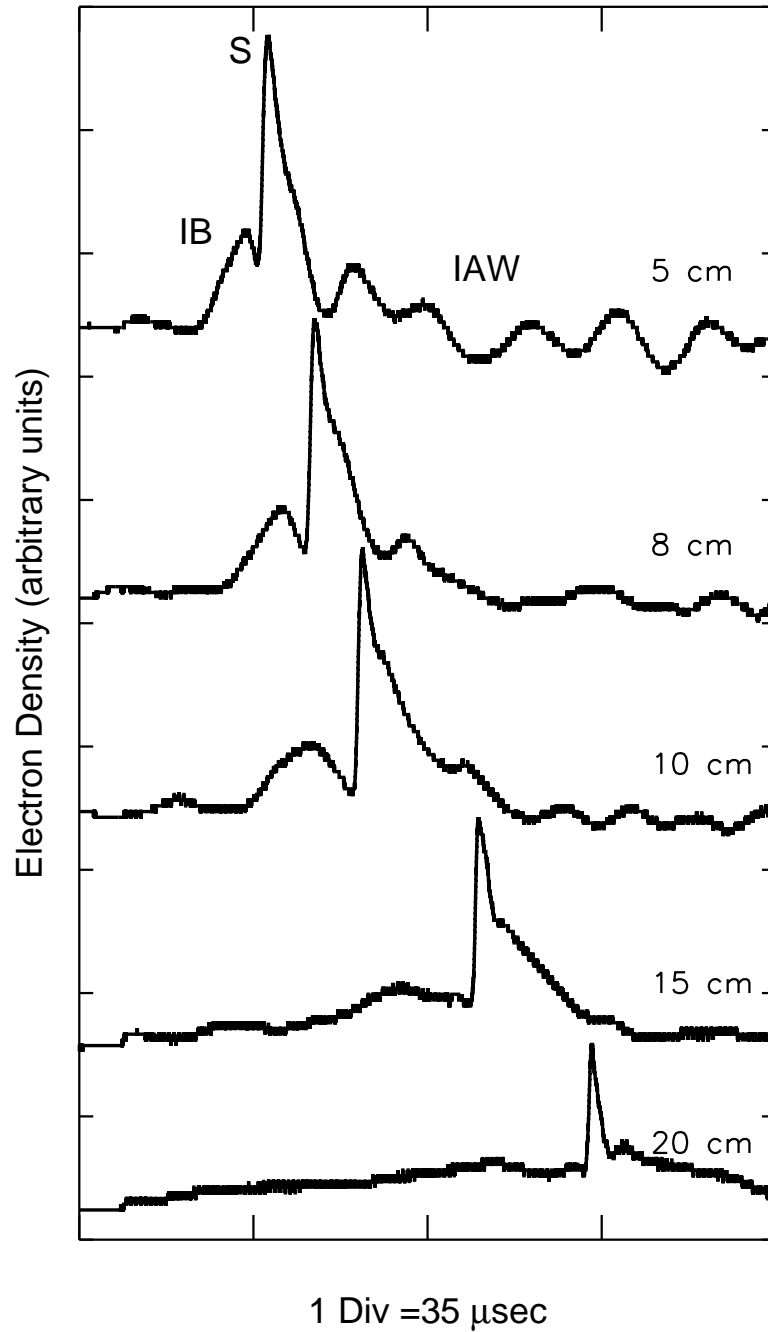


FIGURE 6.5: Langmuir probe measurements, showing the soliton propagating toward the left at various distances from the excitation grid.

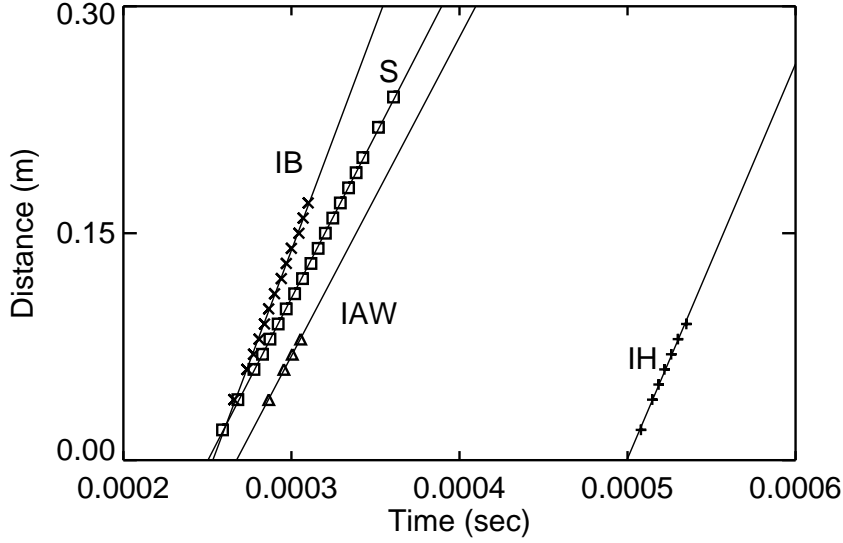


FIGURE 6.6: Trajectories of the various signals. Here, IB refers to ion burst, S to soliton, IAW to ion-acoustic wave and IH to ion hole. The velocities are found to be $V_{IB} = 1.407$, $V_S = 1.023$, $V_{IAW} = 1$ and $V_{IH} = 1.24$.

ion-acoustic wave IAW are plotted and the relative velocities are calculated by following the trajectories of the observed signals. Since the speed of the ion burst remains the same and hence is not accelerated (Fig. 6.6), it is evident that the ion burst is not reflected from the compressive soliton. The velocities of the various signals are calculated in terms of Mach numbers. The normalized velocities of the soliton, ion burst, ion-acoustic wave and ion hole are referred to as V_S , V_{IB} , V_{IAW} and V_{IH} respectively. At later positions, viz. 10, 15 and 20 cm, the ion burst moves away from the soliton and eventually disperses. On the other side, at the initial stages, the ion-acoustic wave IAW ($V_{IAW} = 1$) can also be seen following the soliton. This ion-acoustic wave, as expected, suffers damping and is barely visible after a few centimeters of distance. Thus, the only prominent structure is the soliton.

The relative amplitude of the soliton in Figs. 6.5 and 6.6 is found to be $\delta n/n = 4.5\%$. The velocity of the soliton was calculated by following its trajectory and the Mach number was obtained as $V_S = 1.023$. According to the KdV criterion, the velocity of the soliton should be $1 + \delta n/3n$ (Eq. 2.1). This way, the theoretical KdV velocity of the soliton comes out to be 1.015, which is in agreement with our experimental value. This shows that these solitons are KdV type solitons.

6.5 Effect of excitation signal parameters on soliton properties: Experimental results

In this section, we will summarize some results that were obtained during the experimental studies on the solitons in FLIPS. In particular, the effects of amplitude, frequency and duration of the applied signal are investigated on the soliton propagation characteristics.

6.5.1 Effect of signal amplitude

The effect of increasing grid-modulation signal amplitude on the soliton is shown in Fig. 6.7. We observe that the amplitude of the soliton and the ion hole is quite small for smaller peak-to-peak amplitude of the applied signal. As the applied signal amplitude increases, the soliton gets bigger, as does the ion hole. We also see an increase in the size of the ion burst, as the fast ions of which the ion burst consists, depends on the amplitude of the excitation signal [24, 59, 60, 61].

The relative amplitude $\delta n/n$ of the soliton is calculated, and is plotted against the peak-to-peak amplitude of the excitation signal, in Fig. 6.8. The time-of-flight is also plotted in Fig. 6.8, which is the time at which the soliton is formed at a certain location. Here, we notice that the soliton amplitude increases, reaches a maximum and then becomes constant for higher signal amplitudes. The time-of-flight of the soliton behaves contrarily. This indicated that for higher values of excitation signal amplitudes bigger and faster solitons are evolved, but after 8 V the amplitude does not increase any more. This result is in agreement with the results of Yi *et al.* [25].

6.5.2 Effect of signal duration

In order to see the effect of signal duration on the soliton characteristics, soliton profiles at different time durations of the signals are plotted in Fig. 6.9. The most evident effect of the signal duration is the formation of the ion hole further apart from the soliton. The reason for this, already explained in the previous chapter, is that the ion hole is generated from the trailing edge of the excitation signal. Hence, the longer the excitation signal, the farther the ion hole is generated.

The relative amplitude of the soliton and the time-of-flight is plotted against the duration of the excitation signal and is shown in Fig. 6.10. In this figure, we see that the amplitude of the soliton first increases, reaches a maximum and then becomes almost constant. As the soliton is formed due to the beginning edge of the signal duration and the trailing edge does not play any role in the soliton evolution, the soliton should not be affected from the signal duration. It was seen that for short signal durations the ion hole and the soliton are very close to each other and this affects the properties of the soliton. This might be the reason for smaller solitons in the case of shorter signal duration. For

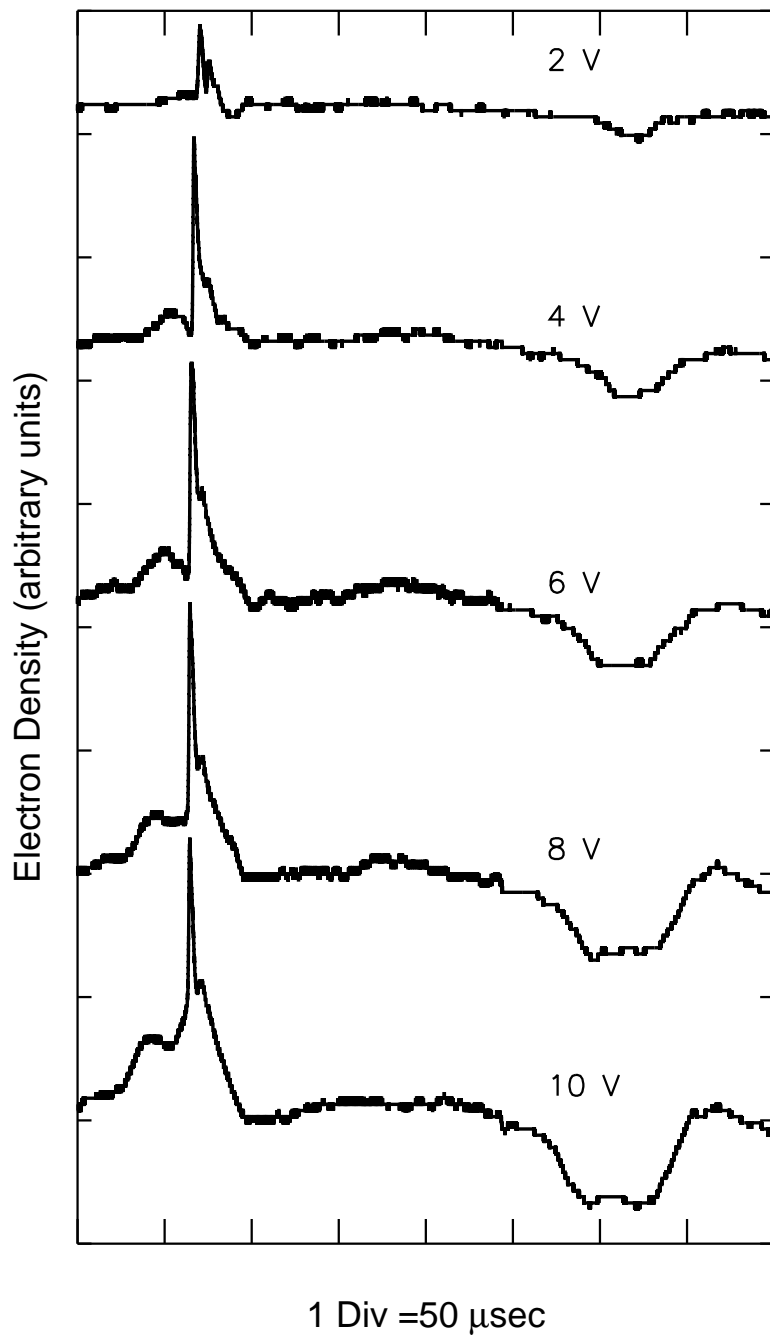


FIGURE 6.7: Soliton profiles at different peak-to-peak amplitudes of the applied signal.

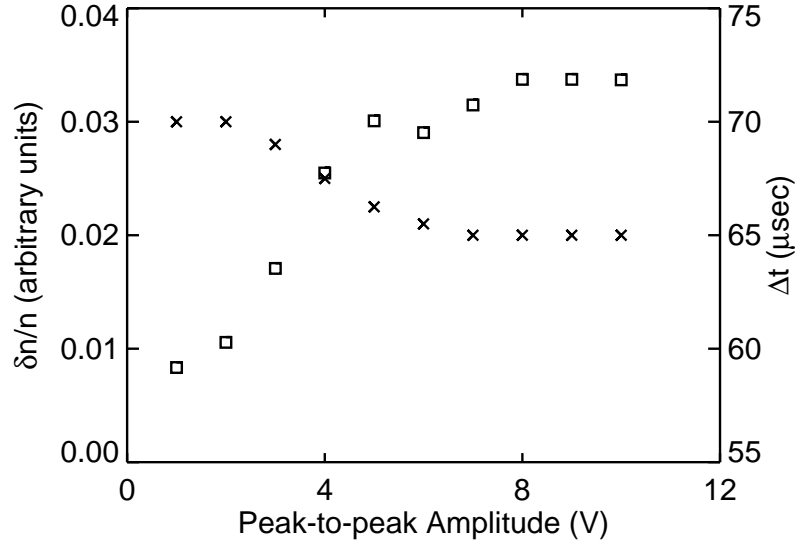


FIGURE 6.8: Dependence of soliton amplitude (\square) and time-of-flight (\times) on peak-to-peak amplitude of the signal applied to the separation grid G .

longer signal durations we see that the soliton amplitude becomes independent of the signal duration. This implies the fact that after the separation of the ion hole from the soliton, the amplitude and time-of-flight of the soliton become independent of the signal duration.

6.5.3 Effect of signal frequency

The solitons profiles for different frequencies of the applied signal can be seen in Fig. 6.11. It is observed that for low excitation frequencies (below 1 MHz) a single soliton is not observed, rather a few other structures also appear along with the soliton. This is in accordance with the fact that the number of solitons depend on the width of the excitation signal [20]. It might be another soliton or an ion-acoustic wave but cannot be clearly distinguished due to the noisy signal. As the applied frequency is increased, we again see the single prominent soliton and the accompanying structure are either not evolved or are dominated by the bigger soliton.

The effect of enhancement in the frequency of the grid-modulation signal on the relative amplitude of the soliton and the time-of-flight is seen in Fig. 6.12. Here, we observe an increase in the amplitude and afterwards it attains saturation for higher applied frequencies.

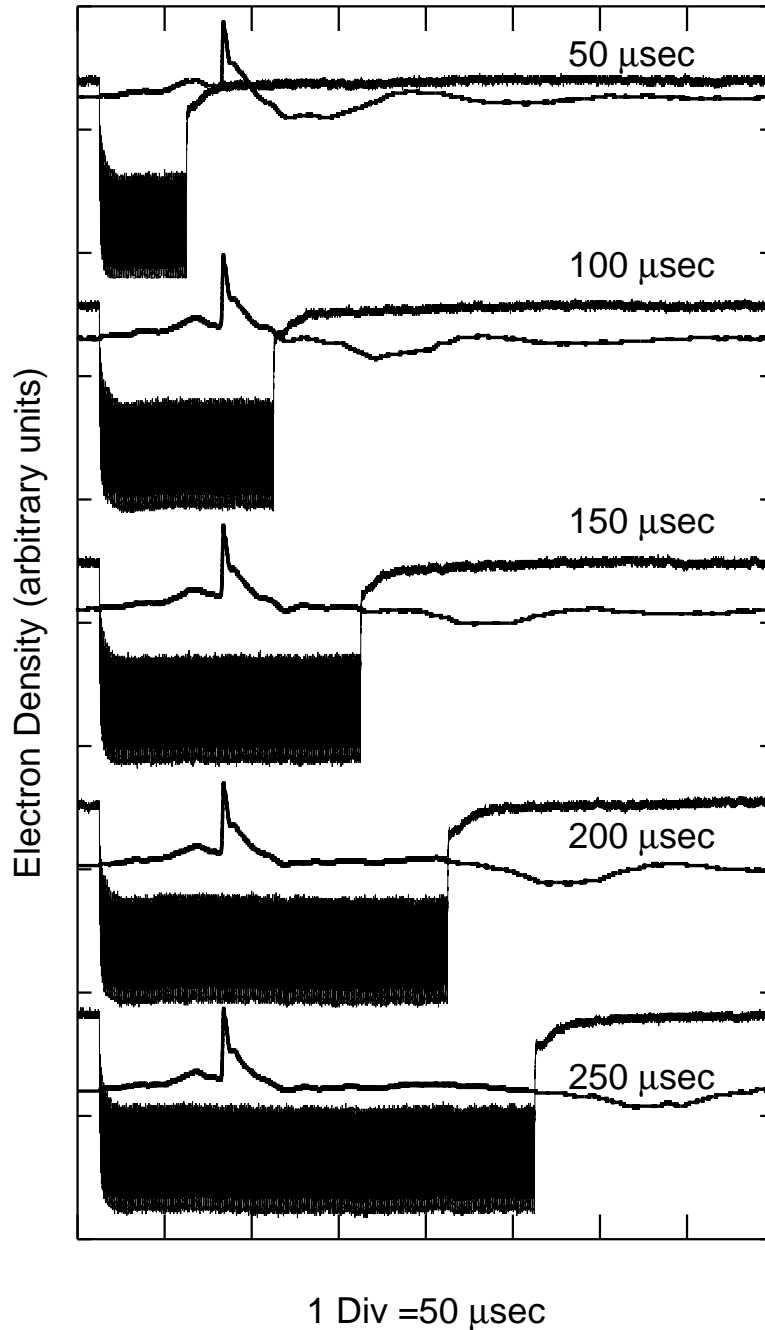


FIGURE 6.9: Soliton profiles at different applied signal durations.

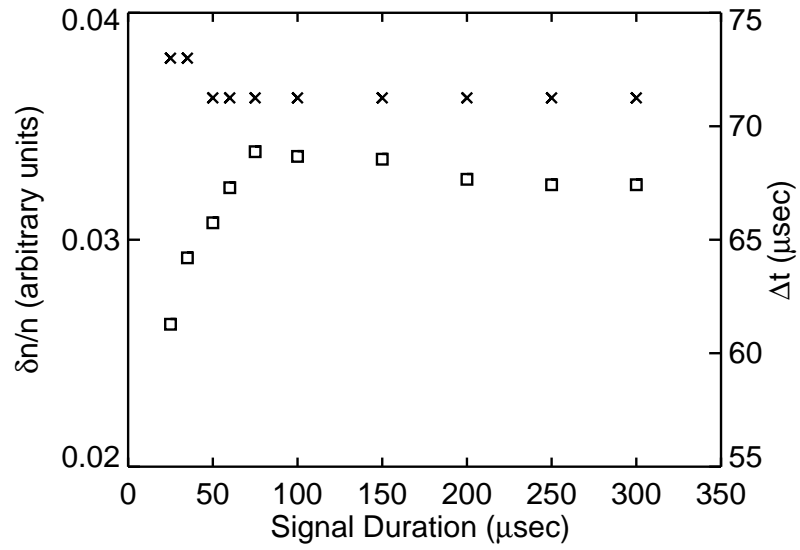


FIGURE 6.10: Dependence of soliton amplitude (\square) and time-of-flight (\times) on the duration of the signal applied to the separation grid G .

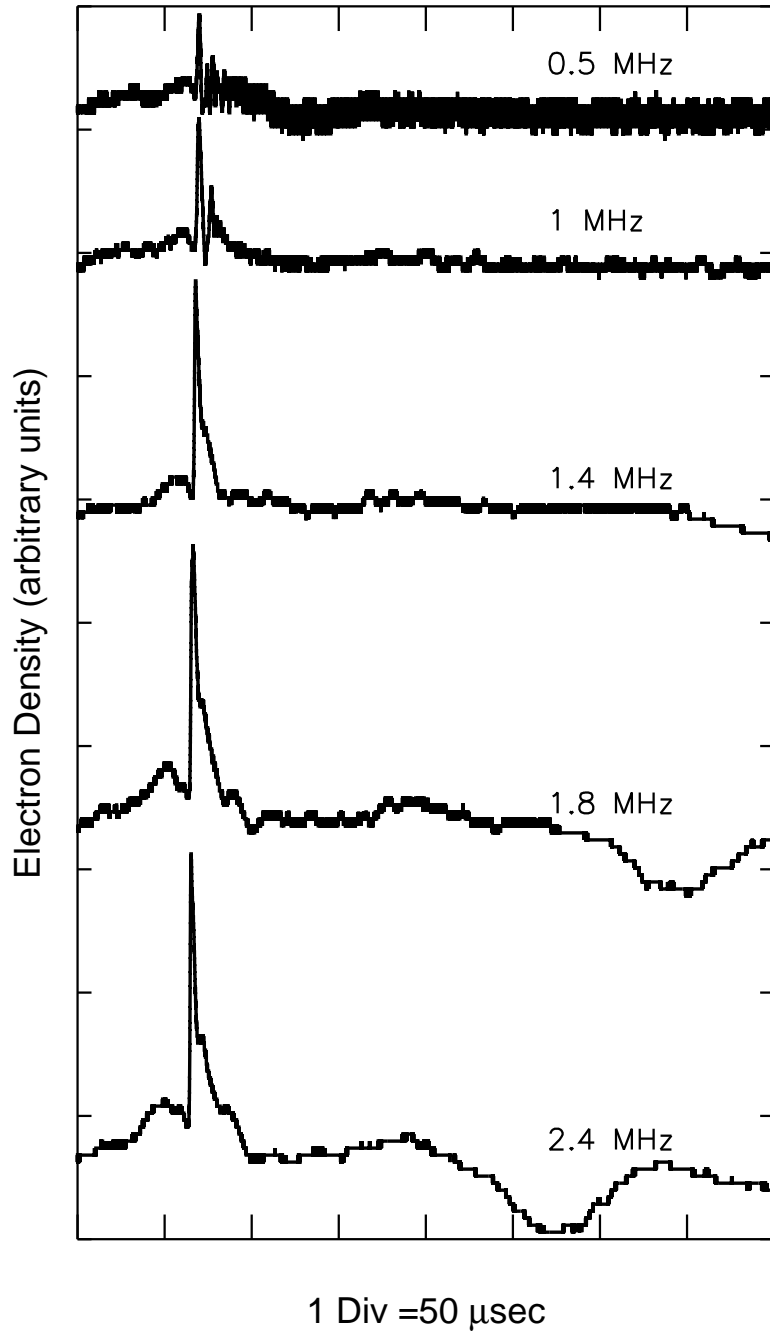


FIGURE 6.11: Soliton profiles at different applied signal frequencies.

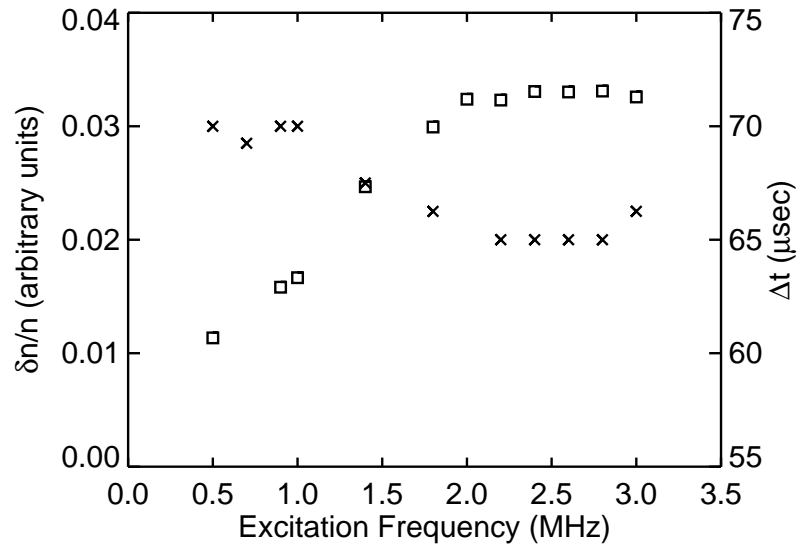


FIGURE 6.12: Dependence of soliton amplitude (\square) and time-of-flight (\times) on the frequency of the signal applied to the separation grid G .

Chapter 7

Particle-In-Cell simulations

Apart from the experimental and theoretical investigations of the solitons, there has been an increasing interest in simulating the evolution of solitons from grids [62, 63, 64]. Hence, the experimental results obtained in the previous chapter are simulated in this chapter to get a detailed insight into the mechanisms involved in the excitation and propagation of solitons in a DP device. The difference between simulated and real plasma lies in the representation of charges, the fields and the space time in which the phenomenon occurs. Among the most successful models for computer simulations of plasma are particle models.

7.1 Particle simulation models

In particle simulation models, we follow the motion of a large number of charged particles in their self-consistent electric and magnetic fields. As the number of particles in a real plasma is much higher than a typical computer can actually follow, a computer particle is made to represent a lot of real particles. Hence, in a particle simulation, each charged particle is a homogeneous collection of a large number of real plasma particles, called a *super-particle*. It is always multiple charged and has a greater mass, but the charge to mass ratio is the same as for real particles.

Using super-particles is not enough and it is still too time consuming to calculate the inter particle forces directly. Hence, in the early 1960s a mathematical mesh or grid across the length of the plasma was introduced. In order to make a computational mesh, the physical volume is divided into cells by lines which run parallel to the boundaries of the simulation box. The intersection of these lines define a set of points called mesh points or grid points. A computational mesh is shown in Fig. 7.1a. Introducing a grid has two major purposes. Firstly, it helps speeding up the calculation, and secondly the inter particle forces at distances less than a grid cell are smoothed away. The grid gives particles a finite size, reducing short range forces, because otherwise these would be artificially enhanced by the small number of simulation particles.

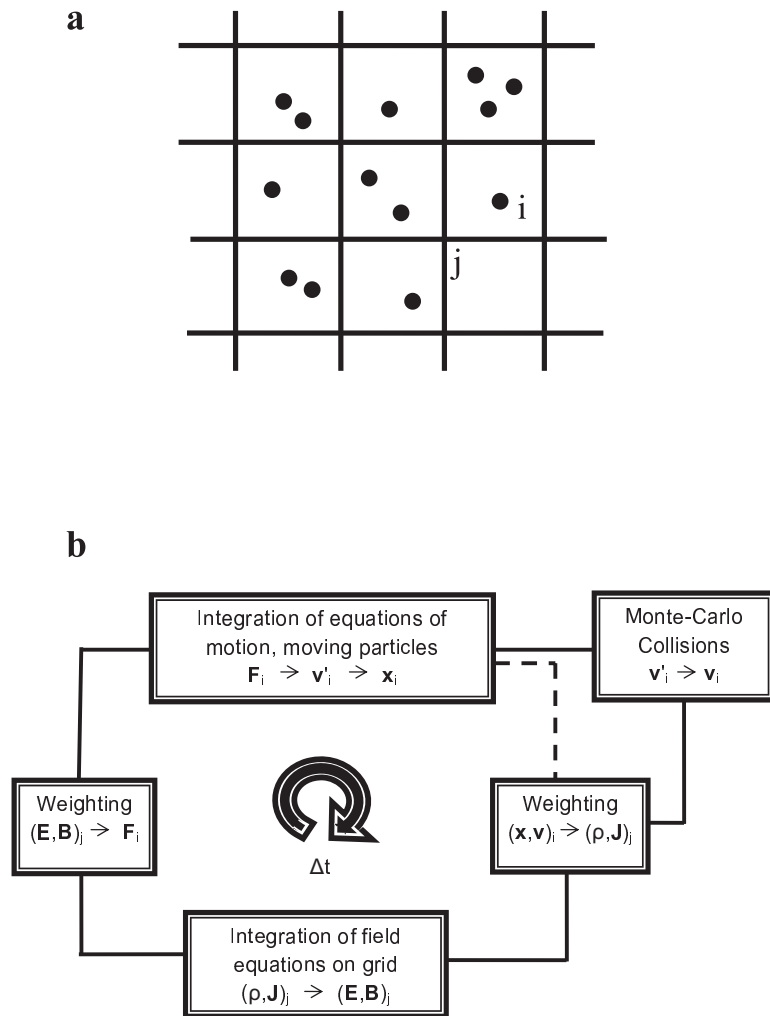


FIGURE 7.1: a) The spatial grid/mesh for the particle simulation models, where the dots are the super-particles, and i and j represent the positions of the particles and grid points, respectively. b) The computational cycle of the PIC simulation.

7.2 The Particle-In-Cell simulation technique

Particle-In-Cell (PIC) simulations have widely been used as a computational technique to understand and predict the plasma behavior [65]. In the Particle-In-Cell simulation technique, a spatial grid is introduced on which the charge and current densities are accumulated using an interpolation scheme. The field equations are solved on this grid. The forces acting on the particles are obtained by interpolating the fields back to the particles.

7.2.1 The computational cycle

The computational cycle of the PIC simulation is shown in Fig. 7.1b. The index i is used to denote quantities evaluated for the particles, and j is used for those evaluated at the grid points. This is also pointed out in Fig. 7.1a. The computational cycle consists of four steps (excluding the Monte-Carlo collision). In the first step, the acceleration is computed and the particle positions and velocities are updated. In the second step, the charge density ρ is evaluated at the grid points using the charge of each particle and current particle position; this is called *weighting*. It can be noted that ρ has the index j pointing to the fact that the charge density is calculated on the grid. The third step integrates the Poisson's equation to obtain the electric potential, and computes the electric field \mathbf{E} on the grid via a finite difference scheme. In the last step, the force on each particle is computed from the electric field at neighboring grid points.

As PIC codes can also include collisions between charged particles and neutral atoms using Monte-Carlo methods, an extra step in the computational cycle is also introduced (Fig. 7.1b). The most straight forward way is to test all the particles in the simulation for each time step. However, this consumes a lot of time; so another technique called the null collision method is used. In this method, a particle is picked out and the relative probability of a collision is tested against a random number to determine if a collision really occurs. For these simulations, only electron-neutral and ion-neutral collisions are considered.

7.2.2 Scaling

Scaling is important because it relates the simulations with the real plasma world. The values assigned to parameters like grid spacing, the time step and the super-particle density are very important because they give the speed and the accuracy of the simulation. Before carrying out PIC simulation of the plasma a few things must be taken into consideration in order to avoid unphysical results.

1. The number of super-particles in the simulation N_p should be much greater than the number of grid cells n_g , i.e. $N_p \gg n_g$. This is to

ensure that each grid cell always contains several particles on the average during the simulation. If the number of particles is too small, the simulation will be noisy.

2. The size of the grid cell Δx should be of the order of the Debye length $\lambda_D = \sqrt{\epsilon_0 T_e / n_0 e^2}$, i.e. $\Delta x \leq \lambda_D$. The Debye length is the maximum distance over which the Coulomb forces of individual particles are important. If the grid spacing is smaller we will not be able to reduce the short-range particle interactions, which are unimportant for the overall behavior of the plasma. However, if the spacing is made larger than Debye length, then important electric field gradients can be ignored, as the fields are only determined at the grid points. Also, as the grid cells determine the particle size, bigger grid cells will lead to unphysical results.
3. The time step Δt should be smaller than the period of plasma oscillations $f_{pe}^{-1} = 2\pi \sqrt{\epsilon_0 m_i / n_0 e^2}$, i.e. $\Delta t < f_{pe}^{-1}$. The time step should be sufficiently small so that the integration of the particle equations of motion is stable and accurate and also the particle oscillations can be faithfully reproduced.

7.2.3 Noise

The simulation particles moving across the cell boundaries cause fluctuations in the density which are then passed on to the potentials and the electric fields. These fluctuations can be ignored if they are smaller than the amplitude of the applied potentials and do not result in unstable behavior. Electrons are very sensitive to fluctuations in the field and can result in an unphysical increase in the electron energy. Ions are slower to respond to the fields so they are not affected by transient fluctuations. If this artificial increase in the electron energy becomes large enough it can start to cause excess ionization, which increases the plasma density, which magnifies the heating, resulting in an exponential increase in the plasma density and finally the simulation breaks down. Another problem is the loss of resolution in regions of lower density, i.e. sheaths. So one has to reduce the number of particles in a super-particle, i.e. use smaller super-particles.

7.3 The modified XPDP1 code

For our simulation studies on soliton evolution in the target chamber of a DP device we make use of the **XPDP1** (X-Windows Plasma Device Planar 1 Dimensional) code [66, 67]. This code is made available by the Plasma Theory and Simulation Group, University of California, Berkeley, US. It is a bounded electrostatic code for simulating one-dimensional bounded plasma plus an external electric circuit system whose characteristics can be specified by an input file.

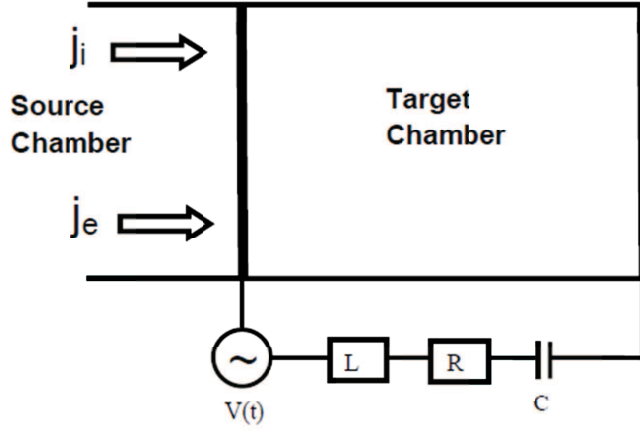


FIGURE 7.2: A simple schematic diagram of the DP setup as used in the simulation.

With respect to our PIC simulation investigations of soliton excitation in FLIPS, we need to simulate a source chamber and a target chamber. As the evolution of solitons takes place in the target chamber, the target chamber is of primary importance in our simulation. Simulating the source chamber needs extra computational space and time, thus the source chamber as a whole is not simulated, rather the current densities of the electrons and ions, being injected from the source chamber of the device, are evaluated. Keeping this in mind, the code has been modified in order to incorporate the distributions of the particles coming from the source chamber and entering the target chamber. The current density for the injected electrons is given as:

$$J_e = -en\sqrt{\frac{T_e}{2\pi m_e}} \exp[-e(\varphi_{src} - \varphi_{grid})/T_e] \quad \varphi_{grid} \leq \varphi_{src} \quad (7.1)$$

$$J_e = -en\sqrt{\frac{T_e}{2\pi m_e}} \quad \varphi_{grid} > \varphi_{src} \quad (7.2)$$

Similarly, the current density for the ions entering the target chamber is written as:

$$J_i = 0.61en\sqrt{\frac{T_e}{m_i}} \quad \varphi_{grid} \leq \varphi_{src} \quad (7.3)$$

$$J_i = 0.61en\sqrt{\frac{T_e}{m_i}} \exp[-e(\varphi_{src} - \varphi_{grid})/T_i] \quad \varphi_{grid} > \varphi_{src} \quad (7.4)$$

The ions enter with a velocity v_{0i} , which is given as:

$$v_{0i} = \sqrt{\frac{2e|\varphi_{src} - \varphi_{grid}|}{m_i}}$$

In the above equations, m_e , m_i and e are the electron mass, ion mass and electronic charge, respectively. Also, T_e , T_i and n are the electron temperature, ion temperature and the background number density in the source chamber, respectively. φ_{src} is the plasma potential of the source chamber and φ_{grid} is the potential on the separation grid.

In Fig. 7.2, the simulation box is specified. The left boundary of the simulation box is the modulated grid attached to an external circuit. The simulation box itself represents the target chamber of our experimental device FLIPS (as shown in Fig. 6.1a). The left hand side of the grid is the source chamber, from where the particles enter the target chamber through the separation grid G .

7.4 Simulation parameters

The simulation parameters are carefully chosen, keeping in view the conditions required for the PIC simulations. In our simulation studies the length of the simulation box is $l = 0.4$ m. This length is not exactly equal to that of the target chamber of the experimental device, but is enough to observe the excitation and propagation of solitons. We take the number of grid cells $n_g = 24000$. This makes the size of one simulation grid cell $\Delta x = l/n_g = 1.67 \times 10^{-5}$ m, which is a few times smaller than the Debye length, i.e. $\Delta x = \lambda_D/7$. This is in accordance with the condition given in section 7.2.2 that the size of the simulation grid cell should be smaller than the Debye length. The time step Δt is supposed to be very small as compared to the period of the electron plasma frequency, but long enough to make the simulations as fast as possible. Keeping this into consideration we took the time step $\Delta t = f_{pe}^{-1}/215 = 1 \times 10^{-10}$ s. The size of the super-particle is also an important parameter, and in our case one super-particle consists of 2×10^5 real particles. The gas used is Argon, as in the experiment.

7.5 Creating a steady-state plasma

The particles are lost at walls and this causes a continuous loss in the plasma density. So the first step is to create a steady-state plasma. We run the simulation until it reaches an equilibrium state, where the rate of loss of particles is equal to the rate of incoming particles. Apart from the particles coming from the source chamber, we also have introduced a volume source which replaces every lost ion with an ion-electron pair. At the steady state, the phase-space of electrons is shown in Fig. 7.3a. The electron velocity distribution is shown in Fig. 7.3b. We can clearly see that the electron velocity distribution is Gaussian. In case of ions the phase-space is slightly different (Fig. 7.4a) and the velocity distribution which is shown in the Fig. 7.4b slightly deviates from the Gaussian shape due to incoming ions from the source chamber.

At the steady-state, the number densities of the electrons and ions are obtained as $n_e = 2.42 \times 10^{13} \text{ m}^{-3}$ and $n_i = 2.3 \times 10^{13} \text{ m}^{-3}$, respectively. The

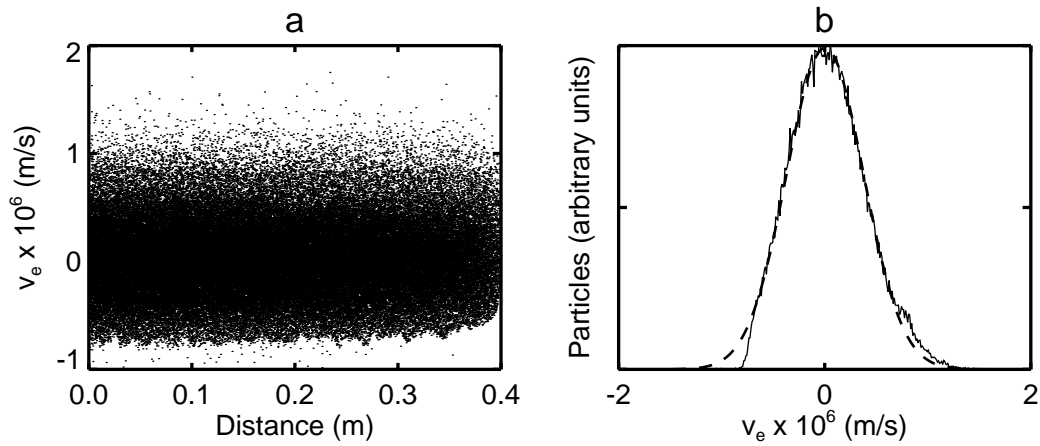


FIGURE 7.3: a) Electron velocity phase-space at the steady-state in the target chamber. b) Particle distribution for electrons (solid line) and fitted Gaussian distribution (dashed line) at the steady-state.

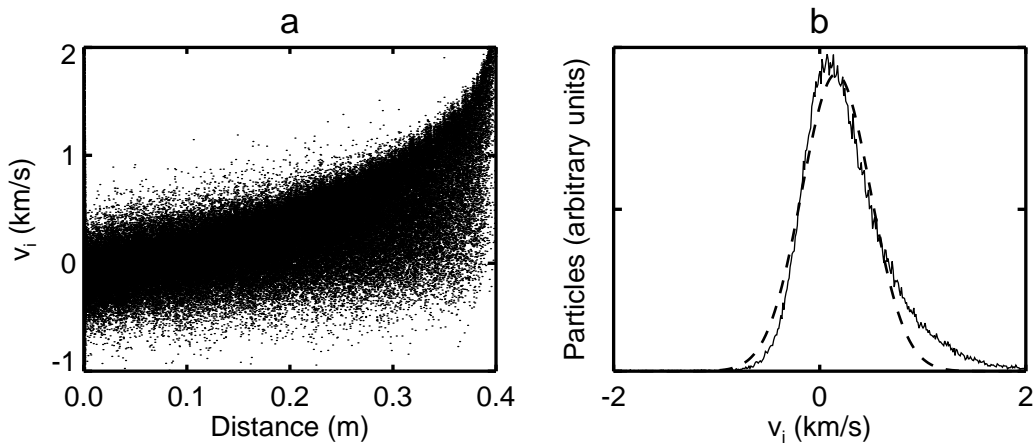


FIGURE 7.4: a) Ion velocity phase-space at the steady-state in the target chamber. b) Particle distribution for electrons (solid line) and fitted Gaussian distribution (dashed line) at the steady-state.

electron density and the averaged potential of the target chamber are plotted in Fig. 7.5a and 7.5b. The temperature of the electrons comes out to be $T_{ex} = 0.79$ eV and that of ions is $T_{ix} = 0.046$ eV, so that the ratio $T_e/T_i \approx 17$. The temperature of the electrons and ions in the target chamber is plotted in Fig. 7.6a. The kinetic energy carried by the electrons and ions is plotted in Fig. 7.6b.

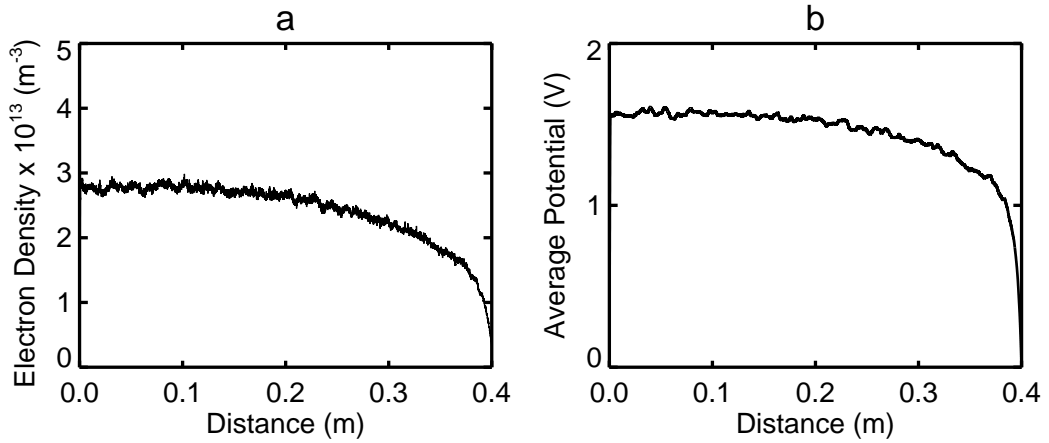


FIGURE 7.5: a) Electron density and b) averaged potential of the target chamber at the steady-state.

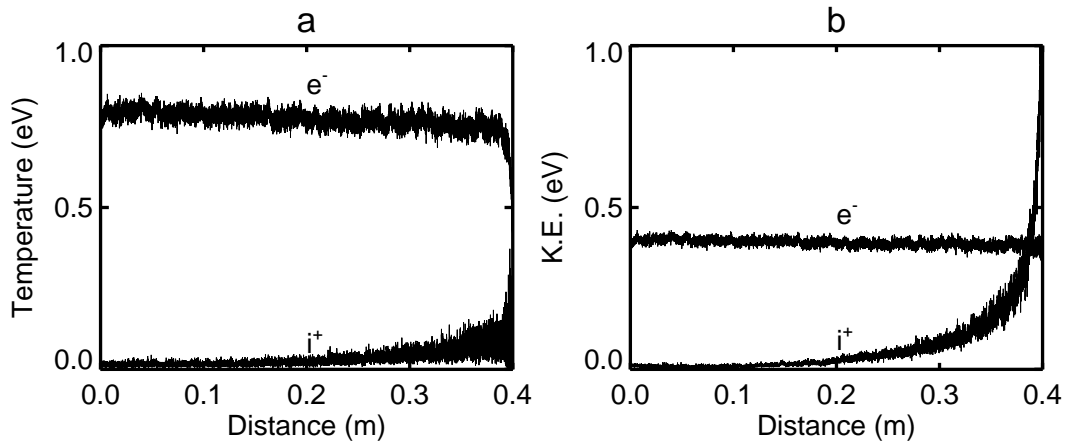


FIGURE 7.6: a) Temperatures and b) kinetic energies of the ions and electrons at the steady state in the target chamber.

7.6 Excitation of solitons

Now that the steady state plasma is achieved in the target chamber, i.e. the simulation box, we will excite the ion-acoustic solitons. For this reason, we apply a modulated signal on the left electrode which serves as the separation grid G in our simulation. The applied signal is shown in Fig. 7.7a. The frequency is 0.2 MHz and the peak-to-peak amplitude is 6 V. The signal was applied for a duration of 25 μs . As seen from Fig. 7.6a, the electron temperature is quite large as compared to the ion temperature, i.e. $T_e \gg T_i$. This is done in order to make the physical conditions comparable to that of the DP device and to reduce the effects of Landau damping.

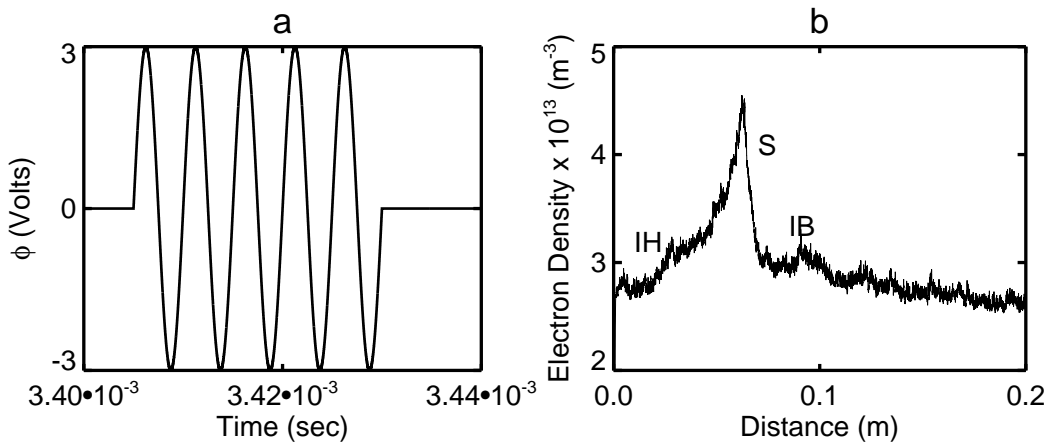


FIGURE 7.7: PIC simulation of the soliton showing a) the signal applied to the separation grid and b) electron density profile plotted against the distance from the grid in meters.

Figure 7.7b shows the electron density plotted against the distance in meters, showing the soliton profile along with the ion burst and the ion hole at $t = 40 \mu\text{s}$. This figure shows similar features as in Fig. 6.4.

Figure 7.8 shows the propagation of solitons in space towards the right. The speed of the soliton was calculated by following the trajectory of the soliton and the resulting distance-time graph, as shown in Fig. 7.9. The Mach number comes out to be about 1.2. This is the same as the value predicted by the KdV theory, showing that the soliton under consideration is a KdV soliton.

When the modulation is started, it is observed that ions are pulled into the simulation box during the negative cycle of the applied signal. Some of the incoming ions are too fast to contribute to the wave formation and simply move away to the other end of the simulation box. A lot of ions do contribute to the formation of the ion bursts, which finally leads to the evolution of linear and nonlinear waves. One thing has to be kept in mind that in the simulations the ratio T_e/T_i is slightly lower as compared to that in the experiment. This means that the ion temperature is slightly higher in the simulations as compared to

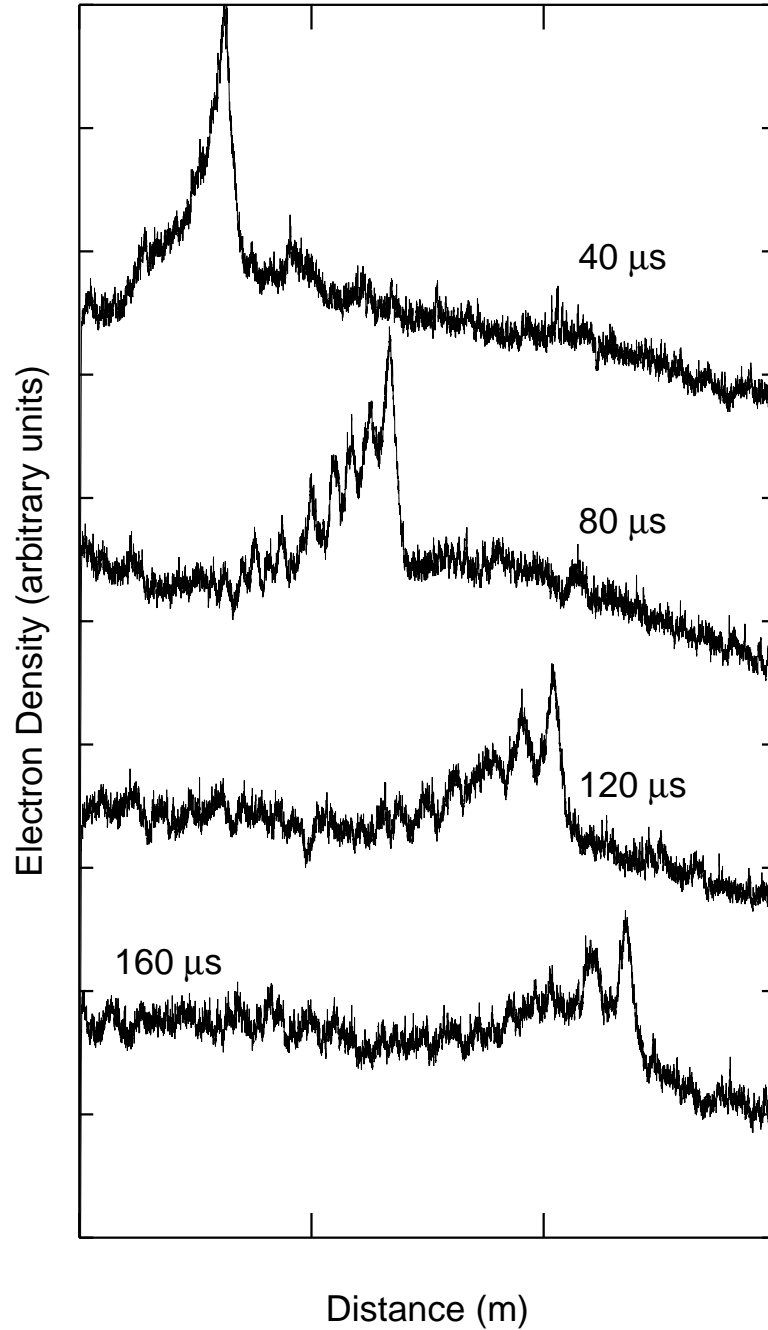


FIGURE 7.8: PIC simulation of the soliton propagating towards the right at $t = 40$, 80, 120 and 160 μs .

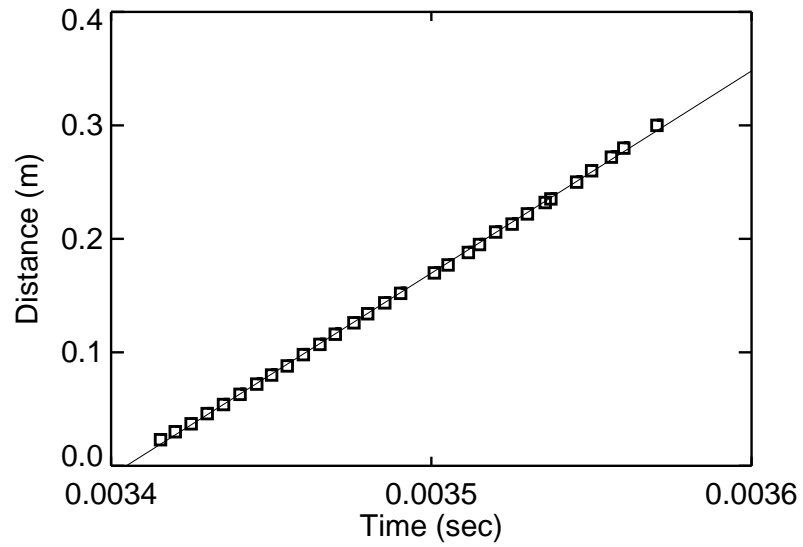


FIGURE 7.9: Time-distance graph of the soliton corresponding to Fig. 7.8. The velocity of the soliton is calculated to be around 1.2.

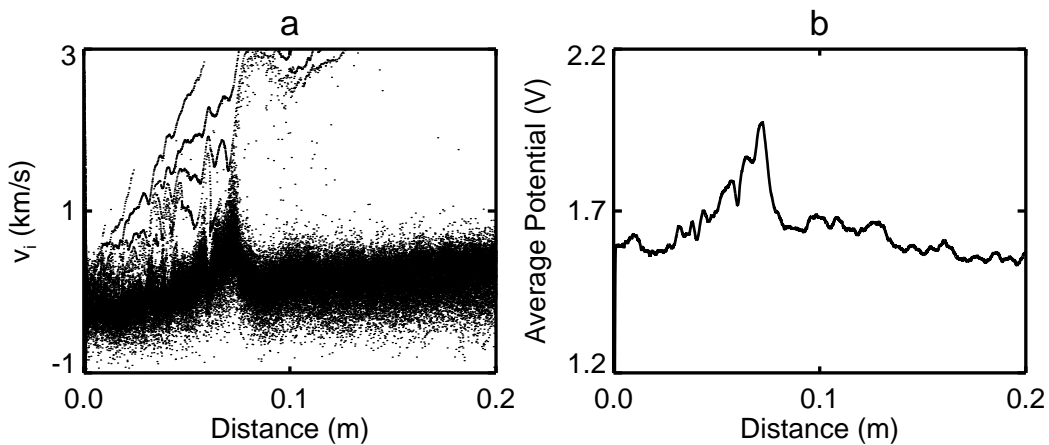


FIGURE 7.10: a) Ion phase-space and b) averaged potential of the soliton at $t = 45 \mu\text{s}$.

the experiment. The reason is the particle heating in the simulation which becomes significant during the application of the signal. This results in a slightly higher concentration of resonant ions, which get their energy from the grid G . These resonant ions are then responsible for the damping of the soliton and the evolution of other structures along with the ion hole from the trailing edge of the signal [68]. This is in complete agreement with the earlier observations where solitons are modified by resonant ions [69]. The ion phase-space in the vicinity of the soliton at $t = 45 \mu\text{s}$ is plotted in Fig. 7.10a, where the resonant ions ahead of the soliton can be clearly seen. Behind the soliton, we can also see some ion bursts which could have been reflected from the soliton potential. The potential of the soliton is plotted in Fig. 7.10b.

Figure 7.11 shows the soliton and other plasma features around the soliton vicinity at $t = 45 \mu\text{s}$. In Fig. 7.11a, a contour plot is prepared that shows the ion phase-space distribution. The electron density is portrayed in Fig. 7.11b which shows the soliton profile. Figure 7.11c is the ion temperature around the soliton. The higher temperature of the resonant ions around the soliton is depicted quite clearly in this plot. The last plot (Fig. 7.11d) shows the kinetic energy of the ions. The results shown in this figure completely agree with the experimental results obtained by the Laser Induced Fluorescence diagnostics on the target chamber of the FLIPS [70, 71], shown in Figure 7.12. It has to be kept in mind that the sudden dip in the velocity of the ions in Fig. 7.12 corresponds to the jump in Fig. 7.11 due to opposite direction of propagation of the ions in both the cases.

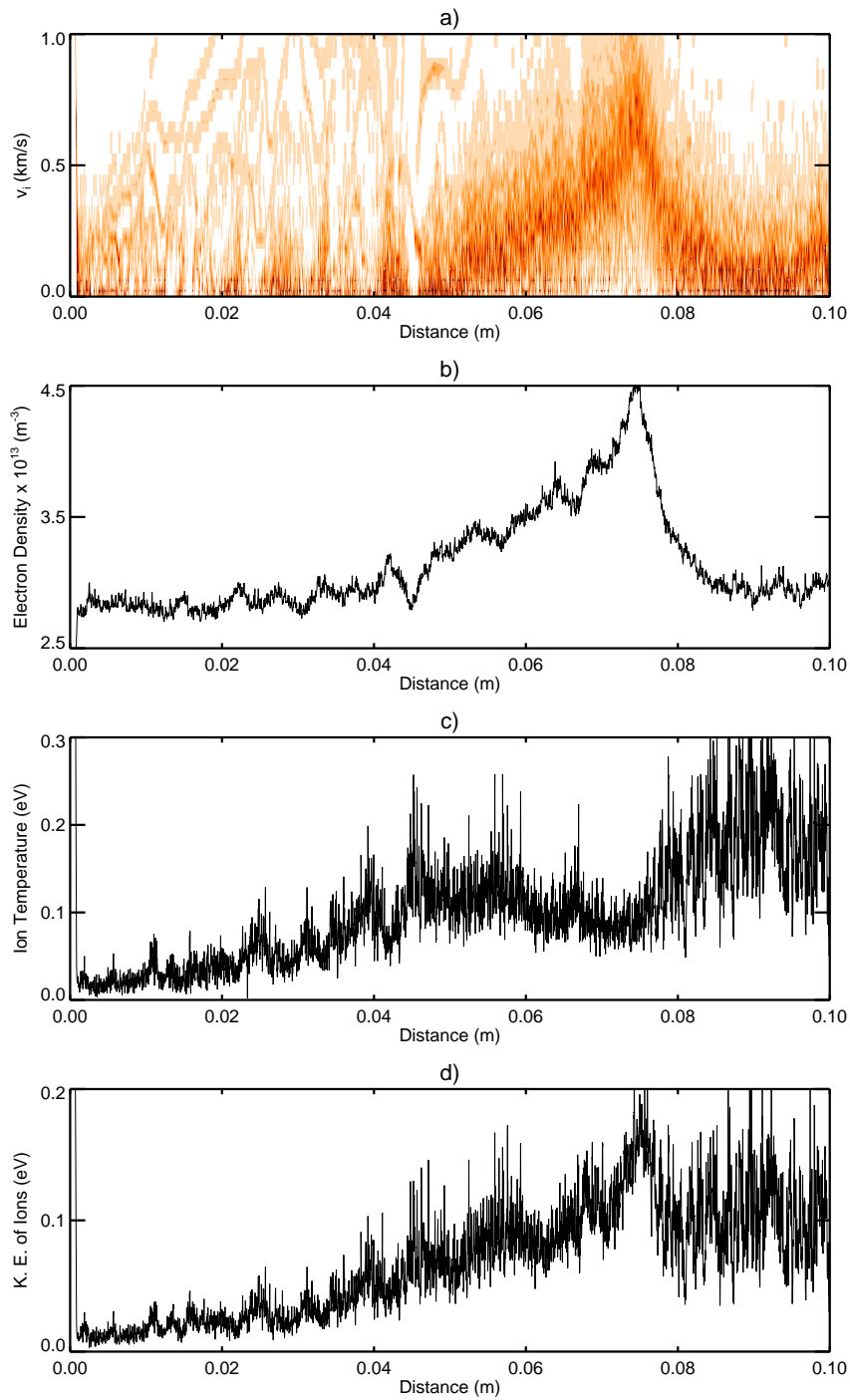


FIGURE 7.11: PIC simulations of the soliton and other plasma characteristics at $t = 45 \mu\text{s}$ plotted against the distance from the grid in meters. a) Ion phase-space distribution, b) electron density, c) ion temperature and d) kinetic energy of ions.

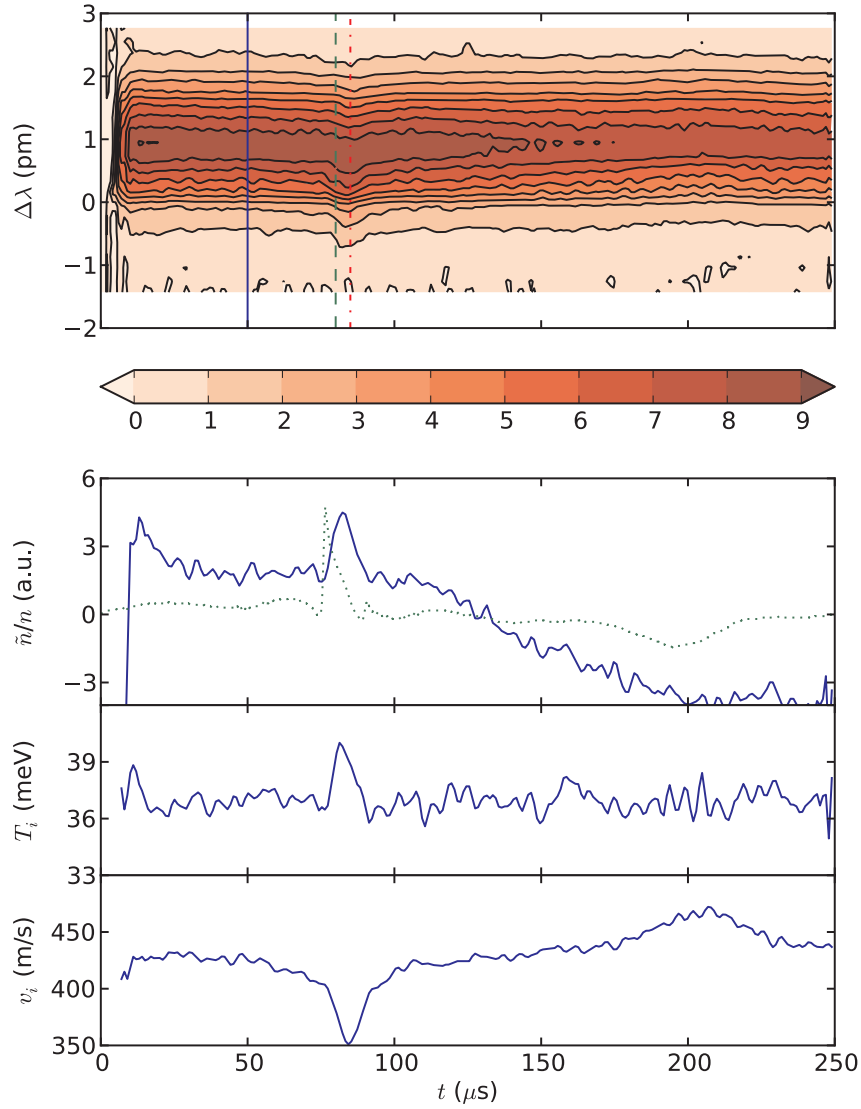


FIGURE 7.12: Soliton diagnostics by Laser Induced Fluorescence. The top graph shows the time dependence of LIF intensity (shading) and wavelength (y-axis). The second plot shows the density perturbation, whereas the dotted plot represents the electron density perturbation by the Langmuir probe. The third and fourth diagrams show the ion temperature and velocity distribution, respectively. Image courtesy: Sebastian Enge [71]

7.7 Effect of excitation signal parameters on soliton properties: Simulation results

For a comparison with experimental results, in this section we carry out PIC simulations of the effects of varying the amplitude, frequency and duration of the applied signal.

7.7.1 Effect of signal amplitude

In order to see the effect of excitation potential on the soliton generation, we carried out PIC simulations of soliton excitation at different applied potentials. Figure 7.13 shows the soliton profiles at different peak-to-peak voltages of the applied signal. The relative density amplitude $\delta n/n$ of the solitons is calculated and plotted against the applied voltage. The resulting graph is then shown in Fig. 7.14. It is seen that for low applied voltages the soliton amplitude is quite small which is then enhanced with the increase in the signal amplitude. This result is in agreement with the experimental observations (Fig. 6.8) presented in section 6.5.1. Just like in the experimental measurements we observe a saturation after an initial increase and the soliton amplitude becomes rather constant for higher applied voltages. The small amplitude of the soliton at low voltages can be explained by the fact that the mechanism of soliton excitation strongly depends on the speed of the ions coming from the source chamber. At low applied voltages the incoming ions are not fast enough to resonate with the initial perturbation, so a small or no soliton structure is observed. However, at high applied voltages the incoming ions are too fast to contribute to the soliton formation and hence we see no further increase in the soliton amplitude.

7.7.2 Effect of signal duration

The effect of the duration of the applied signal on the formation of solitons is shown in Figs. 7.15 and 7.16. The soliton profiles are plotted for different signal durations in Fig. 7.15. It has been mentioned earlier that the soliton and the ion burst are evolved from the initial part of the applied signal and the ion hole is generated from the trailing edge of the signal. For shorter signal durations we see small amplitude solitons due to the fact that the ion hole overlaps the soliton and affects its properties. For longer signal durations, we can see that solitons are evolved with higher amplitudes. Apart from that, other structures are also seen to emerge behind the soliton, when we increase the number of sinusoidal cycles in the applied signal. These structures are mainly bursts of resonant ions coming from the source chamber during the application of the long signal. These ions, being too energetic to resonate with the soliton, reflect from the soliton potential and lose some of their energy. This process then causes the generation of more solitons, albeit smaller and wider. This phenomenon becomes more clear in section 7.8. The ion hole is not distinctly visible due to the presence of these ion bursts and newly formed

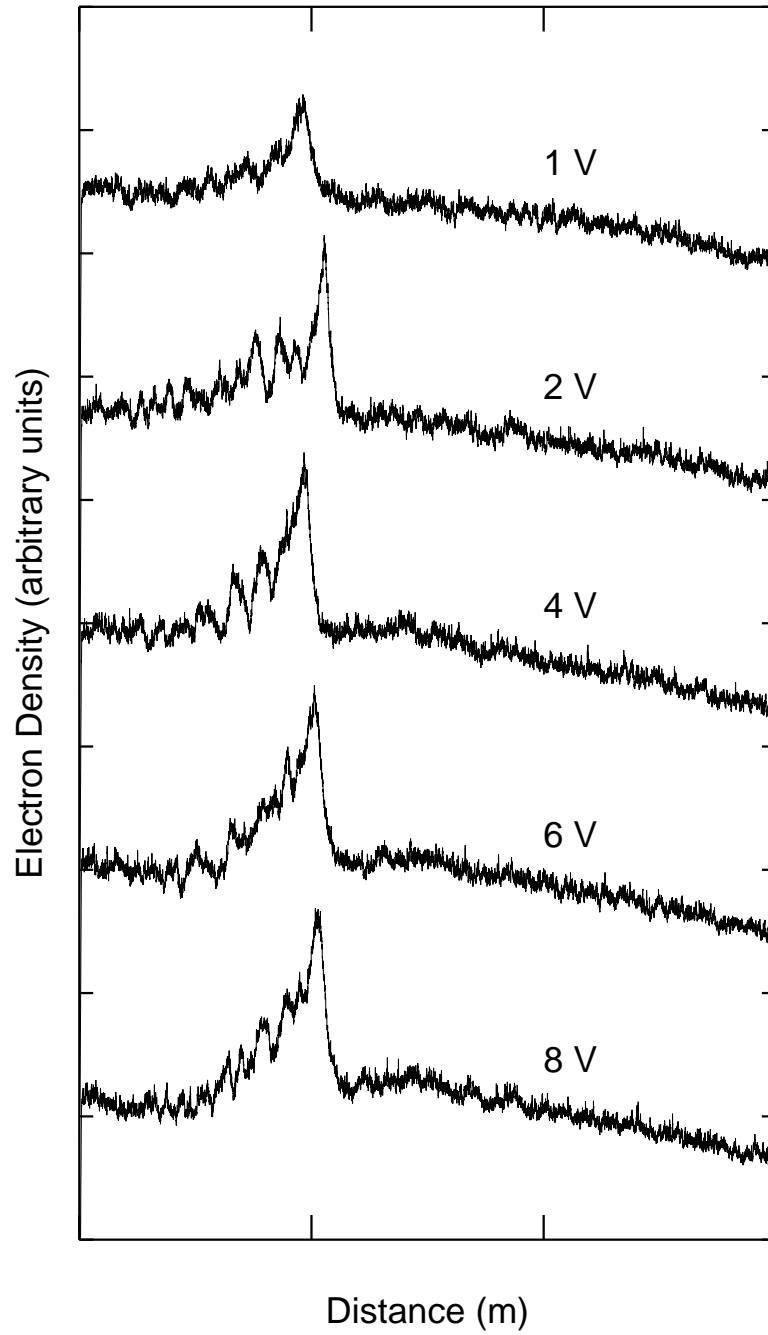


FIGURE 7.13: Soliton profiles at different peak-to-peak amplitudes of the applied signal.

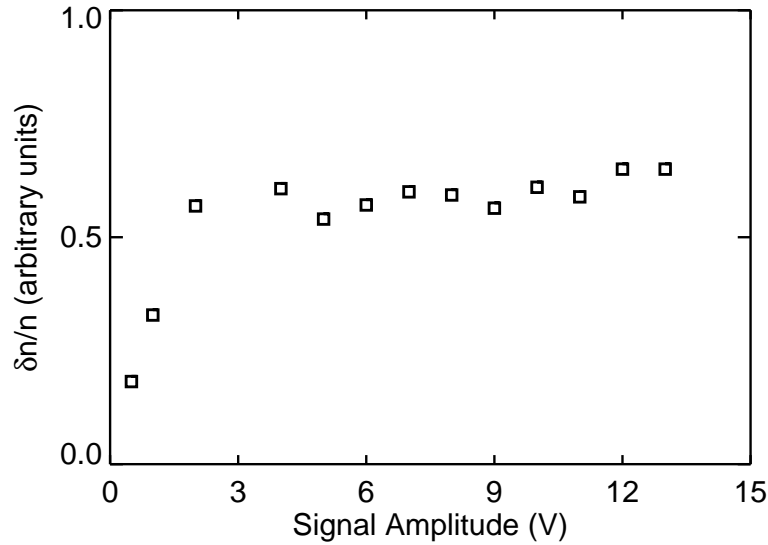


FIGURE 7.14: Dependence of soliton amplitude on peak-to-peak amplitude of the signal applied to the separation grid.

solitons. Figure 7.16 quite clearly depicts the fact that the soliton amplitude first increases and then becomes independent of the signal duration. This is in complete agreement with the observations in section 6.5.2.

7.7.3 Effect of signal frequency

The effect of changing the frequency of the applied signal is also simulated. Figure 7.17 shows the soliton profiles at different applied signal frequencies. In this figure, we observe more than one soliton at lower frequencies. This might be due to the longer rise time of the signal that leads to the formation of more than one soliton. Similar behavior has been observed in the experimental results presented in section 6.5.3. The amplitudes of the soliton are obtained at different values of applied frequencies and plotted in Fig. 7.18. It is observed that the amplitude increases and then attains saturation.

7.8 Role of fast ions

We extend our simulations further in order to investigate in detail the role played by fast ions on the propagation of solitons and ion hole as well as other structures that could be seen excited from the trailing edge of the signal, as in Fig. 7.17. Up till now we have simulated the solitons for $T_e/T_i > 10$. In order to see the effects of fast ions, we take $T_e/T_i < 10$ so that we can observe interaction between the energetic ions and the solitons. In this case the solitons are not excited from the beginning edge of the applied signal due to the fact

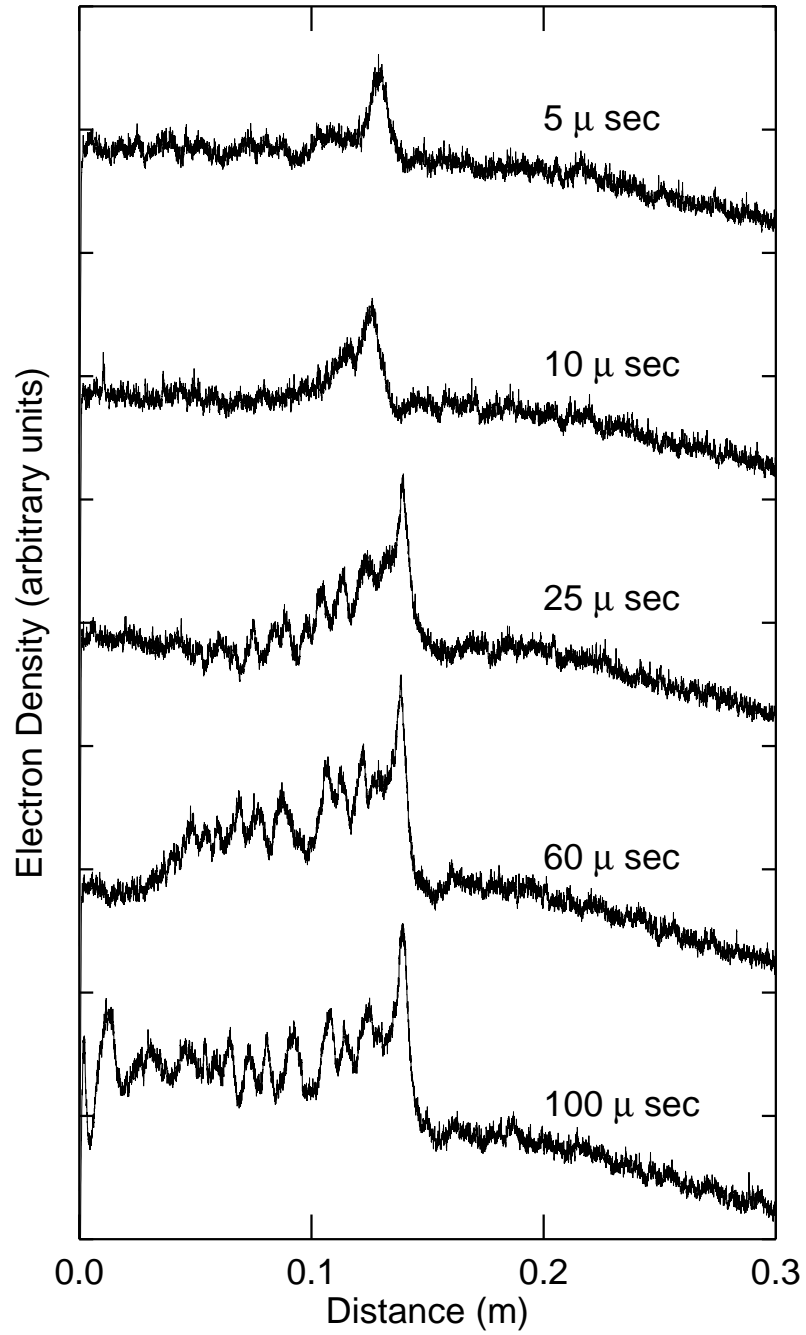


FIGURE 7.15: Soliton profiles at different applied signal durations.

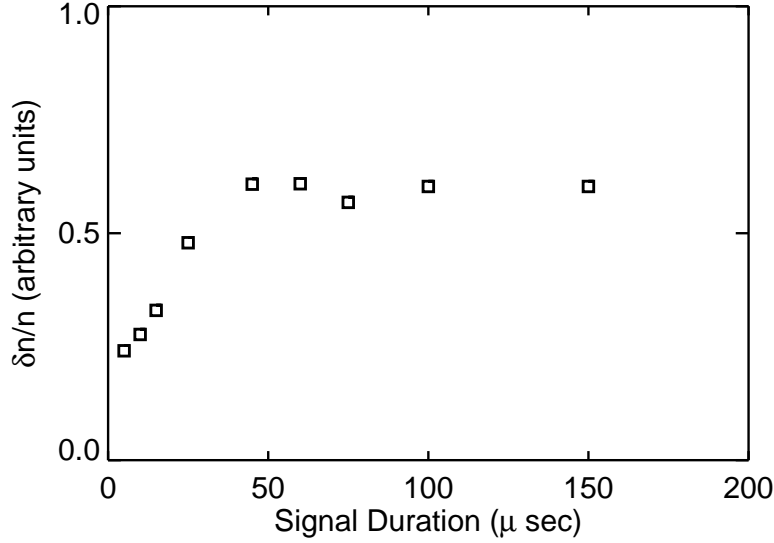


FIGURE 7.16: Dependence of soliton amplitude on peak-to-peak amplitude of the signal applied to the separation grid.

that the fast ions emitted were too energetic to resonate with the wave. This results in the excitation of only an ion burst and no solitons from the leading edge of the signal. Another factor responsible for the absence of the solitons is the Landau damping that causes the wave to dissipate [68, 69].

However, at the trailing edge of the signal, there is a completely different scenario. We have seen previously that for low ion temperatures the soliton is followed by an ion hole and other structures like pseudo-waves [72]. It is commonly observed that in grid excitation techniques used for soliton excitation in DP or multidipole devices, free streaming burst ions are also detected along with the solitons. The properties of these ion bursts depend on the excitation signal [24, 59, 60, 61]. Researchers have also investigated strong interaction of these fast ions with the solitons [73, 74].

When the separation grid is not modulated and the grid is at negative potential, then the ions from the source chamber are injected into the target chamber along with the current density given by Eq. 7.4. However, when the modulation signal is applied to the grid and the grid potential rises and attains a value equal to the plasma potential of the target chamber, then the ions that are in phase with the signal gain a large amount of energy. In this situation, a burst of fast ions is generated along with the usual thermal ions. The velocity of these free streaming fast ions is greater than the ion-acoustic velocity. So it is evident that these supersonic ions gain energy from the sudden rise in the grid potential when the modulation signal starts. Some of these fast ions generated in this process are non-interacting and are observed to have no effect on the soliton formation. However, we will focus on the supersonic ions which

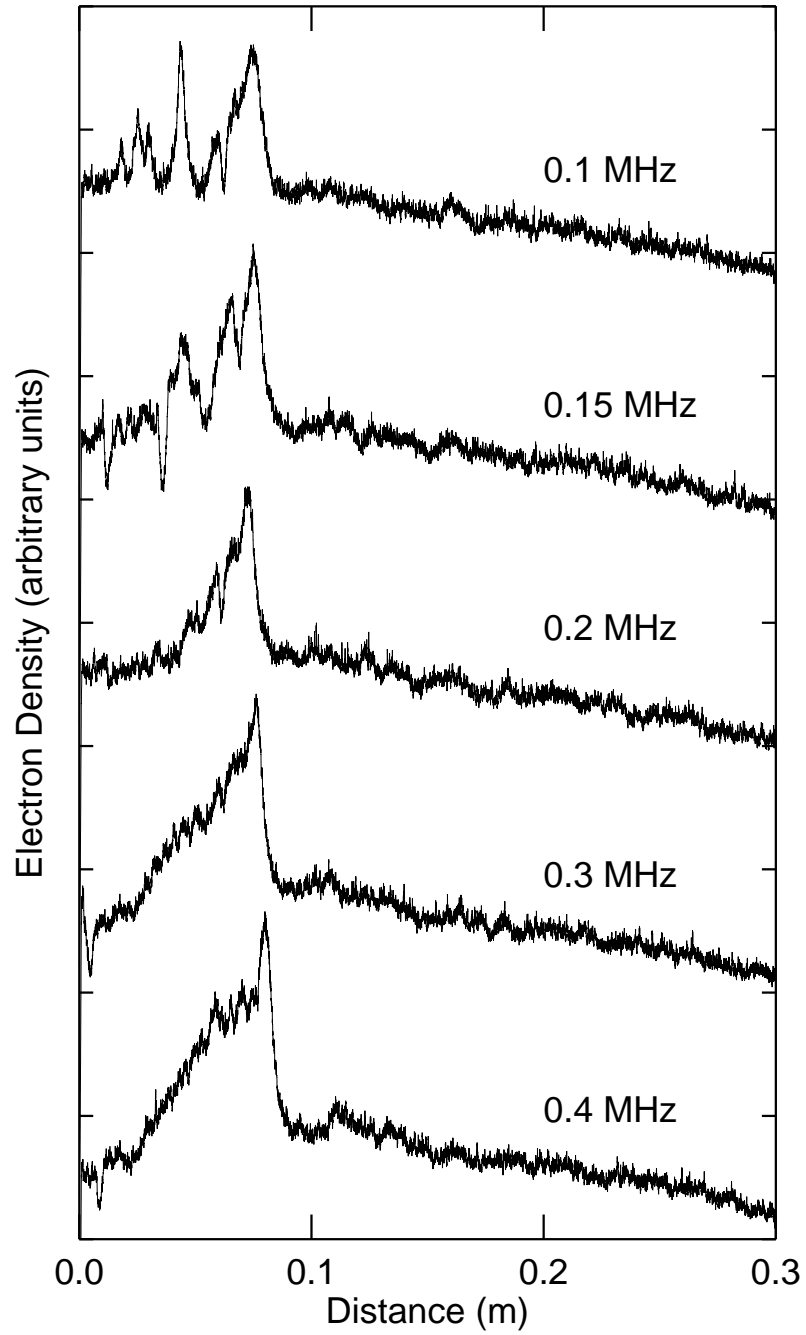


FIGURE 7.17: Soliton profiles at different applied signal frequencies.

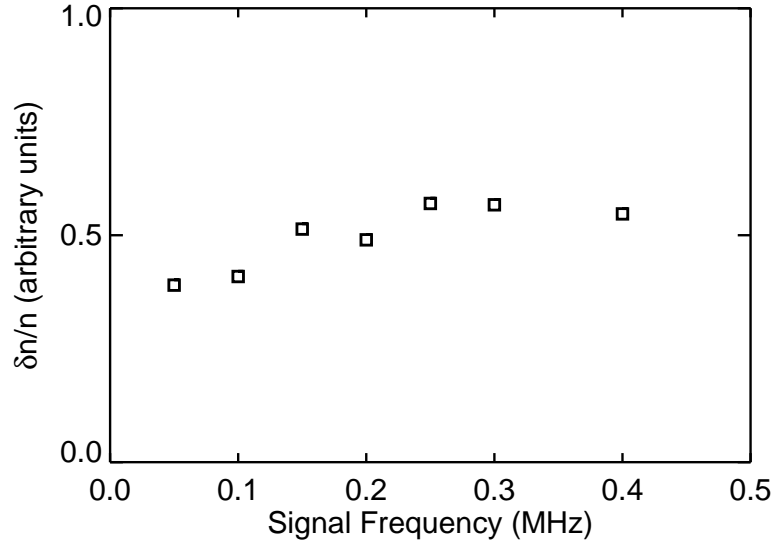


FIGURE 7.18: Dependence of soliton amplitude on applied signal frequencies.

interact with the waves and thus exchange energy with them.

Figure 7.19 shows the evolution and propagation of nonlinear waves in the presence of slightly higher temperature ions. The electron density and ion phase space at $t = 54 \mu\text{s}$ is plotted separately in Fig. 7.20. We observe an ion burst around $x = 11 \text{ cm}$ (marked as (1) in Fig. 7.19). This density bump consists of the faster ions, which gain their energy from the grid excitation. These faster ions are emitted from the beginning of the signal but are unable to contribute to the formation of soliton due to their non-resonant nature. Hence, we do not see a soliton evolving at (1), rather just a density compression that dissipates quickly. The density depression, also referred to as ion hole (IH) in this thesis, is created at the trailing edge of the applied grid signal.

In Fig. 7.19, at $t = 64 \mu\text{s}$, we see a spike arising between the ion hole (IH) and ion burst at (1). This structure grows and develops into a full fledged soliton S1 later. At $t = 74 \mu\text{s}$, we see an increase in the amplitude of this soliton. This increase in the amplitude is attributed to the presence of fast ions which transfer energy to the soliton. This increase in the amplitude of the soliton is short-lived, however, and we see that the soliton after some time returns to its normal amplitude at $t = 94 \mu\text{s}$. On close inspection, we also observe some other structures developing ahead of the main soliton, despite the noise. These structures grow with the passage of time and are clearly visible at $t = 114 \mu\text{s}$. As the time passes, a new soliton is seen to emerge after gaining its energy from the fast ions. The energy exchange at this point is clearly seen in the phase-space, plotted in Fig. 7.21. This figure shows the velocity phase-space of the ions, where the supersonic bursts are shown to be losing some of their energy. A careful look at these ions reveals that they are slowed down

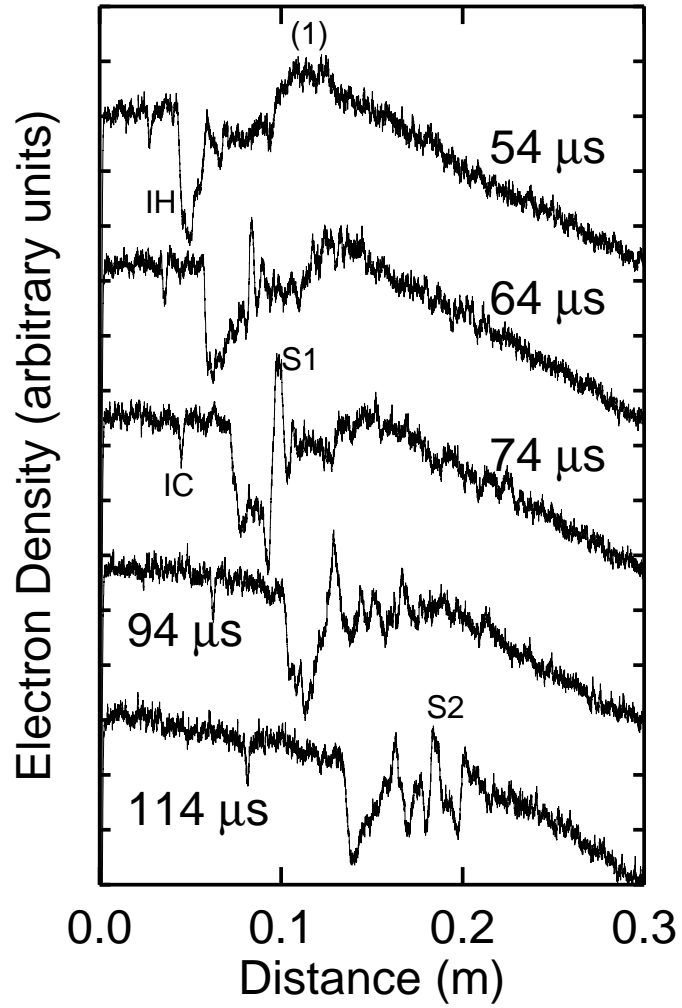
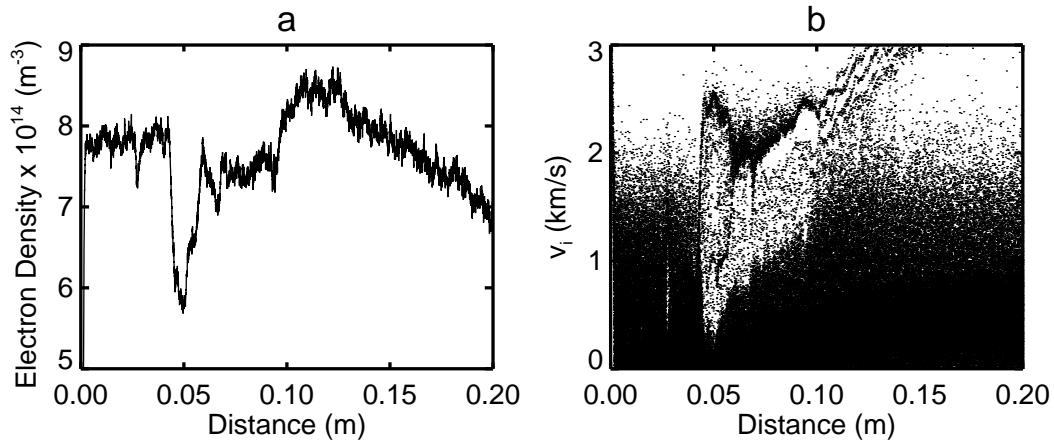
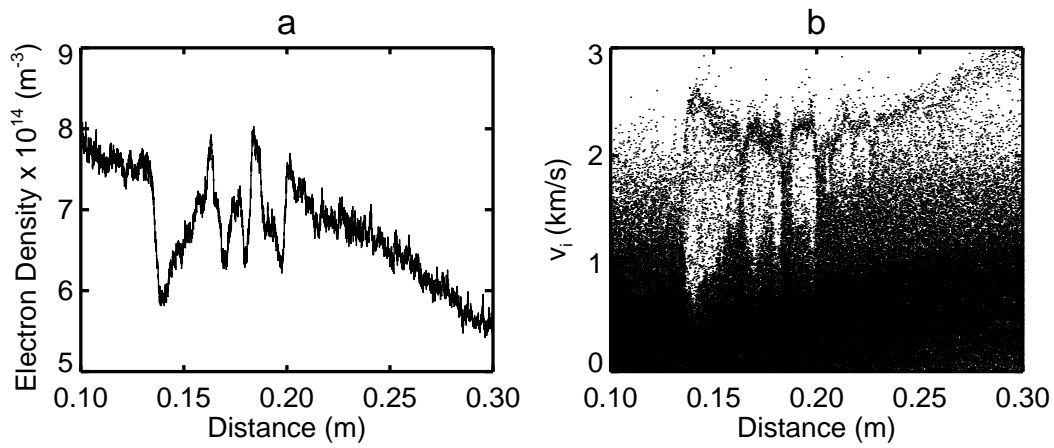


FIGURE 7.19: Evolution and propagation of solitons and other structures observed in the simulation for $T_e/T_i < 10$.

FIGURE 7.20: a) Electron density and b) phase-space at $t = 54 \mu\text{s}$.FIGURE 7.21: a) Electron density and b) phase-space at $t = 114 \mu\text{s}$.

exactly at the position of the soliton and hence, they exchange energy with the soliton. Since at this stage the amplitude of the soliton is enhanced, it is obvious that the soliton has gained the energy from these ions via an inverse Landau damping mechanism. In addition to this, it can also be seen from the ion temperature plots that the faster ions after interacting with the solitons become thermalized. The distance-time graphs that enable us to calculate the velocities of original soliton (S1), second soliton (S2), ion hole (IH) and ion cavity (IC) are shown in Fig. 7.22. Clearly both the solitons propagate nearly at the same velocity. Moreover, another rarefactive structure, referred to as ion cavity (IC) here, is seen to be propagating at a smaller velocity. This structure and the second soliton were not observed in earlier experiments and simulations.

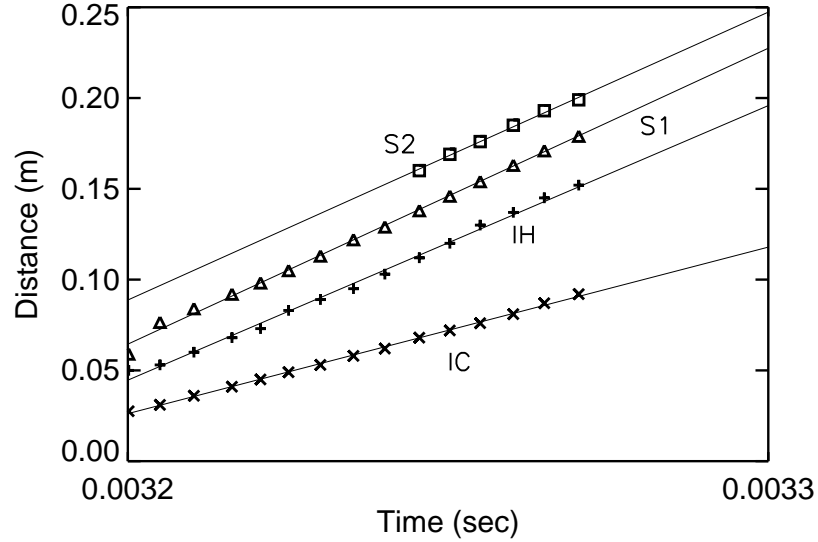


FIGURE 7.22: Trajectories of the various signals observed in the simulation. Here, S1 refers to the original soliton, S2 refers to the soliton developed at a later stage, IH refers to the ion hole and IC to the ion cavity. The velocities are found out to be $V_{S1} = 1.08$, $V_{S2} = 1.05$, $V_{IH} = 1.004$ and $V_{IC} = 0.61$.

In the present observations, the formation of soliton is directly affected by the presence of fast ion bursts, which is similar to the observations made by other researchers in the past [21, 25, 63, 68]. However, the new observation made in the present simulation is the formation of a second soliton. The reduction in the initial soliton structure is attributed to a decrease in the plasma density away from the grid. With respect to the evolution of the second soliton, we understand that it is due to the interaction of the ion burst with its neighboring structures. Owing to a decrease in the plasma density there sets up a pressure gradient force, which along with the fast ions succeeds in demolishing the moving ion bursts. Afterwards these ions strongly interact with the

structure ahead of the ion burst and cause this structure to evolve as a second soliton. In this process, it is quite plausible that the initial soliton loses some particles and hence, attains a smaller structure. In addition to these interesting results, we have also seen a localized structure (IC) in Fig. 7.19 around 3, 4, 5, 6.5 and 9 cm at $t = 54, 64, 74, 94$ and $114 \mu\text{s}$, respectively. This structure follows the soliton and obviously it propagates at a lower velocity than the soliton (Fig. 7.22). Figure 7.19 and the ion velocity space (Fig. 7.20) also confirm this situation as a complete depression in the ion concentration. It can be said that this structure corresponds to the rarefactive soliton, or this is a post-soliton as very recently has been observed in a laser plasma interaction experiment [75]. However, rarefactive solitons have largely been found in negative ion containing plasmas [26, 27]. On the other hand, the recent theories made in negative ion containing plasmas with two temperature electrons [50, 76] have shown that the rarefactive solitons do not occur in these plasmas as a consequence of low-temperature or trapped electrons. Since in the present simulations, two temperature ions are observed and high temperature/fast ions are observed to interact strongly with the waves and the soliton, it is quite possible that a rarefactive soliton evolves in such non-negative ion containing moving plasmas. Although, some experimental confirmation lacks in this case.

Chapter 8

Conclusions

In this thesis, the evolution of solitons and their propagation has been studied in plasmas. In addition to analytical investigations on soliton propagation, its reflection and transmission in inhomogeneous plasmas having trapped electrons, we have conducted experiments and also carried out simulations for studying solitons in a Double-Plasma device. Towards analytical investigations, we have developed theoretical models that enable us to examine the soliton reflection and transmission under the effect of two-temperature electrons (including trapped electrons), density inhomogeneity, drift of ions, obliqueness of wave propagation, etc. However, the experiment and simulations were performed with a focus on exploring the soliton evolution mechanism under the effect of excitation signal's duration, frequency and amplitude. Particularly in simulation studies, the role of fast ions in the generation of a secondary soliton was investigated in greater detail.

One-dimensional propagation of the solitons was analyzed under the effect of ion temperature, density and temperature of the trapped electrons. We observed that the usual KdV equation is modified by variable coefficients and an additional term appearing due to the density gradient present in the plasma. In particular it is found that:

- The solitons evolved are compressive solitons and also fulfill the criterion of a modified KdV equation.
- It was found that even a small fraction of the population of trapped electrons affects considerably the properties of the solitons; prominent modification in the soliton characteristics comes from the contribution of their thermal motion.
- The solitons propagate with larger amplitudes in the presence of trapped electrons. Similar effects of ion and electron temperatures on the phase velocity, soliton amplitude and width were observed in the plasma. This effect was more pronounced in the presence of more trapped electrons.

A two-dimensional analysis of the oblique reflection of solitons from a density inhomogeneity in the presence of trapped electrons was carried out keeping

in view the effect of obliqueness.

- In addition to the sech^2 term in the soliton solution of coupled equation, an extra term was also found to appear, which led to the down-shift of the incident soliton after its reflection. This down-shift increased with higher concentration of trapped electrons and higher temperatures of ions and trapped electrons. In case of smaller angles of reflection, this down-shift has a lower value.
- Solitons in an inhomogeneous plasma with trapped electrons emerge with a lower peak amplitude after the reflection. The strongest reflection of the soliton is possible only in the case of normal reflection. The reflection coefficient decreases with the increase in the temperature of ions and trapped electrons as well as for the concentration of trapped electrons.

In the last part of analytical investigations, for the first time we developed a theory for investigating the complete problem of soliton propagation, its reflection and transmission from a semi-transparent grid in an inhomogeneous plasma.

- A soliton reflection-transmission conservation law was derived, based on which the behavior of the solitons could be explored in greater detail, and the shifts in velocities of the reflected and transmitted solitons were obtained in terms of plasma parameters and the soliton solutions.
- It was observed that the angle of transmission depends on the angle of incidence of the solitons and it gets larger in the presence of trapped electrons and high temperature ions. The maximum possible ion drift velocity for the soliton transmission showed a significant dependence on the trapped electrons.
- A higher fraction of the energy of the incident soliton is utilized in the transmission in comparison with the reflection. In the presence of high temperature of ions and trapped electrons and their concentrations, solitons evolve with higher energies.

Linear and nonlinear ion-acoustic waves were excited in the target chamber of the DP device with $T_e/T_i > 10$, by applying the excitation signal on the grid separating the target and the source chambers.

- The linear dispersion relation of the ion-acoustic waves showed that for low frequencies the experimental result had complete agreement with the linear theory. At higher frequencies, the experimental results deviated from the linearity, pointing to the fact that the speed of ion-acoustic waves is no longer constant at higher frequencies.
- The soliton was found to be accompanied by an ion burst ahead of it, and was followed by an ion hole. Distance-time graphs showed that the

soliton velocity was quite close to the theoretically predicted velocity of the KdV soliton. It was seen that the ion hole was actually evolved from the trailing edge of the applied signal.

- The amplitude of the soliton increases with an increase in the peak-to-peak amplitude of the applied signal up to a certain maximum voltage, and then it becomes constant. Apart from that, it was seen that the ion burst preceding the soliton becomes bigger, as the peak-to-peak amplitude is increased.
- The soliton amplitude is independent of the applied signal duration, however, due to the formation of the ion hole very close to the soliton for small applied signal duration, we see smaller solitons for shorter applied signals.
- For low applied frequencies, more than one soliton structure was seen to appear. At slightly higher frequencies, we saw only one prominent soliton. The amplitude first increased and then became constant with the increase in the applied signal frequency.

PIC simulations not only reproduced the above experimental results for $T_e/T_i > 10$, but gave a detailed insight into the phase-space distributions of the resonant and non-resonant ions. The target chamber of the DP device was simulated, whereas the current densities of the particles coming from the source chamber were also included in the form of distributions.

- For $T_e/T_i > 10$, the PIC simulations of the soliton evolution showed similar features as in the experiment. Ion phase-space distributions were obtained those explained the importance of the role played by the resonant ions during the formation of a soliton.
- PIC simulations of the effect of excitation signal for $T_e/T_i > 10$ showed that the soliton amplitude behaves in a consistent manner with the experimental observations under the effect of the amplitude, duration and frequency of the applied signal, and it attained a saturation in its amplitude after undergoing an enhancement.
- For $T_e/T_i < 10$, simulations showed that the usual soliton was not evolved from the beginning of the signal due to non-resonant behavior of the fast ions. However, a strong interaction of fast ions and the ion hole generated at the trailing edge of the signal gave rise to another soliton.

Bibliography

- [1] N. J. Zabusky and M. D. Kruskal, Phys. Rev. Letters **15**, 240 (1965).
- [2] G. T. Delory *et al.*, Geophys. Res. Lett **25**, 2069 (1998).
- [3] S. K. El-Labany, M. Shalaby, E. F. El-Shamy, and L. S. El-Sherif, Planet. Space Sci. **57**, 1246 (2009).
- [4] C. M. Roach, J. W. Connor, and S. Janjua, Plasma Phys. Control. Fusion **37**, 679 (1995).
- [5] R. F. Hubbard *et al.*, IEEE Trans. Plasma Sci. **33**, 712 (2005).
- [6] J. S. Russell, *Report on waves* (Fourteenth meeting of the British Association for the Advancement of Science, York, 1844).
- [7] D. J. Korteweg and G. deVries, Phil. Mag. **39**, 422 (1895).
- [8] H. Washimi and T. Taniuti, Phys. Rev. Lett. **17**, 996 (1966).
- [9] S. Leibovich and A. R. Seebass, *Nonlinear waves* (Cornell University Press, New York, 1974).
- [10] N. Asano and T. Taniuti, J. Phys. Soc. Jpn. **27**, 1059 (1969).
- [11] N. Asano and T. Taniuti, J. Phys. Soc. Jpn. **29**, 209 (1970).
- [12] J. L. Cooney *et al.*, Phys. Fluids B **3**, 3277 (1991).
- [13] H. Schamel, Plasma Phys. **14**, 905 (1972).
- [14] H. Schamel, J. Plasma Phys. **9**, 377 (1973).
- [15] Y. Nishida and T. Nagasawa, Phys. Fluids **29**, 345 (1986).
- [16] W. D. Jones, A. Lee, S. M. Gleman, and H. J. Doucet, Phys. Rev. Lett. **35**, 1349 (1975).
- [17] B. N. Goswami and B. Buti, Phys. Lett. **57 A**, 149 (1976).
- [18] H. Alinejad, S. Sobhanian, and J. Mahmoodi, Phys. Plasmas **13**, 012304 (2006).

- [19] D. K. Singh and H. K. Malik, *IEEE Trans. Plasma Sci.* **36**, 462 (2008).
- [20] H. Ikezi, R. J. Taylor, and D. R. Baker, *Phys. Rev. Lett.* **25**, 11 (1970).
- [21] K. E. Lonngren, *Opt. Quant. Electronics* **30**, 615 (1998).
- [22] J. L. Cooney, M. T. Gavin, and K. E. Lonngren, *Phys. Fluids B* **3**, 2758 (1991).
- [23] J. L. Cooney, D. W. Aosse, J. E. Williams, and K. E. Lonngren, *Phys. Rev. E Stat. Phys. Plasmas Fluids Relat. Interdiscip. Top.* **47**, 564 (1993).
- [24] E. F. Gabl and K. E. Lonngren, *Plasma Phys. Control. Fusion* **26**, 799 (1984).
- [25] S. Yi, E.-W. Bai, and K. E. Lonngren, *Phys. Plasmas* **4**, 2436 (1997).
- [26] G. O. Ludwig, J. L. Ferreira, and Y. Nakamura, *Phys. Rev. Lett.* **52**, 275 (1984).
- [27] Y. Nakamura and I. Tsukabayashi, *Phys. Rev. Lett.* **52**, 2356 (1984).
- [28] H. H. Kuehl, *Phys. Fluids* **26**, 1577 (1983).
- [29] S. Singh and R. P. Dahiya, *Phys. Fluids B* **3**, 255 (1991).
- [30] H. K. Malik, *IEEE Trans. Plasma Sci.* **23**, 813 (1995).
- [31] H. K. Malik, *Phys. Lett. A* **365**, 224 (2007).
- [32] H. H. Kuehl, *IEEE Trans. Plasma Sci.* **PS-13**, 595 (1985).
- [33] R. P. Dahiya, P. I. John, and Y. C. Saxena, *Phys. Lett. A* **65**, 323 (1978).
- [34] Y. Nishida, *Phys. Fluids* **27**, 2176 (1984).
- [35] K. Imen and H. Kuehl, *Phys. Fluids* **30**, 73 (1987).
- [36] S. Raychaudhuri, R. Ichiki, and Y. Kawai, *Phys. Plasmas* **9**, 1125 (2002).
- [37] Y. Nishida, K. Yoshida, and T. Nagasawa, *Phys. Fluids B* **5**, 722 (1993).
- [38] T. Nagasawa and Y. Nishida, *Phys. Rev. Lett.* **56**, 2688 (1986).
- [39] O. Ishihara, I. Alexeff, H. G. Doucet, and W. D. Jones, *Phys. Fluids* **21**, 2211 (1978).
- [40] Y. Nakamura, T. Nomura, and T. Itoh, (*Proc. Int. Conf. Plasma Phys.*, Nagoya, Japan, 1980), Vol. 1.
- [41] G. Popa and M. Oertl, *Phys. Lett.* **98A**, 110 (1983).

- [42] A. Raychaudhuri, B. Trieu, E. K. Tsikis, and K. E. Lonngren, IEEE Trans. Plasma Sci. **PS-14**, 42 (1986).
- [43] Y. Nishida, K. Yoshida, and T. Nagasawa, Phys. Lett. A **131**, 437 (1988).
- [44] H. K. Malik, D. K. Singh, and Y. Nishida, Phys. Plasmas **16**, 072112 (2009).
- [45] G. C. Das and B. Karmakar, Aust. J. Phys. **43**, 65 (1990).
- [46] H. K. Malik, Phys. Plasmas **15**, 072105 (2008).
- [47] S. G. Tagare and R. V. Reddy, Plasma Phys. Control. Fusion **29**, 671 (1987).
- [48] C. Yan, Phys. Lett. A **224**, 77 (1996).
- [49] H. K. Malik and Y. Nishida, IEEE Trans. Plasma Sci. **35**, 1046 (2007).
- [50] T. S. Gill, H. Kaur, and N. S. Saini, Phys. Plasmas **10**, 3927 (2003).
- [51] H. K. Malik and K. Singh, IEEE Trans. Plasma Sci. **33**, 1995 (2005).
- [52] F. Aziz and U. Stroth, Phys. Plasmas **16**, 032108 (2009).
- [53] D. K. Singh and H. K. Malik, Plasma Phys. Control. Fusion **49**, 1551 (2007).
- [54] F. Aziz, H. K. Malik, and U. Stroth, IEEE Trans. Plasma Sci. **38**, 2802 (2010).
- [55] S. S. Chauhan and R. P. Dahiya, Phys. Lett. A **243**, 108 (1997).
- [56] S. Singh and R. P. Dahiya, J. Plasma Phys. **41**, 185 (1989).
- [57] K. N. Leung, T. K. Samec, and A. Lamm, Phys. Lett. A **51**, 490 (1975).
- [58] L. Schott, Phys. Fluids B **3**, 236 (1991).
- [59] K. E. Lonngren, M. Khazei, E. F. Gabl, and J. M. Bulson, Plasma Phys. **24**, 1483 (1982).
- [60] D. I. Xiao *et al.*, Phys. Plasmas **14**, 092104 (2007).
- [61] S. Raychaudhuri, E. F. Gabl, E. K. Tsikis, and K. E. Lonngren, Plasma Phys. Control. Fusion **26**, 1451 (1984).
- [62] S. I. Popel *et al.*, Phys. Rev. E, Stat. Phys. Plasmas Fluids Relat. Interdiscip. Top. **67**, 056402 (2003).
- [63] T. E. Sheridan, S. Yi, and K. E. Lonngren, Phys. Plasmas **5**, 3165 (1998).

- [64] T. E. Sheridan, IEEE Trans. Plasma Sci. **27**, 140 (1999).
- [65] C. K. Birdsall and A. B. Langdon, *Plasma Physics via Computer Simulation* (McGraw-Hill, New York, 1985).
- [66] J. Verboncoeur, V. Vahedi, M. V. Alves, and C. K. Birdsall, J. Comput. Phys. **104**, 321 (1993).
- [67] J. Verboncoeur, V. Vahedi, M. V. Alves, and C. K. Birdsall, *PDP1 Plasma Device Planar 1-Dimensional Bounded Electrostatic Code*, 1990.
- [68] Y. Saitou and Y. Nakamura, Phys. Lett. A **343**, 397 (2005).
- [69] V. I. Karpman *et al.*, Phys. Fluids **23**, 1782 (1980).
- [70] F. Aziz *et al.*, Plasma Phys. Controll. Fusion **53**, 065012 (2011).
- [71] S. Enge, Ph.D. thesis, Institut fur Plasmaforschung, 2010.
- [72] I. Alexeff, W. D. Jones, and K. E. Lonngren, Phys. Rev. Lett. **21**, 878 (1968).
- [73] T. Honzawa, M. Arakawa, and S. Singh, Phys. Fluids B **4**, 2807 (1992).
- [74] T. Honzawa and T. Nagasawa, Phys. Plasmas **4**, 3954 (1997).
- [75] G. Sarri, D. K. Singh, J. R. Davies, and F. Fiuza, Phys. Rev. Lett. **105**, 175007 (2010).
- [76] H. K. Malik and U. Stroth, Plasma Sources Sci. Technol. **17**, 035005 (2008).

Acknowledgments

I have made a sincere effort in removing the debt of obligation to those who have helped me throughout my doctoral research work.

First and foremost, I thank Allah Almighty who blessed me with the strength and capability to accomplish this task, Alhamdulillah.

I owe my deepest gratitude to my supervisor Prof. Dr. Ulrich Stroth for putting his trust in me and allowing me to join his group, and for his constant guidance throughout my Ph.D. I really appreciate his logical way of thinking and his polite manner in which he offered his valuable advice. I would also like to thank Dr. H. K. Malik for his time and interest particularly in the analytical part of the thesis. His optimistic approach during the research work is sincerely appreciated.

I consider it my pleasant duty to acknowledge my colleagues at the Institut für Plasmaforschung (IPF) for providing a pleasant environment in which to learn and grow. A special thanks goes out to Dr. Alf Köhn for being really kind and patient enough to bear with me, and answer my constant queries regarding almost everything, including IDL and Latex. I also offer my sincere gratitude to Dr. Sebastian Enge for the help he extended during the measurements at FLIPS. The experimental part of this thesis would not have been possible without his expertise. I would like to extend many thanks to Dr. Lars Stollenwerk for his valuable guidance and insightful discussions about the simulation code. I thank Dr. Eberhardt Holzhauser for always being so kind to me and my daughter. Many thanks to all my colleagues at IPF especially Bernhard Nold, Gregor Birkenmeier, Mirko Ramisch and Hendrik Höhnle. This friendly group of people has made my stay here at IPF Stuttgart very pleasant and memorable.

I wish to express my thanks to my family back home, for being a constant source of support and encouragement. Especially for looking after Maryam with such unselfish love and care, in my absence. However, no words can express the deepest gratitude that I owe to my parents for praying for me and always believing in me no matter what. I also wish to thank Ali, my loving husband, who was always there for me with his unfailing support. I really appreciate his emotional support in tough times during my Ph.D. pursuit. My heartfelt gratitude goes out to Maryam, to whom this thesis is dedicated, for being far more understanding than an ordinary six-year-old. I believe she has missed out on a lot due to my hectic schedule during the course of this work. I must say that I consider myself very lucky to have such a supportive family. I

would also like to acknowledge my parent institute, Department of Physics, GC University Lahore, Pakistan, for providing me with this opportunity to pursue my Ph.D. in Germany. Finally, the financial support of the Higher Education Commission (HEC) Pakistan and Deutscher Akademischer Austausch Dienst (DAAD) is gratefully acknowledged.

FARAH AZIZ

Eidesstattliche Erklärung

Hiermit erkläre ich an Eides Statt, dass ich diese Arbeit ausschließlich unter Anleitung meiner wissenschaftlichen Lehrer und unter Verwendung der angegebenen Hilfsmittel angefertigt habe.

Stuttgart, den 01.06.2011

Farah Aziz